UNIVERSITY OF SOUTHAMPTON

Faculty of Engineering and Physical Sciences
School of Engineering

Micromagnetic simulations of helimagnetic nanostructures

by

Martin Lang

ORCiD: 0000-0001-7104-7867

A thesis for the degree of
Doctor of Philosophy

December 2023

University of Southampton

Abstract

Faculty of Engineering and Physical Sciences
School of Engineering

Doctor of Philosophy

Micromagnetic simulations of helimagnetic nanostructures

by Martin Lang

Complex magnetic materials hosting topologically non-trivial, particle-like objects such as skyrmions or Bloch points are under intensive research and could fundamentally change the way we store and process data. One important class of materials in which such chiral magnetisation configurations can be found are helimagnetic materials with Dzyaloshinskii-Moriya interaction. Recently, it was demonstrated that nanodisks consisting of two layers with opposite material chirality can host a single stable Bloch point—a point singularity in the magnetisation configuration—of two different types at the layer interface.

In this work, we use finite-difference micromagnetic simulations to study static and dynamic properties of Bloch points in the two-layer system. To conduct the simulations, we use a Python package called Ubermag, which defines a domain-specific language to express micromagnetic problems and provides a high-level interface to existing micromagnetic calculation packages such as OOMMF. Its functionality and capabilities have been significantly enhanced and extended as part of this work.

In the first part of the work, we focus on the static properties of Bloch points in rectangular two-layer FeGe nanostrips. We find that multiple Bloch points in any possible combination of the two different types can coexist—a crucial prerequisite for potential applications. The number of Bloch points in stable configurations depends on the strip geometry. We can predict suitable geometries for a given Bloch-point number, which we demonstrate for an 80-Bloch-point configuration.

In the second part of the work, we study the dynamics of the stable Bloch points when an electric current is applied, which couples to the magnetisation via the spin-transfer torque. We demonstrate that the Bloch points move in the current direction without deflection. Constrictions in a nanostrip can be used to control the motion: at lower current densities, Bloch points are trapped at the constrictions; at higher current densities, they can move past them. This can be exploited to move arrays of Bloch points in a controlled manner. Finally, we demonstrate that Bloch points in more complex geometries with multiple possible paths, such as the T-shaped geometry studied in this work, can move along the different paths if current is applied in suitable directions.

Contents

List of Figures

Declaration of Authorship

I declare that this thesis and the work presented in it is my own and has been generated by me as the result of my own original research.

I confirm that:

1. This work was done wholly or mainly while in candidature for a research degree at this University;
2. Where any part of this thesis has previously been submitted for a degree or any other qualification at this University or any other institution, this has been clearly stated;
3. Where I have consulted the published work of others, this is always clearly attributed;
4. Where I have quoted from the work of others, the source is always given. With the exception of such quotations, this thesis is entirely my own work;
5. I have acknowledged all main sources of help;
6. Where the thesis is based on work done by myself jointly with others, I have made clear exactly what was done by others and what I have contributed myself;
7. Parts of this work have been published as:
    - Beg, M., Lang, M. & Fangohr, H. (2022). Ubermag: Toward More Effective Micromagnetic Workflows. *IEEE Transactions on Magnetics*, **58** (2), 1–5
    - Lang, M., Beg, M., Hovorka, O. & Fangohr, H. (2023a). Bloch points in nanostrips. *Scientific Reports*, **13** (1), 6910
    - Lang, M., Pathak, S. A., Holt, S. J. R., Beg, M. & Fangohr, H. (2023b). Controlling stable Bloch points with electric currents. *Scientific Reports*, **13** (1), 18934

Signed:..... Date: 20 December 2023

List of Publications

Published

- M. Beg, M. Lang and H. Fangohr. Ubermag: Toward More Effective Micromagnetic Workflows. *IEEE Transactions on Magnetics **58**, 2* (2022)
- M. Lang, M. Beg, O. Hovorka and H. Fangohr. Bloch points in nanostrips. *Scientific Reports **13**, 6910* (2023)
- M. Lang, S. A. Pathak, S. J. R. Holt, M. Beg and H. Fangohr. Controlling stable Bloch points with electric currents. *Scientific Reports **13**, 18934* (2023)

Under review

- M. Lonsky, M. Lang, S. J. R. Holt, S. A. Pathak, R. Klause, T. Lo, M. Beg, A. Hoffmann and H. Fangohr. Developing computational skills through simulation based problem-solving in science. arXiv:2303.01784 (2023)
- T. B. Winkler, M. Beg, M. Lang, M. Kläui and H. Fangohr. Energetics and Dynamics of a stable Bloch point. arXiv:2303.10091 (2023)
- S. J. R. Holt, M. Lang, J. C. Loudon, T. J. Hicken, D. Suess, D. Cortés-Ortuño, S. A. Pathak, M. Beg and H. Fangohr. Virtual experiments in computational magnetism: `mag2exp`. (2023)

Acknowledgements

First of all, I would like to thank Prof. Hans Fangohr for giving me the opportunity to carry out this work and for his excellent supervision. Without him, the present work would not have been possible. I would like to thank Dr. Marjian Beg for his patience, support, and guidance in the beginning of my candidature.

Thank you to Dr. Marijan Beg, Dr. Samuel Holt, Dr. Swapneel Amit Pathak, and Prof. Hans Fangohr for the constructive work and repeated discussions on the Ubermag software.

I would like to thank the Max Planck Institute for the Structure and Dynamics of Matter in Hamburg, Germany, for giving me the opportunity to carry out parts of the work at their institute. My thanks go to everyone at MPSD, in particular Kevin Yanes Garcia, Dr. Henning Glawe, Ashwin Kumar, and Kauser Zulfiqar, for the nice and friendly atmosphere.

Finally, I would like to thank Dr. Swapneel Amit Pathak and Kevin Yanes Garcia for their help in proofreading parts of this thesis.

Chapter 1

Introduction

Our society is highly dependent on modern technology, which plays a crucial role in all aspects of our lives. While our reliance on technology has increased significantly in recent decades, fundamental changes have always been linked to technological advances. Most of these advances are the result of extensive fundamental and applied research. The substantial recent changes are primarily related to digitisation due to the proliferation of computers and embedded devices connected via the Internet and the massive increase in computing power over the past decades. These changes have been made possible by significant advances in semiconductor technology and magnetism, among others.

Ongoing advances still make it possible to double memory capacity and computing power roughly every two years, as described by Moore's law (Moore, 1965, 1975). However, this trend is coming to an end. The miniaturisation of magnetic storage has nearly reached physical limits (Richter, 2009; Tannous & Comstock, 2017). Likewise, increases in computing power can now be achieved mostly through improved parallelisation, especially GPU computing (Baji, 2018), and improved device designs, while the miniaturisation and clock speeds of modern processors have also almost reached physical limits (Markov, 2014; Waldrop, 2016).

Furthermore, improving energy efficiency has become a key issue for a number of reasons. First, data centres and cloud services consume huge amounts of electricity, which is more and more evolving into an environmental problem. Second, low power consumption and hence long battery life are important for many mobile and IoT (Internet of Things) applications. Third, heat generation and the difficulty of cooling chips effectively is one of the fundamental issues for increasing computing power.

To address these issues and further advance digital technology, fundamentally new concepts for novel types of logic and storage devices are required, both in terms of how these devices operate and what computing paradigms they are based on. New types of magnetic materials show promising features and have the potential to play an important role in future devices. One possible new type of fast, non-volatile data storage is magnetic racetrack memory. This

new concept could allow for the realisation of truly three-dimensional magnetic storage devices and thus significantly increased storage capacities compared to current, effectively two-dimensional, hard disks. In racetrack memory, data is stored in nanowires and can be moved to fixed read and write elements. This design avoids mechanically moving read and write elements and could therefore substantially decrease access times. Furthermore, the absence of mechanically moving elements can help reduce energy consumption. In their initial proposal, Parkin et al. (2008) have suggested to use domain walls in nanostrips as information carriers. Based on the initial idea, other types of particle-like magnetisation configurations such as skyrmions have also been proposed (Fert et al., 2013). Actual realisation still faces many problems. One difficulty is that the aforementioned designs rely on the presence or absence of a single type of magnetic object, and the data is hence encoded in the distance of these objects that needs to be preserved to avoid data loss. Suggestions have been made to overcome this design limitation by using particles of different types (Zhu et al., 2020) or multiple lanes (Müller, 2017).

More generally, magnetic materials are complex systems with numerous physical properties, often exhibiting complex behaviour. As such, they form a vibrant field of fundamental research. A fundamental feature of magnetic materials is the competition between different interactions. Ferromagnetic materials are dominated by exchange interaction, which favours aligned magnetic moments. In addition, magnetocrystalline anisotropy, demagnetisation, and Zeeman interaction (with external magnetic fields) play an important role. In bulk systems, these interactions typically lead to the formation of large uniform domains separated by narrow regions of non-collinear magnetisation called domain walls.

1.1 Helimagnetic materials

In the late 1950s, a new type of interaction was predicted for low-symmetry materials, the so-called Dzyaloshinskii–Moriya interaction (DMI) (Dzyaloshinsky, 1958; Moriya, 1960). DMI favours perpendicular alignment of neighbouring magnetic moments. The competition between exchange interaction and DMI can lead to the formation of helical magnetic configurations (Fig. 1.1). Materials that feature DMI are referred to as helimagnetic materials. Under suitable

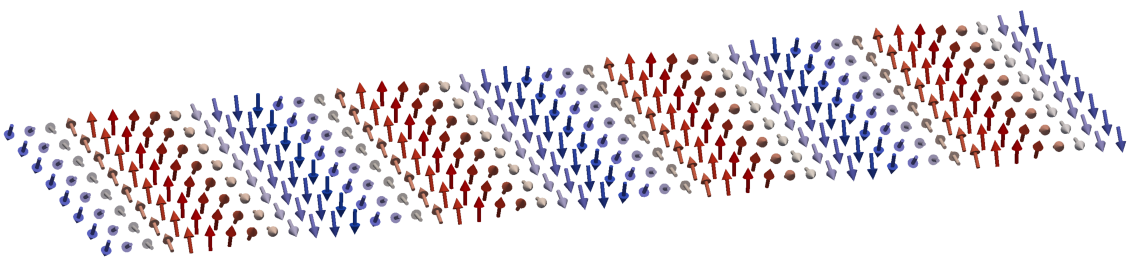

FIGURE 1.1: Magnetic helix.

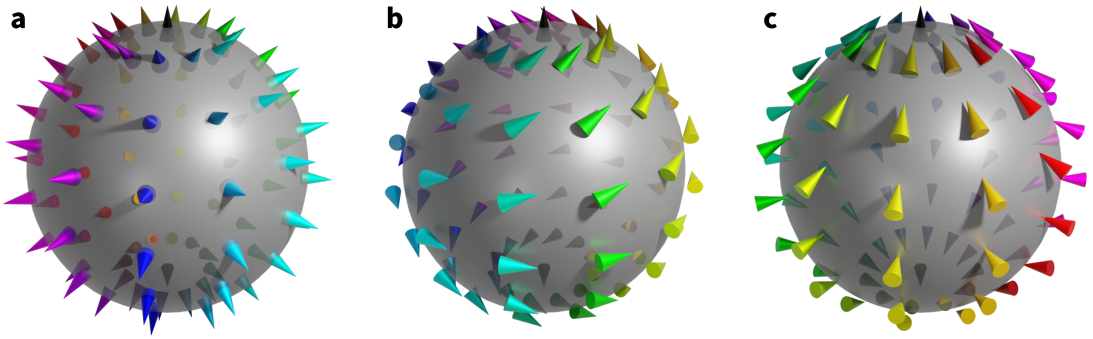

FIGURE 1.2: A Bloch point can occur in different configurations: (a) diverging configuration, (b) circulating configuration, and (c) spiralling configuration. Configurations (b) and (c) can be obtained from configuration (a) by rotating all magnetic moments by $\pi/2$ and π around the z axis, respectively. The spheres are semi-transparent to also show cones on the rear. Visualisation adapted from Im et al. (2019, Fig. 1).

conditions, e.g. with an applied magnetic field, the competition between DMI and exchange interaction can also lead to twisted, vortex-like magnetic configurations called skyrmions, which were first predicted in particle physics (Skyrme, 1962). Skyrmions show interesting features such as topological protection.

A different intriguing configuration is the so-called Bloch point, a point of vanishing magnetisation (Feldtkeller, 1965; Döring, 1968). A Bloch point is characterised by the fact that the magnetisation configuration on any closed surface surrounding the Bloch point spans the entire solid angle. Hence, Bloch points also have a non-trivial topology. Bloch points exist in different configurations. Figure 1.2 shows examples for a diverging, a circulating, and a spiralling Bloch point. The existence of Bloch points could be experimentally verified in several systems (Kabanov et al., 1989; Thiaville & Miltat, 1994; Da Col et al., 2014). Various theoretical works indicate the importance of Bloch points during dynamical processes of other magnetisation textures such as magnetisation reversal of domain walls (Hillebrands & Thiaville, 2006) and switching of vortices (Hertel et al., 2007) and skyrmions (Beg et al., 2015). Bloch points do not only emerge in dynamical processes, some systems can also host static Bloch points (Malozemoff & Slonczewski, 1979; Kanazawa et al., 2011; Rybakov et al., 2015).

A new system that can host a single stable Bloch point has recently been predicted by Beg et al. (2019). The authors have micromagnetically studied helimagnetic nanodisks consisting of two FeGe layers with opposite material chirality. They observe the formation of a stable Bloch point in two different realisations and demonstrate switching between the two types with an external magnetic field. The present thesis is based on this work and studies the two-layer system in more detail.

We use finite-difference micromagnetic simulations to study Bloch points in a two-layer FeGe system with layers of opposite material chirality. In the majority of the work, we focus on rectangular nanostrips. We show that such nanostrips can host multiple Bloch points and

that arbitrary combinations of the two different types can exist. Furthermore, we study the dynamics of Bloch points when applying a spin current and find collective motion of arrays of Bloch points. We show that geometrical variations can be used to control the movement. All simulations are performed using a Python package called Ubermag (Beg et al., 2022).

1.2 Thesis structure

In Chapter 2 we introduce the micromagnetic model and give an overview of different topological magnetisation configurations. We describe how static and dynamic systems are studied within the micromagnetic framework and explain the most relevant contributions to the energy and dynamics equation. We discuss the effects of spin currents on the magnetisation and the concept of emergent electrodynamics, an effective model for the description of an electron traversing a magnetisation structure. The latter is closely related to the concept of topological charge, which is also explained in this chapter. Lastly, we give an overview of existing literature on domain walls, vortices, skyrmion, and Bloch points.

In Chapter 3 we discuss Ubermag, the software used to perform all simulations in this work. Ubermag is an interface to existing micromagnetic calculators and defines a domain-specific language to formulate micromagnetic problems in a machine-readable format. Its aim is to simplify running micromagnetic simulations and analysing the resulting data. We first discuss a typical workflow in micromagnetics and the importance of reproducibility, which motivate the Ubermag Python software. To introduce Ubermag, we first explain its use in a simple example and then discuss the overall design. During the present work, I have significantly extended and modified Ubermag. The most important changes as well as some more general software engineering practices are discussed in the last part of this chapter.

In Chapter 4 we present the results for multiple stable Bloch points in nanostrips, published in Lang et al. (2023a). In this chapter, we show that multiple stable Bloch points can coexist in the two-layer nanostrips. We find that different combinations of the two different types can be stabilised and compare their properties and the effects of different strip sizes. We observe the formation of additional antivortices between Bloch points of the same type. Furthermore, we find simple rules to predict strip geometries (length and width) for arbitrary numbers of Bloch points and put these to a test for a larger system.

In Chapter 5 we focus on manipulating Bloch points using spin currents, published in Lang et al. (2023b, currently under review). First, we study the motion of a single Bloch point and a pair of Bloch points in rectangular nanostrips. Then, we study the effect of constrictions in the geometry. We find that Bloch points can get trapped at constrictions for lower current densities. This can be exploited to divide a long nanostrip into multiple storage areas and move arrays of Bloch points through this structure in a controlled manner. Short strong current pulses are used to push Bloch points from one storage area to the next. Finally, we study the

motion of a single Bloch point in a T-shaped geometry. Depending on the direction of the applied current, the Bloch point can move along different paths in the structure.

In Chapter 6 we summarise the new results obtained in this work. We discuss their implications and outline possible future work.

Chapter 2

Micromagnetism

Preface

Parts of the discussion of the Bloch point in the two-layer system in Sec. 2.8.4 have been published in Lang et al. (2023a).

In this chapter, we introduce the framework of micromagnetism, which provides a powerful description of microscopic magnetic systems. Section 2.1 introduces the prerequisites and basic assumptions of the micromagnetic model. In Section 2.2 we focus on static micromagnetism. Static configurations can be obtained solely based on the energy equation of the system. In Section 2.3 we discuss important energy contributions for ferromagnetic and helimagnetic materials. In Section 2.4 we focus on the description of the dynamics of magnetic systems based on the Landau-Lifshitz-Gilbert equation. In Section 2.5 the influence of spin currents on the magnetisation is discussed. In Section 2.6 we discuss the effects of non-collinear magnetisation on the conduction electrons and the connection to the topological charge of magnetic structures. In Sec. 2.7 we briefly discuss numerical methods used for micromagnetic simulations. In Section 2.8 we discuss several magnetisation configurations that can form in ferromagnetic and helimagnetic materials, namely domain walls in Sec. 2.8.1, vortices in Sec. 2.8.2, skyrmions in Sec. 2.8.3, and Bloch points in Sec. 2.8.4.

2.1 Introduction

Each electron carries a magnetic moment consisting of two parts, orbital magnetic moment and spin. The orbital magnetic moment depends on the atomic orbital of the electron. To some extent, this can be explained as the quantised microscopic movement of a charged particle, in analogy to the macroscopic picture (Krishnan, 2016). The spin is an intrinsic property of an electron. A macroscopic analogue would be a spinning charged particle, which however cannot quantitatively explain the spin. The electron's spin can only be fully explained within relativistic quantum mechanics.

Different approaches are available to model the physics of a solid magnetic structure. Important numerical methods are ab-initio methods, spin models, and the micromagnetic model. The different models can resolve the ferromagnet on different levels and come at different computational cost. The most detailed description is provided by ab-initio methods, which can resolve the electron wave functions. However, this method is also computationally most demanding and only applicable to small systems with a limited number of atoms. Spin-models provide the first level of approximation. Here, each magnetic atom is represented by a single magnetic dipole. This description is well suited to study e.g. finite-temperature effects, effects of rough interfaces, or anti-ferromagnets.

The micromagnetic model (Brown, 1963) provides a reliable description for magnetisation processes on larger length scales, typically in the range of tens of nanometres to micrometres, using an effectively classical framework. Effective energy terms are used to include relevant quantum effects into the classical model. The most important quantum effect is the exchange interaction, which is of fundamental importance for the formation of ferromagnetism. Micromagnetics can be used to resolve the internal structure of magnetic configurations such as domain walls or skyrmions. It does not treat all spins individually. Instead, it assumes that the individual spins are effectively parallel on a small length scale λ much larger than the lattice constant a (Abert, 2019). Hence, micromagnetics is only applicable to ordered systems with strong ordering forces, such as strong exchange interaction. In the micromagnetic model individual spins are approximated with a continuous vector field $\mathbf{M}(\mathbf{r})$, the magnetisation. The condition $\lambda \gg a$ is a prerequisite for this description as it justifies neglecting local variations of the spin density resulting from the crystal structure and effects from the crystal field in the averaged magnetisation. The model's assumption is then to have a homogeneous spin density in arbitrary volumes larger than λ^3. A consequence of the homogeneous spin density is that the norm of the magnetisation does not vary spatially. The magnetisation can therefore be divided into a unit vector field $\mathbf{m}(\mathbf{r})$ and the spontaneous magnetisation M_s:

$$\mathbf{M}(\mathbf{r}) = M_\mathrm{s}\mathbf{m}(\mathbf{r}), \tag{2.1}$$

$$|\mathbf{m}(\mathbf{r})| \equiv m(\mathbf{r}) = 1. \tag{2.2}$$

At zero temperature, the only case considered in this work, M_s is the saturation magnetisation of the magnetic material, a material constant. At non-zero temperature below the ordering temperature thermal fluctuations decrease the value compared to the saturation magnetisation. (Abert, 2019)

2.2 Static micromagnetism

Static magnetic structures can be studied using only the system's energy equation. Equilibrium configurations are characterised by local minima of the total free energy E of the system. Individual contributions to the total energy will be discussed in the next section. In the

continuum description, variational calculus can be used to obtain minima of the total free energy E with respect to the magnetisation $\mathbf{m}$. Here, the normalisation condition $|\mathbf{m}| = 1$ must be taken into account. It can be included in the variational formalism using a Lagrange multiplier technique.

A necessary condition for a local energy minimum is a vanishing functional differential of the energy (Abert, 2019):

$$\begin{aligned}\delta E(\mathbf{m}, \mathbf{v}) &= \frac{\mathrm{d}}{\mathrm{d}\epsilon} E(\mathbf{m} + \epsilon\mathbf{v}) = \lim_{\epsilon \to 0} \frac{E(\mathbf{m} + \epsilon\mathbf{v}) - E\mathbf{m}}{\epsilon} \\ &= 0 \quad \forall \quad \mathbf{v} \in V_m,\end{aligned} \tag{2.3}$$

where $\mathbf{v}$ is an arbitrary test function and V_m the function space of the magnetisation $\mathbf{m}$. The right-hand side of Eq. 2.3 can be expressed in terms of the functional derivative $\delta E/\delta\mathbf{m}$ and an additional boundary term $\mathbf{B}(\mathbf{m})$. Furthermore, the condition of constant magnetisation can be taken into account using Lagrange multipliers λ and μ that enforce constant magnetisation inside the magnetic volume V and on the surface ∂V (Abert, 2019):

$$\delta E(\{\mathbf{m}, \lambda, \mu\}, \mathbf{v}) = \int_V \mathrm{d}\mathbf{r}\, \frac{\delta E}{\delta \mathbf{m}} \cdot \mathbf{v} + \int_{\partial V} \mathrm{d}\mathbf{s}\, \mathbf{B} \cdot \mathbf{v} + 2 \int_V \mathrm{d}\mathbf{r}\, \lambda \mathbf{m} \cdot \mathbf{v} + 2 \int_{\partial V} \mathrm{d}\mathbf{s}\, \mu \mathbf{m} \cdot \mathbf{v}. \tag{2.4}$$

Analytic expressions for $\delta E/\delta\mathbf{m}$ and $\mathbf{B}(\mathbf{m})$ can be derived for individual terms of the energy equation as well as combinations of multiple energy terms, details can be found in Abert (2019). To find more complicated micromagnetic structures, which cannot easily be expressed with closed expressions, numerical treatment is required.

2.3 Energy equation

In the following, we discuss important contributions to the total free energy of a ferromagnet. In general, the total energy is given as (Liu et al., 2017):

$$E_{\mathrm{tot}} = E_{\mathrm{ex}} + E_{\mathrm{K}} + E_{\mathrm{d}} + E_{\mathrm{DMI}} + E_{\mathrm{Z}}, \tag{2.5}$$

where E_{ex} is exchange energy, E_{K} magnetocrystalline anisotropy energy, E_{d} demagnetisation energy, E_{DMI} Dzyaloshinskii-Moriya interaction energy, and E_{Z} Zeeman energy. For some systems additional energy contributions originating from other types of interactions, such as RKKY interaction (Ruderman & Kittel, 1954; Kasuya, 1956; Yosida, 1957), which describes long-range coupling of magnetic moments mediated by the conduction electrons, or magnetostriction (Ekreem et al., 2007), shape deformation in an applied magnetic field, can be observed.

Depending on the material in question, the contribution of the individual energy terms to the total energy varies. In many materials some contributions are completely absent. The different

contributions are discussed in the following subsections based on the book by Liu, Zhang, and Zhao (2017) and the review paper by Abert (2019).

2.3.1 Exchange energy

Exchange interaction is the most important energy contribution for ferromagnets. It is the cause for the non-zero net magnetisation in the absence of an external field. It originates from quantum mechanics and cannot be explained classically. Exchange interaction is a consequence of the Coulomb interaction. It can lead to both parallel (ferromagnetic) and antiparallel (antiferromagnetic) spin alignment. Exchange interaction can be very strong, resulting in Curie temperatures up to around 1000 K in some materials (Mohn & Wohlfarth, 1987).

The origin of exchange interaction can be intuitively understood by considering a two-electron system. As an example, we consider the ferromagnetic case. We assume that the two electrons are in orthogonal orbitals, and we neglect spin-orbit interaction. The total wave function for this system consists of an orbital and a spin part, which are decoupled. The total wave function has to be antisymmetric for the fermionic system. Hence, for the product of orbital and spin part to be antisymmetric, one of the two must be symmetric while the other is antisymmetric. For an antisymmetric orbital part of the wave function the probability density between the two sites is reduced compared to the symmetric orbital part. This in turn reduces the energy contribution of the Coulomb interaction, which depends on the overlap of the individual electron wave functions. Therefore, the spin part of the ground-state wave function is symmetric, hence parallel alignment (spin triplet) is preferred over antiparallel alignment (spin singlet). However, the two-electron model only provides a simplified picture indicating the type of mechanism behind exchange energy. The situation is much more complex in full many-body systems with more than two electrons.

In a semi-classical picture, the exchange energy between two localised electrons with spins $\mathbf{S}_1$ and $\mathbf{S}_2$ is expressed by the Heisenberg model:

$$E_{\mathrm{ex}} = -J_{ij}\,\mathbf{S}_1 \cdot \mathbf{S}_2, \tag{2.6}$$

where J is the exchange integral obtained from the full quantum-mechanical description. In a many-body system we obtain:

$$E_{\mathrm{ex}} = -\frac{1}{2}\sum_{i,j} J_{ij}\,\mathbf{S}_1 \cdot \mathbf{S}_2, \tag{2.7}$$

where the pre-factor compensates double counting in the sum. In most systems exchange interaction only has a short range. In an isotropic system with only nearest-neighbour exchange interaction and constant coupling between all neighbouring pairs, the energy can be written as:

$$E_{\mathrm{ex}} = -J\sum_{\langle ij\rangle} \mathbf{S}_i \cdot \mathbf{S}_j, \tag{2.8}$$

where $\langle ij \rangle$ denotes the sum over nearest neighbours. In ferromagnetic materials ($J > 0$) parallel alignment of neighbouring spins minimises the exchange energy. In antiferromagnetic materials ($J < 0$) the exchange energy causes neighbouring spins to align antiparallel.

In the continuum limit, for $J > 0$, exchange energy can be written as:

$$E_{\text{ex}} = A \int \mathrm{d}V \left[(\nabla m_x)^2 + \left(\nabla m_y\right)^2 + (\nabla m_z)^2 \right], \tag{2.9}$$

where $A = JS^2 z/a$ is the exchange stiffness, with z the number of sites per unit cell (e.g. $z = 1$ for simple cubic lattices), and a the nearest-neighbour distance. The continuum form can be derived from a Taylor expansion of Eq. 2.8. A full derivation is e.g. given by Abert (2019). The continuum description, derived for localised spins, can also be used to accurately describe band magnets and anisotropic materials (Abert, 2019).

2.3.2 Dzyaloshinskii-Moriya energy

In certain materials with broken inversion symmetry an additional antisymmetric exchange interaction is present. This so-called Dzyaloshinskii-Moriya interaction (Dzyaloshinsky, 1958; Moriya, 1960) causes neighbouring spins to align perpendicular. It arises from spin-orbit coupling, typically via a third non-magnetic atom.

The antisymmetric exchange energy between two spins $\mathbf{S}_i$ and $\mathbf{S}_j$ is given as (Moriya, 1960):

$$E_{\text{DMI}} = \mathbf{d}_{ij} \cdot (\mathbf{S}_i \times \mathbf{S}_j), \tag{2.10}$$

where $\mathbf{d}_{ij}$ is the DMI vector that depends on the crystal structure and symmetry. Moriya (1960) has derived a set of rules that determine the existence or absence as well as the direction of the vector $\mathbf{d}_{ij}$ depending on the crystal symmetry. DMI can exist both in bulk systems and at the interface between a ferromagnet and a heavy metal.

In bulk systems with broken inversion symmetry, crystal classes T and O, the vector $\mathbf{d}_{ij}$ takes the form (Abert, 2019):

$$\mathbf{d}_{ij} = -d\mathbf{e}_{ij}, \tag{2.11}$$

where $\mathbf{e}_{ij}$ is a unit vector pointing from spin $\mathbf{S}_i$ to spin $\mathbf{S}_j$. The discrete form can be converted into the continuum form using Taylor expansion of the magnetisation around position i, details can e.g. be found in Abert (2019). Bulk DMI is then obtained as:

$$E_{\text{DMI}} = D \int \mathrm{d}V\, \mathbf{m} \cdot (\nabla \times \mathbf{m}). \tag{2.12}$$

The scalar coupling constant D depends both on the coupling constant d and the lattice spacing. Bulk DMI can give rise to the formation of Bloch skyrmions, shown in Fig. 2.6b.

Eq. 2.12 can also be expressed in terms of Lifshitz invariants:

$$\mathcal{L}_{ij}^{(k)} = m_i \partial_k m_j - m_j \partial_k m_i, \tag{2.13}$$

based on which the energy density takes the form (Ado et al., 2020):

$$e_{\mathrm{DMI}} = D\left(\mathcal{L}_{zy}^{(x)} + \mathcal{L}_{xz}^{(y)} + \mathcal{L}_{yx}^{(z)}\right). \tag{2.14}$$

The equivalence of the two equations can be directly seen by expanding the scalar and cross product in Eq. 2.12. Based on the form of the Lifshitz invariants present in the energy equation we qualitatively know types of magnetisation configurations that likely occur. For a Lifshitz invariant with three different indices, the magnetisation tends to form a helix propagating in k direction with the rotation of the magnetisation in the ij plane. For bulk DMI the propagation direction is normal to the plane of rotation.

Another common form of DMI is called interfacial DMI and occurs at the interface between a magnet and a non-magnetic heavy metal, where the latter has strong spin-orbit coupling. The interaction of two magnetic moments is mediated via a non-magnetic atom in the heavy-metal layer. For the interface normal pointing along z direction, the energy density takes the form (Ado et al., 2020):

$$e_{\mathrm{DMI,i}} = D\left(\mathcal{L}_{xz}^{(x)} + \mathcal{L}_{yz}^{(y)}\right), \tag{2.15}$$

or equivalently, the total energy is given as (Abert, 2019):

$$E_{\mathrm{DMI}} = D \int \mathrm{d}V\, \mathbf{m} \cdot \nabla m_z - m_z \nabla \cdot \mathbf{m}. \tag{2.16}$$

Here, the Lifshitz invariants describe helices where the propagation direction lies in the plane of rotation. Interfacial DMI can give rise to Néel skyrmions, shown in Fig. 2.6a.

2.3.3 Zeeman energy

Zeeman energy describes the interaction with an external magnetic field $\mathbf{H}_{\mathrm{ext}}$. It is known from classical electromagnetism and can be expressed as:

$$E_{\mathrm{Z}} = -\mu_0 \int \mathrm{d}V\, \mathbf{M} \cdot \mathbf{H}_{\mathrm{ext}}, \tag{2.17}$$

where μ_0 is the vacuum permeability. The Zeeman energy is minimal when magnetic moments are aligned parallel to the external field. Strong external fields can dominate most other energy contributions, leading to a fully saturated sample.

2.3.4 Demagnetisation energy

The dipole-dipole interaction of the spins is in micromagnetics described by the demagnetisation energy, also referred to as magnetostatic or stray-field energy. Dipole-dipole interaction is a comparatively weak, long-range interaction. It causes the magnetisation to form closed loops and minimise surface and volume charges, i.e. magnetisation at the sample surface aligns parallel to the surface. In ferromagnets, it is responsible for the formation of magnetic domains. In a microscopic sample, the combination of exchange interaction and demagnetisation can stabilise magnetic vortices, discussed in Sec. 2.8.2.

Demagnetisation can be described as the interaction of the magnetic moments with the demagnetisation field $\mathbf{H}_\mathrm{d}$ generated by the sample itself. The energy contribution from the stray field is (Hubert & Schäfer, 1998):

$$E_\mathrm{d} = -\frac{1}{2}\int \mathrm{d}V\, \mathbf{H}_\mathrm{d}\cdot\mathbf{M}, \tag{2.18}$$

where the factor 1/2 accounts for double counting. For individual magnetic dipoles $\mathbf{S}_j = \mathbf{S}(\mathbf{r}_j)$ located at position $\mathbf{r}_j$, the demagnetisation field is given as a sum of all individual dipole fields (Exl et al., 2020):

$$H_\mathrm{d}(\mathbf{r}_i) = \frac{1}{4\pi}\sum_{j\neq i}\left(3\frac{(\mathbf{S}_j\cdot\mathbf{r}_{ij})\mathbf{r}_{ij}}{r_{ij}^5} - \frac{\mathbf{S}_j}{r_{ij}^3}\right), \tag{2.19}$$

where $r_{ij} = |\mathbf{r}_{ij}| = |\mathbf{r}_j - \mathbf{r}_i|$ is the distance between spins $\mathbf{S}_i$ and $\mathbf{S}_j$.

In the continuum limit, the demagnetisation field $\mathbf{H}_\mathrm{d}$ can be derived from the macroscopic Maxwell equations. Here, we outline the important steps, the full derivation is e.g. given in Abert (2019) or Hubert and Schäfer (1998). In the absence of electric currents and external fields, Maxwell's equations describing magnetic fields have the form:

$$\nabla\cdot\mathbf{B} = 0, \tag{2.20}$$

$$\nabla\times\mathbf{H}_\mathrm{d} = 0. \tag{2.21}$$

According to Eq. 2.21, the demagnetisation field is nonrotational. Hence, $\mathbf{H}_\mathrm{d}$ can be defined via a magnetic scalar potential u:

$$\mathbf{H}_\mathrm{d} = -\nabla u. \tag{2.22}$$

With the magnetic flux $\mathbf{B}$ proportional to the sum of the magnetisation $\mathbf{M}$ and the demagnetisation field $\mathbf{H}_\mathrm{d}$, we obtain:

$$\nabla\cdot(-\nabla u + \mathbf{M}) = 0, \tag{2.23}$$

from which the scalar potential u can be obtained:

$$u(\mathbf{r}) = \frac{1}{4\pi}\left[\int_V \mathrm{d}\mathbf{r}'\,\frac{\rho(\mathbf{r}')}{|\mathbf{x}-\mathbf{x}'|} + \int_{\partial V}\mathrm{d}\mathbf{s}'\,\frac{\sigma(\mathbf{r}')}{|\mathbf{x}-\mathbf{x}'|}\right], \tag{2.24}$$

where $\rho(\mathbf{r}) = -\nabla \cdot \mathbf{M}(\mathbf{r})$ is the magnetic volume charge and $\sigma(\mathbf{r}) = \mathbf{M}(\mathbf{r}) \cdot \mathbf{n}$ is the magnetic surface charge. Based on Eq. 2.24, the demagnetisation field and the demagnetisation energy can be obtained using Eq. 2.22 and Eq. 2.18, respectively.

2.3.5 Magnetocrystalline anisotropy energy

Magnetocrystalline anisotropy favours alignment of the magnetisation parallel to certain crystallographic directions. The electronic orbitals in a material depend on the local crystal field and have an effect on the magnetisation via spin-orbit coupling. Two different types of favourable directions can be distinguished: easy axes and easy planes. A crystallographic direction is called easy axis if the total energy of the system is minimal when the magnetisation points along that axis. If magnetisation pointing along a crystallographic direction increases the total energy, the direction is called hard axis and the crystal has an associated easy plane perpendicular to that axis. The number and orientation of the easy/hard axes depends on the crystal structure. Easy/hard axes are undirected (Abert, 2019):

$$E_{\text{ani}}(\mathbf{m}) = E_{\text{ani}}(-\mathbf{m}). \tag{2.25}$$

Magnetocrystalline anisotropy is expressed in series expansions with empirical material constants. In the case of uniaxial anisotropy, present in hexagonal and tetragonal crystals, the energy density takes the form (Cullity & Graham, 2009):

$$e^{\text{u}}_{\text{ani}} = K_{\text{u0}} + K_{\text{u1}} \sin^2\theta + K_{\text{u2}} \sin^4\theta + \mathcal{O}(\sin^6\theta), \tag{2.26}$$

where K_{u0}, K_{u1} and K_{u2} are material constants and θ defines angle between the magnetisation direction and the easy/hard axis. Depending on the sign of K_{u1} and K_{u2} easy axis, easy plane, or "intermediate" easy cone magnetisation can be observed.

Materials with cubic crystal class have three orthogonal distinguished axes. The cubic anisotropy energy density is (Liu et al., 2017):

$$e^{\text{c}}_{\text{ani}} = K_{\text{c0}} + K_{\text{c1}} \left(m_x^2 m_y^2 + m_x^2 m_z^2 + m_y^2 m_z^2\right) + o\left(m_i^6\right). \tag{2.27}$$

The sign of the material constant K_{c1} determines the easy directions. For $K_{\text{c1}} > 0$ the system has three easy axes along the $\langle 100 \rangle$ directions. For $K_{\text{c1}} < 0$ the system has four easy axes along the $\langle 111 \rangle$ directions and the $\langle 100 \rangle$ directions are hard axes.

The anisotropy can take different forms for other crystal classes, at the surface of thin films, or at the interface to a different material. Furthermore, lattice defects or lattice deformations can also contribute to the anisotropy. Magnetocrystalline anisotropy is important for the formation of domain walls (Sec. 2.8.1).

2.4 Dynamic micromagnetism: Landau-Lifshitz-Gilbert equation

The dynamics of magnetic structures is described by the Landau-Lifshitz-Gilbert (LLG) equation (Landau & Lifshitz, 1935; Gilbert, 1955; Gilbert, 2004). It describes the dynamics of the magnetisation in an effective field:

$$\mathbf{H}^{\text{eff}} = -\frac{1}{\mu_0 M_\text{s}} \frac{\partial E}{\partial \mathbf{m}}. \tag{2.28}$$

The magnetisation dynamics is then in implicit form given as:

$$\frac{\partial \mathbf{m}}{\partial t} = -\gamma \mathbf{m} \times \mathbf{H}^{\text{eff}} + \alpha \mathbf{m} \times \frac{\partial \mathbf{m}}{\partial t}, \tag{2.29}$$

where $\gamma = \mu_0 \gamma_\text{e} \approx 2.2128 \times 10^5$ m/As is the reduced gyromagnetic ratio and α is the dimensionless Gilbert damping constant. In most materials $\alpha \ll 1$. Eq. 2.29 can be rewritten to an explicit form:

$$\frac{\partial \mathbf{m}}{\partial t} = -\frac{\gamma}{1+\alpha^2} \mathbf{m} \times \mathbf{H}^{\text{eff}} - \frac{\alpha\gamma}{1+\alpha^2} \mathbf{m} \times \left(\mathbf{m} \times \mathbf{H}^{\text{eff}}\right). \tag{2.30}$$

The LLG equation can be derived from classical Lagrangian mechanics, a detailed derivation can e.g. be found in Abert (2019) or Wegrowe and Ciornei (2012).

The effects of the two terms in the LLG equation on a single magnetic moment are shown in Fig. 2.1. The first term in Eq. 2.30 describes a stationary precession of the magnetisation around the effective field. This can be easily seen from the equation: the change of the magnetisation is proportional to $\mathbf{m} \times \mathbf{H}^{\text{eff}}$, which describes a vector perpendicular to both $\mathbf{m}$ and $\mathbf{H}^{\text{eff}}$. Hence, the term describes a torque on the magnetisation that causes the magnetisation to rotate around the effective field. The second term describes dissipative (damped) motion of the magnetisation towards the effective field. Again, this can be seen from the equation: first, the change in magnetisation is perpendicular to $\mathbf{m} \times \mathbf{H}^{\text{eff}}$, i.e. lies in the plane containing $\mathbf{m}$ and $\mathbf{H}^{\text{eff}}$. Second, the change in magnetisation is perpendicular to the magnetisation $\mathbf{m}$ and from the order of cross products and the additional minus sign we can see that it points towards the effective field $\mathbf{H}^{\text{eff}}$. Under the influence of both terms, the magnetisation $\mathbf{m}$ performs a damped precessional motion around the effective field $\mathbf{H}^{\text{eff}}$. The speed of convergence towards parallel alignment with the effective field depends on the strength of the damping parameter α.

The LLG equation fulfils the requirement of constant magnetisation $|\mathbf{m}| = 1$ (Abert, 2019). Intuitively, this can be understood from the fact that both the damping and the precession term contribute changes $\partial_t \mathbf{m}$ that are perpendicular to $\mathbf{m}$, i.e. act as torques, and hence only affect the direction of the magnetisation but not its magnitude.

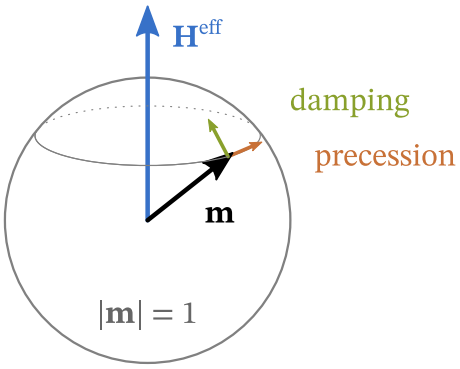

FIGURE 2.1: Effects of the damping and precession term in the LLG equation on the magnetisation direction.

2.5 Spin currents

Manipulation of the magnetisation with external parameters is of central importance for experiments and potential applications. So far, we have only discussed the effects of an external magnetic field on the magnetisation, the Zeeman energy. Interactions between the spins of conduction electrons and the local magnetic moments are a second possibility to manipulate the magnetic configuration. Depending on the current strength and polarisation, an applied spin current can lead to reduced damping, steady precession, or magnetisation switching. This type of all-electric manipulation is particularly appealing for applications, and is summarised under the term spintronics (Abert, 2019).

The effects of the interaction between spin currents and the magnetisation $\mathbf{m}$ can be incorporated into the LLG equation by adding a torque term $\mathbf{T}$ (Abert, 2019):

$$\frac{\partial \mathbf{m}}{\partial t} = -\gamma \mathbf{m} \times \mathbf{H}^{\text{eff}} + \alpha \mathbf{m} \times \frac{\partial \mathbf{m}}{\partial t} + \mathbf{T}. \tag{2.31}$$

The additional torque term can have different microscopic origins. Depending on its origin, we can distinguish between spin-orbit torques and spin-transfer torques. We give a brief overview of the different mechanisms and how they are included into the LLG equation. An in-depth discussion of spin-transfer torques can e.g. be found in Ralph and Stiles (2008), an in-depth discussion of spin-orbit torques in Gambardella and Miron (2011) or Manchon et al. (2019). In the simulations carried out in this work, we only consider spin-transfer torques in a magnetic sample with non-uniform magnetisation as described by the Zhang-Li model, see below.

Spin-transfer torque arises from current flowing through magnetic samples. If the conduction electron spin and the magnetisation are not collinear, the magnetic moments exert a torque on the electron spin. A similar torque of opposite sign is exerted on the magnetic moments, which is called spin-transfer torque (Ralph & Stiles, 2008). It can arise in two different set-ups: first, when electric current flows through a magnetic material with non-collinear magnetisation; second, in a multi-layer stack consisting of magnetic and non-magnetic layers when current

flows perpendicular to the stack. More general methods not limited to one specific set-up are also available (Abert, 2019).

The first set-up, in which the torque originates from current flowing through a single magnetic sample, is described by the Zhang-Li model (Zhang & Li, 2004; Bazaliy et al., 1998; Thiaville et al., 2005):

$$\mathbf{T} = -\mathbf{m} \times [\mathbf{m} \times (\mathbf{u} \cdot \nabla)\mathbf{m}] - \beta \mathbf{m} \times (\mathbf{u} \cdot \nabla)\mathbf{m}, \tag{2.32}$$

where

$$\mathbf{u} = \frac{P\mu_\mathrm{B} g}{2eM_\mathrm{S}(1+\beta^2)}\mathbf{j}_\mathrm{e} \tag{2.33}$$

is the spin-drift velocity. Here, $\mathbf{j}_\mathrm{e}$ is the electric current density, P is the polarisation, μ_B the Bohr magneton, g the electron g-factor, e the elementary charge, and β the non-adiabatic parameter. While the electron traverses the sample, its spin picks up the local magnetisation direction and carries it in current direction. If the magnetisation along this direction is noncollinear, the current flow will exert a spin-transfer torque. This can result in a movement of the whole magnetisation texture, and can e.g. be observed for domain walls (Freitas & Berger, 1985; Parkin et al., 2008) and skyrmions (Sampaio et al., 2013; Kang et al., 2016). The description within the Zhang-Li model is purely local and therefore not suitable for multi-layer systems (Abert, 2019).

Spin-transfer torques can also arise in multi-layer systems. In the typical case, two ferromagnetic layers are separated by a non-magnetic layer, and an electric current flows perpendicular to the layers, i.e. through the multi-layer stack. In this set-up, the first ferromagnetic layer acts as a spin filter and produces a spin-polarised current incident on the second layer. This current then exerts a torque on the second ferromagnetic layer. The effects in the second layer are described by the Slonczewski model (Slonczewski, 1996; Berger, 1996), in which the torque $\mathbf{T}$ takes the form:

$$\mathbf{T} = \tau_\mathrm{FL}\mathbf{m} \times \mathbf{p} + \tau_\mathrm{DL}\mathbf{m} \times (\mathbf{m} \times \mathbf{p}). \tag{2.34}$$

Here, $\mathbf{p}$ is the polarisation of the current. The coefficients $\tau_\mathrm{FL,TL}$ are given as (Abert, 2019):

$$\tau_\mathrm{FL} = \eta_\mathrm{FL}(\theta)\frac{j_\mathrm{e}\gamma\hbar}{2e\mu_0 M_\mathrm{s}} \tag{2.35}$$

$$\tau_\mathrm{DL} = \eta_\mathrm{DL}(\theta)\frac{j_\mathrm{e}\gamma\hbar}{2e\mu_0 M_\mathrm{s}}, \tag{2.36}$$

where θ is the angle between $\mathbf{m}$ and $\mathbf{p}$, j_e is the electric current density, and η_FL and η_DL are dimensionless functions that describe the angular dependence of the torque and depend on the geometry and materials of the multi-layer stack. The first term in Eq. 2.34 is commonly referred to as field-like term, because the torque results in a precession of the magnetisation around the polarisation direction similar to an effective field. The effect of the second term is called damping-like. Its effect is similar to the damping term in the LLG equation and aligns the magnetisation to the current polarisation.

Spin-orbit torques arise from current flowing through a non-magnetic layer with spin-orbit coupling adjacent to a ferromagnetic layer. Two different effects can contribute to the torque. First, a current flowing through the non-magnetic layer can result in a perpendicular spin current towards the interface via the spin Hall effect (Sinova et al., 2015). In the spin Hall effect, the spin-orbit coupling leads to a deflection of electrons with opposite spin and therefore a spin current perpendicular to the electric current. This spin current exerts a torque on the ferromagnetic layer. Second, current flowing parallel to an interface with broken inversion symmetry can lead to a spin-polarisation of the electrons at the interface. The electron spins can exert a torque on the ferromagnetic layer via exchange coupling (Manchon & Zhang, 2008). The resulting torque term in the LLG takes the same form as Eq. 2.34. For a more in-depth discussion, refer to Gambardella and Miron (2011) or Manchon et al. (2019).

2.6 Emergent electrodynamics and topological charge

In the previous section, we discussed the effects of spin currents on the local magnetic moments. Here, we discuss the effects on the electrons in more detail. We consider an adiabatic movement, i.e. the spin of the electron constantly adjusts to the direction of the local magnetisation while the electron traverses the magnetic structure. Under these conditions, the electron picks up a Berry phase (Berry, 1984; Onoda et al., 2004). We can easily understand the effects of the Berry phase by describing the electron movement in a different system (Everschor-Sitte & Sitte, 2014): we assume that the electron moves in a uniform background and additionally "feels" an *emergent* magnetic field $\mathbf{B}^{\mathrm{e}}$ and an *emergent* electric field $\mathbf{E}^{\mathrm{e}}$. The effects of the emergent fields resemble the influence of the Berry phase, which the electron picks up in the real system. The fields depend on the normalised local magnetisation $\mathbf{m}$ (Zhang & Zhang, 2009; Volovik, 1987; Bruno et al., 2004):

$$B_i^{\mathrm{e}} = \frac{\hbar}{2}\epsilon_{ijk}\mathbf{m}\cdot\left(\frac{\partial\mathbf{m}}{\partial r_j}\times\frac{\partial\mathbf{m}}{\partial r_k}\right), \tag{2.37}$$

$$E_i^{\mathrm{e}} = \hbar\mathbf{m}\cdot\left(\frac{\partial\mathbf{m}}{\partial r_i}\times\frac{\partial\mathbf{m}}{\partial t}\right), \tag{2.38}$$

where ϵ_{ijk} is the totally antisymmetric tensor. A full derivation of the emergent fields starting from the Berry phase can be found in Zhang and Zhang (2009). We can see that an emergent electric field can only occur if the magnetisation is time dependent, e.g. in a moving domain wall or skyrmion. An emergent magnetic field only occurs when the magnetisation is non-collinear in at least two directions, e.g. in a magnetic vortex or magnetic skyrmion. This condition is equivalent to the magnetisation having a non-trivial topological charge density, see below.

The emergent fields lead to Lorentz forces acting on the electrons that can be measured in experiments. The effects of the emergent electric field can e.g. be observed as electromotive force induced by domain wall motion (Yang et al., 2009) and in the dynamics of skyrmions (Zhang &

Zhang, 2009; Schulz et al., 2012). The emergent magnetic field leads to additional contributions to the anomalous Hall effect—sometimes also referred to as geometrical Hall effect or topological Hall effect—observed for various systems hosting skyrmions (Lee et al., 2009; Neubauer et al., 2009; Li et al., 2013; Hamamoto et al., 2015; Maccariello et al., 2018), colossal magnetoresistance manganites (Ye et al., 1999), geometrically frustrated ferromagnets (Taguchi et al., 2001), and magnetic hopfions (Göbel et al., 2020), amongst others. Note, that non-adiabatic processes, band structure effects, etc., have to be taken into account to quantitatively correctly describe the experimental results. The strength of the emergent magnetic field is in many materials on the order of several Tesla, thus comparable to externally applied magnetic fields, e.g. 2.5 T in MnSi (Schulz et al., 2012). In systems with very small skyrmions the emergent magnetic field can reach values up to several thousand Tesla, leading to a quantised topological Hall effect (Hamamoto et al., 2015; Göbel et al., 2017).

The emergent magnetic field is closely related to the topological charge S of the magnetisation structure, also called winding number, which can be used to classify e.g. skyrmions. The topological charge is defined as integral of the solid angle span by the magnetisation $\mathbf{m}$ (Kotiuga, 1989):

$$S = \frac{1}{4\pi} \iint \mathrm{d}^2 r \, \mathbf{m} \cdot \left(\partial_x \mathbf{m} \times \partial_y \mathbf{m} \right), \tag{2.39}$$

where we have picked the xy plane as an example. It counts how many times the magnetisation $\mathbf{m}$ wraps around the unit sphere. Comparing Eqs. 2.37 and 2.39, we can see that the topological charge S is equivalent to the flux of the emergent magnetic field $\mathbf{B}_\mathrm{e}$ through the integration plane. Hence, for magnetic objects with discrete topological charge, e.g. skyrmions, the flux of the emergent magnetic field is quantised and depends on the topological charge.

2.7 Numerical micromagnetism

Computational micromagnetism plays a central role in fundamental research and device development. The micromagnetic model, described in the previous sections, can only be solved analytically for some simple edge cases. More complicated solutions require numerical treatment, both, for the description of equilibrium states, i.e. configurations in local energy minima, and for the description of magnetisation dynamics expressed by the LLG equation.

Most numerical methods require a discretisation of the problem, both in space and time. The most popular mesh-based spatial discretisations are finite differences and finite elements, the former is used in this work. In finite differences (Fidler & Schrefl, 2000; Suess et al., 2006), space is divided into small cuboids on a regular grid. The cells are magnetised uniformly and one magnetic moment can be associated with each discretisation cell. In the equations, partial derivatives are replaced with finite difference quotients. This converts the partial differential equation into a set of algebraic equations. For complicated geometries, the discretisation with cuboids on a regular grid is not very well suited because it cannot well resemble curved

geometries. The finite-element method (Fidler & Schrefl, 2000; Suess et al., 2006) is better suited to model complex geometries. Here, space is divided into irregular elements, commonly tetrahedrons in three dimensions, which can model arbitrary geometries. A set of basis functions is then defined on these elements. The solution of the partial differential equation can be expressed as a superposition of these basis functions. This turns the partial differential equation into a set of linear equations, which can be solved using standard linear algebra techniques. The main drawback of the finite-element method is the complicated mathematical background and hence increased complexity of the numerical code. Additional difficulties can arise from the mesh generation.

When discretising space, the cell size has to fulfil certain conditions, independent of the method. First, magnetisation is assumed to be uniformly distributed in micromagnetics. Therefore, the discretisation size must be significantly larger than the crystal lattice to ensure that the locally varying crystal field averages out and lattice effects do not affect the averaged effective magnetisation. Second, micromagnetics assumes that the angle of the magnetic moments of neighbouring cells is small, i.e. the magnetisation changes gradually. Therefore, the discretisation cell size must be much shorter that typical length scales in the system, such as exchange length, domain wall width, and helix length. The different length scales arise from the competition of different contributions to the total energy. They are a measure for the relative strength of the different energy contributions.

The exchange length, defined as (Exl et al., 2020):

$$l_{\mathrm{ex}} = \sqrt{\frac{A}{\mu_0 M_{\mathrm{s}}^2}}, \tag{2.40}$$

is a measure for the competition between exchange and demagnetisation energy. On sufficiently small length scales, the exchange interaction dominates the magnetisation and all magnetic moments align parallel.

The domain wall width, for Bloch walls defined as (Exl et al., 2020):

$$l_{\mathrm{K}} = \sqrt{\frac{A}{K}}\,, \tag{2.41}$$

determines the width of the transition region between two magnetic domains. It arises from the competition between exchange and anisotropy energy.

The helical length (Wilhelm et al., 2012):

$$l_D = \frac{4\pi A}{|D|} \tag{2.42}$$

describes the effect of exchange and Dzyaloshinskii-Moriya interaction. It determines the periodicity of magnetic helices or cones forming in helimagnetic systems.

2.8 Topological objects

A number of different magnetic configurations can form as a result of the competition between the different contributions to the total energy. In many systems some interactions are not present or can be neglected because their contribution is minor and irrelevant. Starting from a ferromagnetic system with only exchange interaction where all magnetic moments are aligned, many new configurations can be obtained by adding additional interactions. Examples are domain walls, vortices, skyrmions, and Bloch points, shown in Fig. 2.2.

In the following sections, we discuss these different objects. The main focus of this thesis is on Bloch points, hence we will provide the most details here. Domain walls, vortices, and skyrmions have been studied extensively, and only a basic explanation of these objects, some central features, and references to relevant literature and reviews can be given. A more comprehensive overview would go beyond the scope of this thesis.

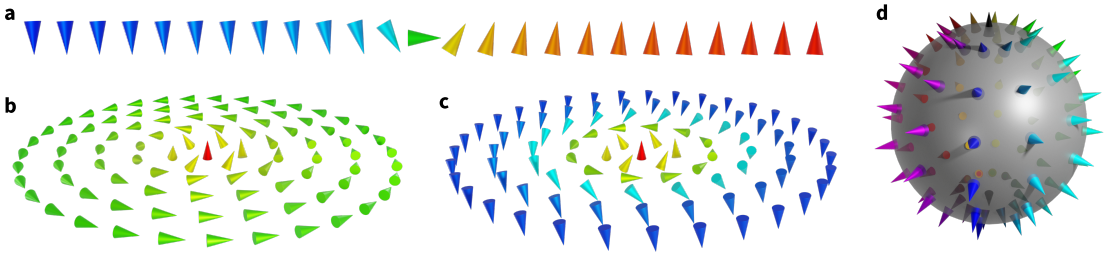

FIGURE 2.2: Selected magnetic configurations: (a) domain wall of Néel type, (b) out-of-plane vortex, (c) Bloch skyrmion, and (d) diverging or hedgehog Bloch point.

2.8.1 Domain wall

On small length scales, ferromagnetic materials are dominated by the exchange interaction, which causes uniform alignment of magnetic moments. However, exchange is a short-range interaction. On larger lengths, roughly starting on the micrometre length scale, the effects of demagnetisation energy gain importance. Magnetic moments on these larger length scales tend to form closed flux lines to avoid magnetic bulk or surface charges. This leads to the formation of magnetic domains. Each domain has a uniform magnetisation, resulting from the strong exchange interaction. The magnetisation of different domains is oriented along different directions, minimising the demagnetisation energy. The orientation of the different domains is commonly determined by the system's anisotropy. The region in between two domains is called domain wall. Here, the magnetisation gradually rotates from the orientation in one domain to the orientation in the other domain. Domain walls can occur in different types, such as Bloch walls, Néel walls, vortex walls, or cross-tie walls. Detailed reviews can e.g. be found in Malozemoff and Slonczewski (1979), Hubert and Schäfer (1998), Thiaville and Nakatani (2014), Thiaville and Miltat (2018) and Okuno (2020).

The internal structure of a domain wall depends on a number of parameters. Material parameters such as exchange and anisotropy, which together can stabilise the domain wall, determine the wall width and are important for its internal structure. The wall width depends on the relative strength of the two contributions (see also Eq. 2.41). Exchange interaction prefers aligned moments, hence thick walls with a gradual rotation and small misalignment between neighbouring moments. Anisotropy favours alignment along certain crystallographic directions. The magnetic domains align with these preferred directions. Inside the wall, the moments are not aligned with the preferred crystal directions. This additional anisotropy energy contribution decreases with decreasing wall width, hence anisotropy prefers narrow walls. The shape of the magnetic sample also affects the type of domain wall via the demagnetisation field.

The two simplest domain-wall configurations are shown in Fig. 2.3. Figure 2.3a shows the magnetisation of a Bloch domain wall. The figure shows two different cross-sections in the xy and xz plane. For simplicity, only a single layer of magnetic moments is shown in the z direction. Two domains at $x \ll 0$ with $\mathbf{m} = (0, -1, 0)$ and $x \gg 0$ with $\mathbf{m} = (0, 1, 0)$ are separated by a domain wall centred at $x = 0$, extending through the sample in y and z direction. In a Bloch wall, the magnetisation rotates in the plane of the domain wall, here the yz plane. In the centre of the domain wall, at $x = 0$, the moments point along $\mathbf{m} = (0, 0, 1)$. Bloch walls are commonly observed in bulk systems (Liu et al., 2017).

In thin films, Néel walls have a lower energy than Bloch walls (Liu et al., 2017). The magnetisation in a Néel wall (Fig. 2.3b) rotates in a plane perpendicular to the domain wall. In the figure, the domains are again oriented along $\mathbf{m}_{x\ll 0} = (0, -1, 0)$ and $\mathbf{m}_{x\gg 0} = (0, 1, 0)$ and the magnetisation near $x = 0$ rotates in the xy plane. At $x = 0$, the moments point along $\mathbf{m} = (1, 0, 0)$. Compared to the Bloch wall, the surface charge of the Néel wall is reduced because no moments point out of the xy plane.

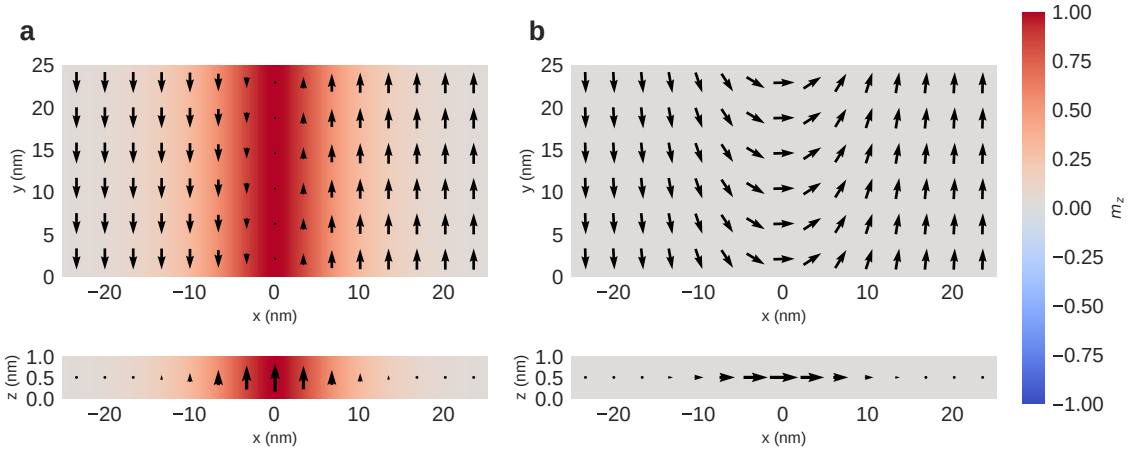

FIGURE 2.3: Magnetisation configuration of a Bloch wall (a) and a Néel wall (b). Two different cross-sections in the xy plane and xz plane are shown for each configurations.

Domain walls are important for the macroscopic properties of magnetic materials (Hubert & Schäfer, 1998). In particular, they can affect hysteresis behaviour, which is of crucial importance for many applications. On the nanoscale, domain walls have been proposed for logic devices (Allwood et al., 2005) and a novel type of data storage, so-called racetrack memory (Parkin et al., 2008; Bläsing et al., 2020). In the racetrack setup, a nanowire contains a number of domain walls that can be moved along the wire using spin currents. The racetrack has fixed read and write elements to which the data is moved with these currents. Racetrack memory would allow for dense three-dimensional storage devices with fast access time and non-volatile storage. Racetrack memory requires the spacing between the domain walls to stay constant because the length of the individual domains encodes the number of bits. Consequently, changes in spacing lead to data loss. This fixed spacing is one of the major experimental challenges. A second difficulty for domain-wall based applications is the fact that the maximum achievable speed of domain walls is limited by the Walker breakdown (Schryer & Walker, 1974; Nakatani et al., 2003): above a certain velocity, typically on the order of hundreds of metres per second, the domain wall speed decreases significantly because the domain wall starts to oscillate while moving. Circular geometries have been proposed to prevent the Walker breakdown (Yan et al., 2011; Hertel, 2016). Experimental realisation (Wartelle et al., 2019) showed a more complex behaviour including creation of Bloch points.

2.8.2 Vortex

A vortex is a two-dimensional magnetisation configuration where the magnetic moments rotate around a single point, the vortex core. The magnetic moments near the vortex core point out of the plane, all other moments lie in the vortex plane. The magnetic moments of a vortex span a solid angle of 2π. Hence, a vortex has a topological charge $S = \pm 1/2$. A vortex can have two different polarisations (core orientations) $p = \pm 1$ and two different circularities $c = \pm 1$. In total, four different configurations exist. Vortices can be stabilised solely through the competition between exchange and demagnetisation energy, magnetocrystalline anisotropy is not required. Due to the absence of chiral energy terms such as DMI, the vortex has no energetically preferred chirality. Without external magnetic field all four configurations have equal energy. (Liu et al., 2017)

A second similar object with topological charge $S = \pm 1/2$ is the antivortex. Vortex and antivortex have a different symmetry: ignoring the crystal symmetry, the vortex is rotationally symmetric; the antivortex has a two-fold symmetry. This is a result of the opposite sense of rotation of the magnetic moments on a circle around the vortex or antivortex core. When we express the orientation of the magnetic moments of the vortex and antivortex (centred at the origin) in cylindrical coordinates, we obtain for the angular component (Behncke et al., 2018):

$$m_\Phi(\phi) = \pm\phi + \frac{c\pi}{2}, \tag{2.43}$$

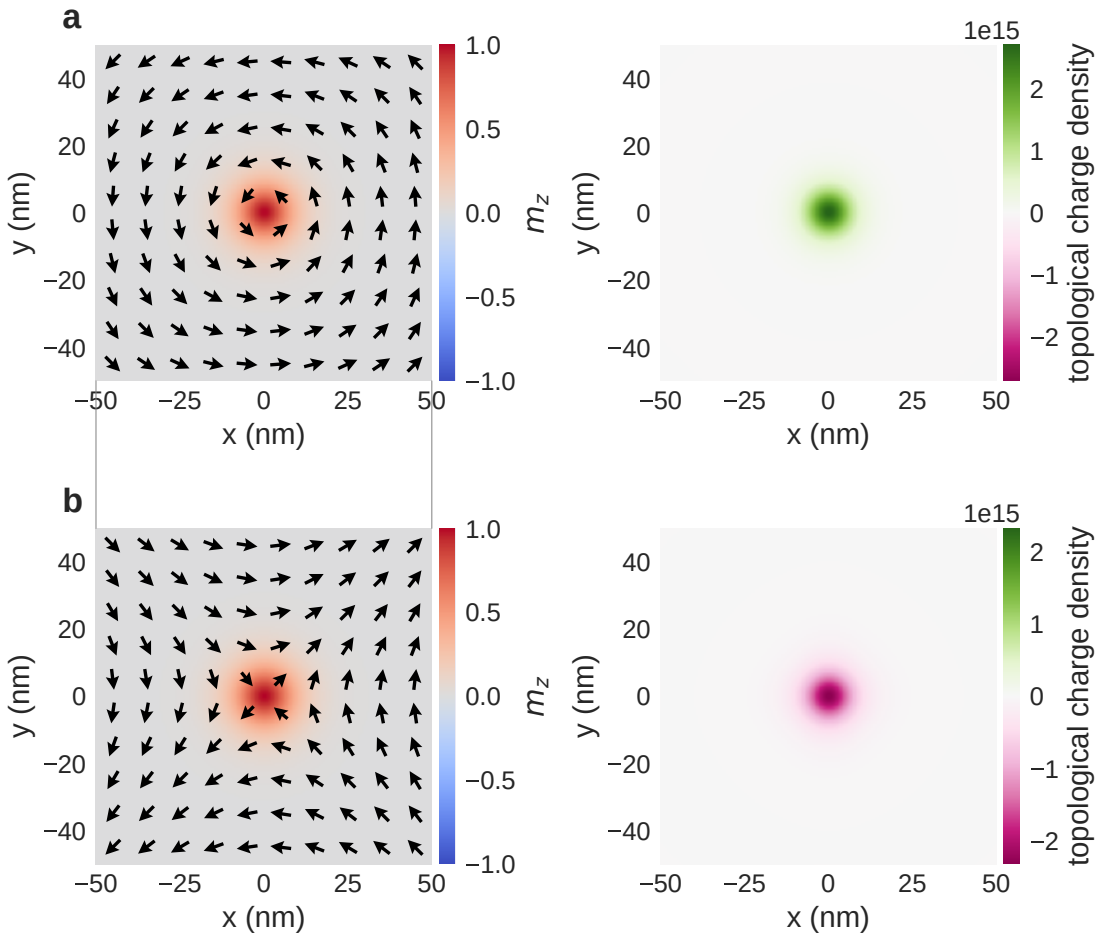

FIGURE 2.4: Magnetisation configuration and topological charge density of a vortex (a) and an antivortex (b). A larger sample containing vortex and antivortex, as indicated with the grey lines, would be topologically trivial.

where c is the circularity, and ϕ the angular component of the position vector of the magnetic moments. The positive solution corresponds to vortices, the negative solution to antivortices. For the vortex only two values $c = \pm 1$ are allowed and determine the circularity of the vortex, as mentioned above. For the antivortex any value $c \in [-2, 2)$ is allowed and determines the orientation of the antivortex. For an in-depth review of vortices and antivortices we refer to Behncke et al. (2018) and Pues and Meier (2018), respectively.

Figure 2.4a shows an example for a vortex with polarisation $p = +1$ and circularity $c = +1$. The left plot shows the magnetisation in the xy plane containing the vortex, the right plot shows the corresponding topological charge density. The main contributions to the total topological charge $S = 1/2$ come from the magnetisation near the vortex core, located at $x = 0$ and $y = 0$, where the misalignment of neighbouring moments is largest. Figure 2.4b shows the corresponding antivortex with $p = +1$ and $c = +1$. The topological charge density is again

concentrated near the core, its sign is reversed. The total topological charge of the antivortex is $S = -1/2$.

Combining a vortex and an antivortex in a system can result in a topologically trivial configuration with $S = 0$. An example is indicated with the grey lines connecting Fig. 2.4a and b. We assume to have a rectangular nanostrip with the vortex and antivortex shown in the two subfigures, separated by $\Delta y = 100\,\text{nm}$. Starting from this configuration, we can continuously deform the vector field to annihilate the vortex-antivortex pair by, in a thought experiment, moving vortex and antivortex towards each other. We end up with a ferromagnetic configuration with moments pointing in $-x$ direction.

Vortices and antivortices have initially been studied in the context of domain walls (Hubert & Schäfer, 1998). In addition to the simple Bloch and Néel wall discussed in the previous section, one or multiple vortices can also occur in the internal wall structure. Examples are cross-tie walls (Huber et al., 1958; Middelhoek, 1963) consisting of a series of vortices and antivortices or vortex walls (Thiaville et al., 2005; Nakatani et al., 2005) containing a single vortex, which can occur in nanowires. More recently, isolated vortices and antivortices have been studied more extensively (Shinjo et al., 2000; Wachowiak et al., 2002; Kamionka et al., 2010; Martens et al., 2012; Haldar & Buchanan, 2013; Pues et al., 2014). Vortices have been proposed for a number of applications, such as spin-torque oscillators (Lebrun et al., 2015, 2017), (anti)vortex based random access memory (Bohlens et al., 2008; Drews et al., 2009), spin wave emitters (Wintz et al., 2016), and even applications in cancer treatment (Kim et al., 2010).

2.8.3 Skyrmion

A magnetic skyrmion is a two-dimensional, swirl-like configuration. Magnetic moments in the skyrmion core and in the periphery point in opposite direction. In between, magnetisation gradually rotates from one towards the other direction. Skyrmions have a non-trivial topological charge. In three-dimensional systems, they form so-called skyrmion tubes, i.e. the 2D skyrmion is trivially extended in the third dimension.

Skyrmions were initially predicted in the context of particle physics (Skyrme & Schonland, 1961; Skyrme, 1962). Since then, they have been found in many systems, e.g. quantum Hall systems (Sondhi et al., 1993), Bose-Einstein condensates (Al Khawaja & Stoof, 2001), liquid crystals (Fukuda & Žumer, 2011), and magnetism (Bogdanov & Yablonskiui, 1989; Mühlbauer et al., 2009). Magnetic skyrmions can exist as isolated particles (Yu et al., 2010) or form lattices (Mühlbauer et al., 2009). Since their experimental discovery, magnetic skyrmions have been studied extensively. Details can be found in one of the many reviews, e.g. Nagaosa and Tokura (2013), Finocchio et al. (2016), Wiesendanger (2016), Kang et al. (2016), Han (2017), Fert et al. (2017), Garst et al. (2017), Jiang et al. (2017b), Everschor-Sitte et al. (2018), Bogdanov and Panagopoulos (2020), Göbel et al. (2021), Li et al. (2021) and Wang et al. (2022b).

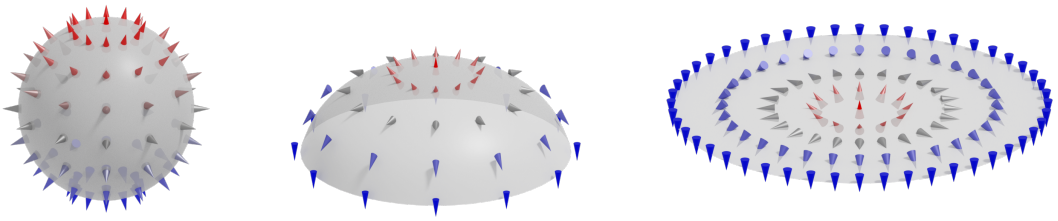

FIGURE 2.5: The magnetisation configuration of a Néel skyrmion can be obtained by projecting a hedgehog magnetisation on a sphere (left) onto a plane (right).

Magnetic skyrmions can form in helimagnetic materials due to the competition between exchange interaction and DMI. Without external magnetic fields, these materials usually have a helical or conical background and skyrmions are meta-stable configurations. The skyrmion phase can be stabilised by applying an external magnetic field (Yu et al., 2011). Skyrmions can also be the ground state without external field if the sample has a finite size (Beg et al., 2015).

Skyrmions are characterised by a non-trivial, quantised topological charge $S = \pm 1$. This implies that the magnetisation wraps the unit sphere exactly once. Understanding this connection is straight-forward: the magnetisation configuration of a skyrmion can be obtained by projecting the magnetisation on a sphere onto a plane. Figure 2.5 demonstrates this for a Néel skyrmion, which we obtain when starting from a hedgehog.

The magnetisation of a skyrmion can be approximated with the following simplified equation (Göbel et al., 2021):

$$\mathbf{m}(\mathbf{r}) = \begin{pmatrix} \cos(m\phi + \gamma)\sin(\pi r/r_0) \\ \sin(m\phi + \gamma)\sin(\pi r/r_0) \\ p\cos(\pi r/r_0) \end{pmatrix} \qquad 0 < r < r_0, \tag{2.44}$$

where m is the vorticity, γ is the helicity, and r_0 the skyrmion radius. The position $\mathbf{r}$ of the magnetic moments is expressed in polar coordinates:

$$r = |\mathbf{r}| = \sqrt{x^2 + y^2} \tag{2.45}$$

$$\tan(\phi) = \frac{y}{x}. \tag{2.46}$$

The true radial dependence of the out-of-plane component of the magnetisation in Eq. 2.44 is approximated with a simple cosine dependency. In a realistic system, the radial profile depends on the interaction parameters, the sample geometry, defects, and other quasiparticles (Göbel et al., 2021). The helicity γ defines the angle between the in-plane component of the magnetisation and the x direction. It determines the plane of rotation of the magnetisation when moving from the skyrmion core to the periphery. For $\gamma = 0$ magnetic moments at $m_z = 0$ point in radial direction, for $\gamma = \pi/2$ magnetic moments at $m_z = 0$ are perpendicular to

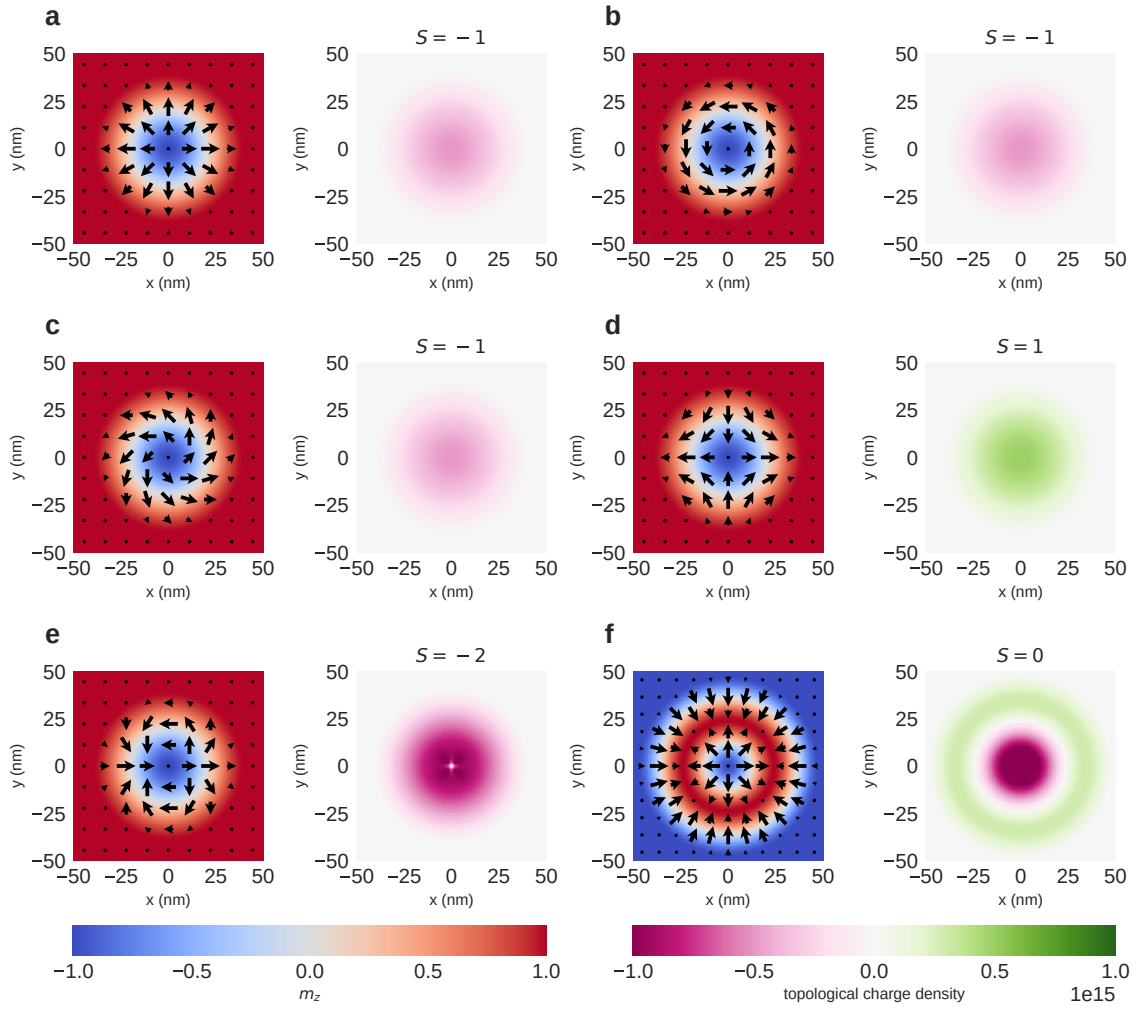

FIGURE 2.6: Different skyrmion configurations based on Eq. 2.44: (a) Néel skyrmion, (b) Bloch skyrmion, (c) mixed-helicity skyrmion, (d) anti-skyrmion, (e) higher-order skyrmion, (f) target skyrmion. The figure shows the magnetisation configuration, the topological charge density, and the topological charge.

the radial direction. The vorticity m describes the circulation of the magnetisation around the skyrmion core. It counts the number of 2π rotations of the in-plane component of the magnetisation, when moving around the skyrmion core on a closed circle (e.g. at $m_z = 0$). The sign determines the direction of rotation of the magnetisation.

Figure 2.6 shows skyrmion profiles for different values of vorticity m and helicity γ. In the figure, we fix the core polarisation to $p = -1$ and the radius $r_0 = 40\,\text{nm}$, except for Fig. 2.6f where we use $r_0 = 24\,\text{nm}$. For each configuration we show the magnetisation profile and the corresponding topological charge density.

The first solution, obtained for $m = 1$ and $\gamma = 0$, is called Néel skyrmion (Fig. 2.6a). The magnetisation in a Néel skyrmion rotates in a plane parallel to the radial direction, similar to a Néel domain wall. The topological charge density is comparatively large inside the skyrmion and approaches zero for $r \to r_0$. Importantly, we see a non-zero topological charge density in

the entire area covered by the skyrmion. This is qualitatively different from a vortex where we only obtain non-zero contributions near the vortex core. The integrated topological charge is $S = -1$, the sign is a result of the negative polarisation. Néel skyrmions can be obtained in systems with interfacial DMI, such as Fe/Ir(111) (Heinze et al., 2011).

A second type of skyrmion is the Bloch skyrmion (Fig. 2.6b), obtained for $m = 1$ and $\gamma = \pi/2$. Here, the magnetisation rotates in a plane perpendicular to the radial direction, similar to a Bloch domain wall. The topological charge density and topological charge are identical to the Néel skyrmion. Bloch skyrmions can be found in systems with bulk DMI, e.g. FeGe (Yu et al., 2011).

Figure 2.6c shows a mixed-helicity skyrmion, obtained for $m = 1$ and $\gamma = \pi/4$. It is a mixture of Néel and Bloch skyrmion. Again, its topological charge is $S = -1$ and the topological charge distribution matches that of the Néel and the Bloch skyrmion.

Fig. 2.6d shows an anti-skyrmion, obtained for $m = -1$ and $\gamma = 0$. The anti-skyrmion has the opposite topological charge of the skyrmion, here $S = +1$ because of the negative polarisation. Due to the negative vorticity, the anti-skyrmion has a two-fold symmetry (in a continuous model). This is different from the skyrmions discussed in Fig. 2.6a–c, which are rotationally symmetric. Anti-skyrmions can e.g. be observed in materials with crystal class D_{2d} (Jena et al., 2020).

Higher-order skyrmions have a vorticity $m = k$ with $|k| > 1$, i.e. the magnetisation on a circle around the core rotates k times as we move around the core once. Figure 2.6e shows the simplest case for $k = 2$ and $\gamma = 0$. The topological charge is equivalent to the total winding determined by k, in the example $S = -2$. (Göbel et al., 2021)

Target skyrmions are characterised by multiple π rotations of the out-of-plane component between the skyrmion core and the periphery. Figure 2.6f shows an example for a total winding of 2π, i.e. the magnetisation in the skyrmion core and the periphery points in the same direction. Here, the two nested skyrmions have the opposite topological charge density and the overall topological charge cancels out, $S = 0$. This specific configuration is also sometimes called skyrmionium (Everschor-Sitte et al., 2018).

Magnetic skyrmions are under extensive scrutiny both as interesting objects for fundamental research and for potential applications. Skyrmions can be manipulated using external fields (Moutafis et al., 2009; Büttner et al., 2015), spin torques (Jiang et al., 2015; Woo et al., 2016; Litzius et al., 2017; Jiang et al., 2017a; Wang et al., 2022a), or temperature gradients (Mochizuki et al., 2014; Pinna et al., 2018; Zázvorka et al., 2019; Wang et al., 2020). They are investigated as an alternative realisation of racetrack memory (Fert et al., 2013; Tomasello et al., 2014; Zhang et al., 2015b; Müller, 2016; Chen & Roy, 2017; Müller, 2017; Suess et al., 2018). Skyrmions could be used for novel for spintronic logic devices (Zhang et al., 2015a; Xing et al., 2016; He et al., 2017; Luo et al., 2018), probabilistic computing (Pinna et al., 2018; Zázvorka et al., 2019), neuromorphic computing (Grollier et al., 2016; Huang et al., 2017), and reservoir computing (Prychynenko

et al., 2018; Bourianoff et al., 2018). Beyond computing or storage applications, skyrmions have been proposed for use in radio-frequency emitters (Carpentieri et al., 2015), microwave detectors (Finocchio et al., 2015), and magnonic crystals (Ma et al., 2015).

2.8.4 Bloch point

A Bloch point is a single discontinuous point in the magnetisation configuration where the magnetisation vanishes (Feldtkeller, 1965; Döring, 1968). Characterising property of the Bloch point is that the magnetic moments on any closed surface enclosing the Bloch point span the entire solid angle. Hence, the surrounding magnetisation structure has a non-trivial topology (Mermin, 1979; Kotiuga, 1989; Zou et al., 2020; Tejo et al., 2021). The magnetisation around a Bloch point can have infinitely many different topologically equivalent configurations (Malozemoff & Slonczewski, 1979). We discuss some common configurations later in this section. Bloch points can also be found in other systems such as liquid crystals (Chandrasekhar & Ranganath, 1986).

We note the following on the use of the word Bloch point in this thesis. Technically, the Bloch point is just the point of vanishing magnetisation. When discussing properties of a magnetisation configuration containing a Bloch point, we are however interested in the Bloch point and its larger surrounding. Therefore, we use the term Bloch point to refer to the point singularity and the surrounding magnetisation. This can be done because the Bloch point affects the surrounding magnetisation at arbitrary distance due to its topology (Malozemoff & Slonczewski, 1979), given that there are no other particle-like objects in the considered volume.

Computationally, the internal structure of Bloch points has been studied in detail using both micromagnetic (Thiaville et al., 2003) and atomistic simulations (Andreas et al., 2014). Andreas et al. (2014) have used a combined atomistic and micromagnetic code, where the atomistic model is used in the vicinity of the Bloch point where the magnetisation changes rapidly. Both types of simulations produce similar results for the static Bloch-point structure (Jourdan, 2008). The Bloch-point energy depends on the location of the Bloch point in the non-uniform lattice potential, which leads to pinning of the Bloch point in the lattice potential. This pinning can directly be seen in atomistic simulations (Kim & Tchernyshyov, 2013; Hertel & Andreas, 2015). In a continuous micromagnetic model no pinning would occur. In micromagnetic simulations, the pinning is re-introduced through the discretisation (Thiaville et al., 2003; Im et al., 2019; Gong et al., 2021). However, the pinning in micromagnetic simulations depends on the discretisation cell size.

Elías and Verga (2011) analytically derived the magnetisation structure around a Bloch point in a system with exchange, demagnetisation and Landau terms. They showed that such a system can host two types of Bloch points, diverging and circulating Bloch points, and that the latter has a lower energy. Pylypovskyi et al. (2012) analytically derived the twist angle of

the circulating Bloch point and obtained a value of 105°, which is in good agreement with micromagnetic simulations.

Theoretical and numerical methods generally work at $T = 0$, where the saturation magnetisation M_s is fixed. At elevated temperatures, the magnitude of the magnetisation can vary locally and in the close vicinity of the Bloch point decreases compared to the average magnetisation. The effects on the Bloch point have been studied theoretically (Khodenkov, 2010) and with micromagnetic simulations at elevated temperatures using the Landau-Lifshitz-Bloch equation (Lebecki et al., 2012). The reduction of the magnetisation around the Bloch point lowers its total energy and makes thermal nucleation more likely (Khodenkov, 2010).

Experimentally, the internal structure of static Bloch points was measured recently using X-ray nanotomography (Donnelly et al., 2017; Hierro-Rodriguez et al., 2020; Donnelly et al., 2021; Rana et al., 2023; Hermosa et al., 2023). In the experiments, a resolution of 25 nm and 10 nm was achieved in Donnelly et al. (2017) and Rana et al. (2023), respectively. Im et al. (2019) measured Bloch-point dynamics using time-resolved transmission X-ray microscopy. They studied Bloch points embedded in magnetic vortices in asymmetric permalloy disks. They observed motion of the Bloch point when applying a magnetic field and found that the Bloch point affects the motion of the whole vortex structure in which the Bloch point is embedded.

Bloch points can exist both as stable configurations and as transient objects mediating several magnetisation reversal processes. They have initially been studied in the context of magnetic bubbles (Slonczewski, 1975; Hasegawa, 1975; Malozemoff & Slonczewski, 1979; Kufaev & Sonin, 1989; Masseboeuf et al., 2009), where Bloch points can occur in Bloch lines inside domain walls. Their existence and dynamic properties inside domain walls have been studied experimentally since the 1980s (Jantz et al., 1981; Zubov et al., 1988; Kabanov et al., 1989; Zubov et al., 1990; Thiaville & Miltat, 1994), the internal structure however could not be resolved in these experiments. Bloch points play an important role in vortex domain walls in cylindrical nanowires in which they have been studied theoretically (Wieser et al., 2004; Piao et al., 2013; Jamet et al., 2015; Hertel, 2016; Askey et al., 2022; Moreno et al., 2022; Caso et al., 2023) and experimentally (Da Col et al., 2014). Sáez et al. (2022a, 2022b) showed that thickness modulations of the nanowire can be used to control the location of the Bloch point and stabilise it against external fields. Bloch points can also exist as metastable states in nanospheres (Pylypovskyi et al., 2012). Interaction between Bloch points in nanospheres via their stray field is investigated in Zambrano-Rabanal et al. (2023), where the authors find that a Bloch point in a nanosphere creates a quadrupole magnetic field. Depending on their relative orientation, the resulting interaction between two Bloch points, each in a nanosphere, can be attractive or repulsive. Two systems combining skyrmions and Bloch points are chiral bobbers (Rybakov et al., 2015; Zheng et al., 2018; Ahmed et al., 2018; Birch et al., 2020) and dipole strings (Müller et al., 2020; Savchenko et al., 2022). The former is a skyrmion tube starting on a material surface that ends in a Bloch point, the latter can be understood as a short skyrmion tube that starts and ends in a Bloch point. Beg et al. (2019) recently predicted the existence of a stable Bloch point in two-layer nanodisks, where the two layers have opposite

material chirality. In this system, the Bloch point forms at the layer interface and is stabilised through the material's chirality. As a result, the energy of the Bloch-point configuration is lower than that of a simpler vortex extending throughout the whole system, which would be the ground state in a single-layer nanodisk of similar size. Different from Bloch points forming in long nanocylinders, the demagnetisation energy in the two-layer system would not be strong enough to stabilise the Bloch-point configuration. Charilaou (2020) studied a Bloch point embedded between two chiral bobbers in chiral nanocuboids and numerically showed that the location of the Bloch point can be controlled with an externally applied magnetic field.

Periodic lattices of Bloch points with alternating opposite topological charge, referred to as Bloch points and anti-Bloch points, have been measured experimentally in MnGe (Kanazawa et al., 2011, 2012; Tanigaki et al., 2015; Kanazawa et al., 2017, 2020) and $MnSi_xGe_{1-x}$ (Fujishiro et al., 2019; Aji et al., 2023). The Bloch-point crystals can form in two different configurations, a tetrahedral $4q$ lattice and a cubic $3q$ lattice. Possible stability mechanisms and the microscopic origin of the different lattices have theoretically been studied in Okumura et al. (2020), Shimizu et al. (2021), Paradezhenko et al. (2022) and Kato and Motome (2023). Fujishiro et al. (2020) summarises many of the results and discusses ways of manipulating these systems. Okumura et al. (2020) have also studied motion of Bloch points in the Bloch point crystal when applying an external magnetic field using Monte-Carlo simulations. They find that the Bloch points move in an applied field and observe repulsion and pair annihilation depending on the field strength.

The simplest dynamical process involving the formation of Bloch points is the reversal process of a uniformly magnetised ferromagnetic cylinder (Hertel & Kirschner, 2004). During the reversal process, Bloch points are generated on the central axis of the cylinder and mediate the reversal of the magnetisation on the central axis. The authors observed Bloch-point pair creation and annihilation in their simulations. The occurrence of Bloch points has been observed in the magnetisation reversal of domain walls (Hillebrands & Thiaville, 2006; Piao et al., 2013; Vazquez, 2015; Hertel, 2016; Wartelle et al., 2019). Bloch points are of central importance for vortex core reversal (Thiaville et al., 2003; Niedoba & Labrune, 2005; Van Waeyenberge et al., 2006; Hertel et al., 2007; Vila et al., 2009; Wohlhüter et al., 2015; Noske et al., 2015; Pylypovskyi et al., 2015), antivortex core reversal (Xing et al., 2008) and vortex-antivortex annihilation (Hertel & Schneider, 2006). Bloch points are also involved in skyrmion dynamics such as switching of skyrmions (Schütte & Rosch, 2014; Beg et al., 2015; Liu et al., 2015) and skyrmion creation and annihilation (Li et al., 2020).

The two-layer system proposed by Beg et al. (2019) is studied in more detail in this thesis. The concept of a Bloch point in the two-layer system is explained in Fig. 2.7, where we start from vortex configurations in single-layer materials and then stack them on top of each other to obtain the Bloch-point configuration of the magnetisation field. Figure 2.7a schematically shows the four possible vortex configurations that we can find in a thin layer of ferromagnetic material due to the competition between ferromagnetic exchange and demagnetisation energy,

as discussed in Sec. 2.8.2. The vortex core with polarisation P, pointing in the out-of-plane direction, can either point along $+z$ for $P = +1$ or along $-z$ for $P = -1$, and, independently, the circularity c of the magnetisation around the vortex core can either be clockwise ($c = -1$) or anticlockwise ($c = +1$). The product of polarisation and circularity can be defined as vortex chirality. In a simple ferromagnet, all four configurations are energetically equivalent. By adding DMI to the system, the relation between polarisation and circularity is fixed through the material chirality, i.e. the sign of the DMI constant D: for a given D only two of the four vortex realisations are energetically favourable.

Figures 2.7b and c show how a Bloch-point configuration can be realised by stacking vortex configurations with the same circularity and opposite polarisation on top of each other. The Bloch point emerges at the interface between the two vortex cores of opposite polarisation. The exchange coupling across the comparatively large interface enforces the same circularity in both layers. In layers with opposite material chirality, the vortices therefore have opposite polarisation and the Bloch point can be stable despite the high exchange energy density near the singularity. Two different Bloch-point types can be realised. When the magnetisation of the vortex cores point toward each other, we obtain a head-to-head Bloch point (HH), shown

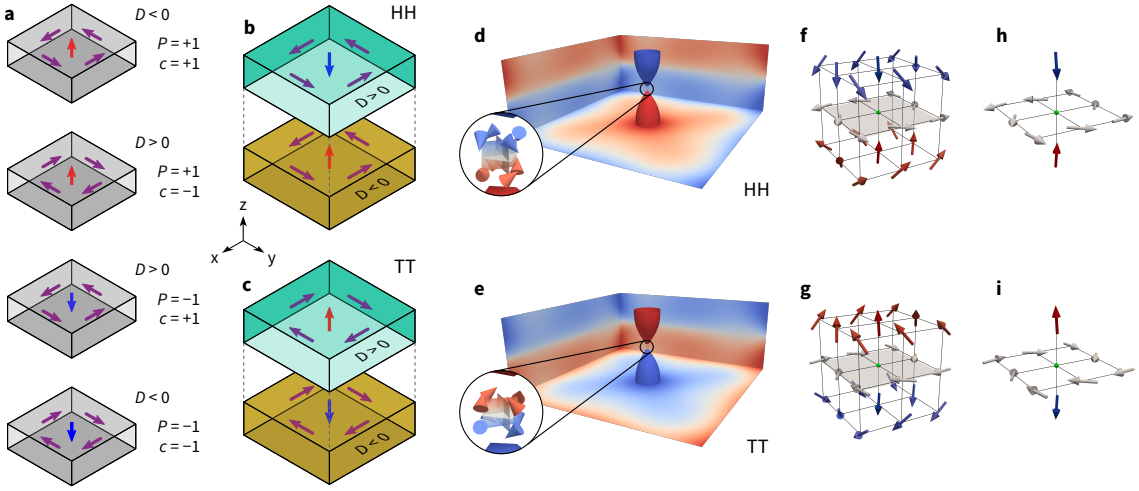

FIGURE 2.7: (a) In a single layer of magnetic material, four different vortices, with polarisation $P = \pm 1$ and circularity $c = \pm 1$, can form as a consequence of the competition between exchange energy and demagnetisation. Adding DMI couples circularity and polarisation. (b, c) By stacking two layers with opposite sign of the DM energy constant D, a Bloch point can be stabilised. The Bloch point can be of type head-to-head (b) or tail-to-tail (c). In the figure, the two layers are, for better clarity, separated in z direction as indicated by the grey dashed lines. (d, e) Simulation result for a single head-to-head (d) and tail-to-tail (e) Bloch point. The isosurfaces (of paraboloidal-like shape) near the centre show $m_z = \pm 0.9$, colour indicates the z component. They are convenient to locate the Bloch point that is situated between them. The insets show three isosurfaces for $m_x = 0$, $m_y = 0$, and $m_z = 0$, respectively. The Bloch point is located at the intersection of the three isosurfaces where the magnetisation vanishes. The cones in the insets indicate the magnetisation directions in the eight discretisation cells surrounding the Bloch point. The magnetisation around the Bloch point is show in more details in (f, h) for the HH configuration and in (g, i) for the TT configuration. See the main text for additional details. (Figure, including caption, taken from Lang et al., 2023a)

in Fig. 2.7b. When the magnetic moments point away from each other, we obtain a tail-to-tail Bloch point (TT), shown in Fig. 2.7c.

Figure 2.7d shows the magnetisation vector field for a single head-to-head Bloch point obtained from a micromagnetic simulation. Figure 2.7e shows the corresponding plot for a tail-to-tail Bloch point. Colour represents the m_z component of the magnetisation, the paraboloidal-like isosurfaces show $m_z = \pm 0.9$. The Bloch points are located between these structures, as indicated in the insets. In the simulations, the Bloch points form in the centre of eight discretisation cells. The insets show the magnetisation of these discretisation cells with cones. Additionally, they show three isosurfaces for $m_{x,y,z} = 0$. The Bloch points are located at the intersection of the three isosurfaces, where the magnetisation vanishes. Figure 2.7f and h and Fig. 2.7g and i show the magnetisation around the two Bloch points in more detail. Only the eight discretisation cells around the Bloch point are included. The magnetisation of the cells is interpolated onto the cell nodes. Here, we can clearly see that the moments above and below the Bloch points point in opposite direction. Furthermore, from the moments located in the xy plane around the Bloch point, we can see the circulating nature of the two Bloch points.

Similar to skyrmions and vortices, Bloch points can be classified using their topological charge. To compute the topological charge of a Bloch point, we can use a modified version of Eq. 2.39:

$$S_{\mathrm{BP}} = \frac{1}{4\pi\hbar} \int_{\mathcal{S}} \mathrm{d}\mathbf{s} \cdot \mathbf{B}^{\mathrm{e}}, \tag{2.47}$$

which reflects the 3D nature of the magnetisation configuration surrounding the Bloch point (Im et al., 2019). The integration in Eq. 2.47 is taken over an arbitrary closed surface $\mathcal{S}$ enclosing the Bloch point, $\mathbf{B}^{\mathrm{e}}$ is the emergent magnetic field, and $\mathrm{d}\mathbf{s}$ is a surface element. Bloch points have a topological charge $S_{\mathrm{BP}} = \pm 1$, depending on their type. Eq. 2.47 describes the flux of the emergent magnetic field through a closed surface surrounding the Bloch point, which is therefore quantised. We can re-write Eq. 2.47 using the divergence theorem and obtain:

$$S_{\mathrm{BP}} = \frac{1}{4\pi\hbar} \int \mathrm{d}V \, \mathrm{div}\, \mathbf{B}^{\mathrm{e}} = \pm 1, \tag{2.48}$$

where V is the volume enclosed by surface $\mathcal{S}$. We can see that Bloch points act as sources and sinks of the emergent magnetic field and can therefore be interpreted as emergent magnetic monopoles and antimonopoles (Milde et al., 2013).

As an example, we can compute the emergent magnetic field and the topological charge of a Bloch point using an analytic expression for the normalised magnetisation around the Bloch point. For a diverging Bloch point, the magnetisation is given as:

$$\mathbf{m}(\mathbf{r}) = \frac{\mathbf{r}}{r}. \tag{2.49}$$

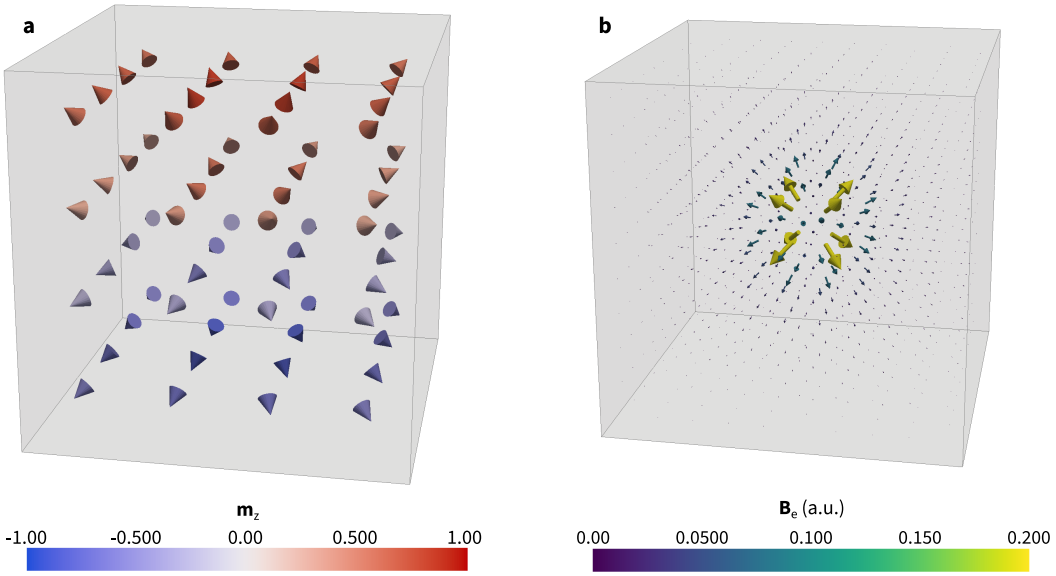

FIGURE 2.8: (a) Magnetisation around a diverging Bloch point; (b) resulting emergent magnetic field.

For the emergent magnetic field, we obtain:

$$\mathbf{B}^{\mathrm{e}}_{\mathrm{BP}} = \hbar \frac{\mathbf{r}}{r^3}. \tag{2.50}$$

We can then compute the divergence of the emergent magnetic field and find:

$$\operatorname{div} \mathbf{B}^{\mathrm{e}}_{\mathrm{BP}} = 4\pi\hbar\delta^{(3)}(\mathbf{r}). \tag{2.51}$$

Hence, for the topological charge we obtain:

$$S_{\mathrm{BP}} = \frac{1}{4\pi\hbar} \int \mathrm{d}V \operatorname{div} \mathbf{B}^{\mathrm{e}}_{\mathrm{BP}} = \int \mathrm{d}V \delta^{(3)}(\mathbf{r}) = 1. \tag{2.52}$$

Figure 2.8 shows numerical calculations for the diverging Bloch point defined in Eq. 2.49. We discretise the problem into $10 \times 10 \times 10$ discretisation cells and use a finite-difference approximation for the calculation of the derivatives. Figure 2.8a shows the magnetisation field around the Bloch point, which is located in the centre of the cube. In the figure, we have reduced the number of cones to $4 \times 4 \times 4$ to improve visibility. Figure 2.8b shows the emergent magnetic field, colour encodes the field strength. We can see the strong field localisation around the Bloch point, pointing radially away from the Bloch point. The diverging Bloch point acts as a source of the emergent magnetic field. Apart from the direct vicinity of the Bloch point, the magnetisation is almost collinear and hence only produces a much weaker emergent magnetic field.

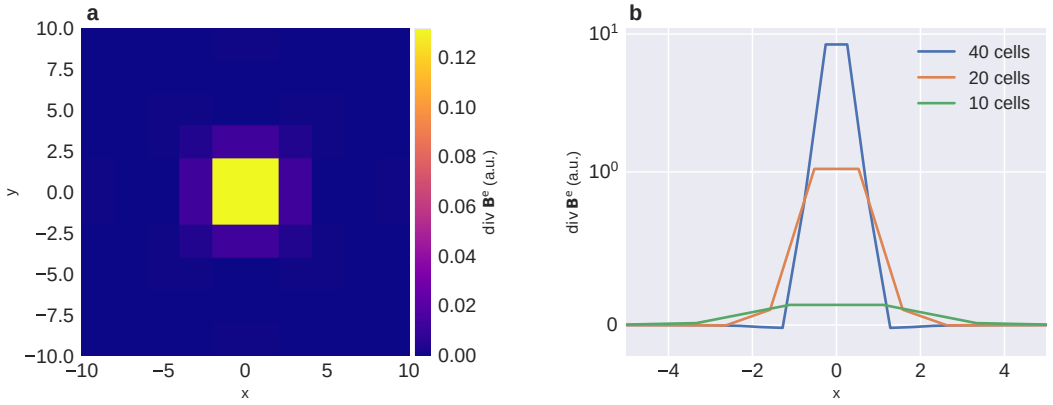

FIGURE 2.9: (a) Divergence of the emergent magnetic field in a layer of cells located above the Bloch point. (b) Influence of decreasing cell size on the numerical approximation of Eq. 2.51 in a line of cells located near the Bloch point.

Figure 2.9a shows $\operatorname{div} \mathbf{B}^{\mathrm{e}}_{\mathrm{BP}}$ on a cut-plane in xy for the discretisation cells located above the Bloch point. We can see a numerical approximation of the sharp δ peak obtained from Eq. 2.51. For the topological charge, we numerically obtain $S_{\mathrm{BP}} \approx 0.993$ which is in good agreement with the analytic value $S_{\mathrm{BP}} = 1$ despite the coarse discretisation used in this example. With decreasing discretisation cell size, the numerical accuracy increases: for $20 \times 20 \times 20$ discretisation cells, we obtain $S_{\mathrm{BP}} \approx 0.999$ and for $40 \times 40 \times 40$ discretisation cells, we obtain $S_{\mathrm{BP}} \approx 0.9996$. Figure 2.9b shows line cuts for $\operatorname{div} \mathbf{B}^{\mathrm{e}}_{\mathrm{BP}}$ for the different cell sizes. The cuts are always taken in the layer above the Bloch point. In the plot, we can see that $\operatorname{div} \mathbf{B}^{\mathrm{e}}_{\mathrm{BP}}$ converges towards a sharp peak with decreasing discretisation cell size.

In the micromagnetic simulations carried out in this work, we use $\operatorname{div} \mathbf{B}^{\mathrm{e}}_{\mathrm{BP}}$ to detect and locate Bloch points and determine their type (depending on the sign of S_{BP}). We numerically evaluate Eqs. 2.37 and 2.48 using a finite-differences approximation. For skyrmions, a numerically more accurate scheme (Berg & Lüscher, 1981; Kim & Mulkers, 2020) is commonly used to evaluate Eq. 2.39. This scheme could be directly generalised to three dimensions in order to compute the emergent magnetic field. In the present work, numerically evaluating the derivatives is sufficient as Bloch points have to have an integer-valued topological charge because of their point-like nature. Deviations from integer values are caused by the discretisation (see Sec. 4.5 for more details). The situation is different for skyrmions, where also non-integer valued skyrmions can exist (Beg et al., 2015).

Further difficulties in detecting Bloch points based on the emergent magnetic field occur in systems containing multiple Bloch points because of the fact that the sign of the topological charge of a Bloch point depends on its type. Hence, contributions from Bloch points of opposite type can cancel out. More details on how to deal with multiple Bloch points in a sample will be given in Sec. 4.5. The emergent magnetic field can also be used to locate Bloch points with sub cell-size accuracy by computing the centre of mass of $\operatorname{div} \mathbf{B}^{\mathrm{e}}$, see Sec. 5.2.2 for details.

Chapter 3

Computational tool Ubermag

Preface

Parts of the work on Ubermag have been published as Beg et al. (2022). The work on `mag2exp` is under review for publication as: S. J. R. Holt, M. Lang, J. C. Loudon, T. J. Hicken, D. Suess, D. Cortés-Ortuño, S. A. Pathak, M. Beg and H. Fangohr. "Virtual experiments in computational magnetism: `mag2exp`" (2023). An example of the usage of Ubermag for teaching, where I am one of the co-authors, is under review (Lonsky et al., 2023).

3.1 Introduction

We use and develop a Python package called Ubermag (Beg et al., 2022) for our simulations. Ubermag provides a high-level interface to existing micromagnetic simulation packages such as OOMMF (Donahue & Porter, 1999). The work on Ubermag started with its predecessor JOOMMF (Beg et al., 2017b), a package that was only interfacing OOMMF, as part of the OpenDreamKit project in 2015.[1] Later on, the ideas were generalised in the Ubermag package collection. Ubermag seemed well suited to support my studies. Therefore, I started using it and extended its functionality as required.

Ubermag is a human-centred research environment that improves the interface between the researcher and the numerical simulation and that can help make simulation-based micromagnetic research reproducible. Ubermag introduces a domain-specific language to describe micromagnetic problems in Python. This description is independent of the simulation tool, such as OOMMF, used to solve the problem. All tool-specific communication with the numerical backend, e.g. writing the `omf` and `mif` input files required for OOMMF, and parsing the output files generated by the numerical backend happens in the background without any interaction from the researcher.

[1] https://opendreamkit.org

This chapter is organised as follows. In Sec. 3.2 we give a high-level overview of a typical workflow when running (micromagnetic) simulations. We focus on the fundamental steps common to most simulation-based research and discuss typical difficulties when working with simulation software. We identify a number of possible improvements that motivate the design of Ubermag. In Sec. 3.3 we discuss the importance of reproducibility in science and common problems in achieving reproducibility in simulations in general. Afterwards, we introduce Ubermag by first discuss a small example of using Ubermag in a Jupyter Notebook in Sec. 3.4. In Sec. 3.5 we discuss the design ideas behind Ubermag and how it can help improve the scientist's work and reproducible research in more detail. We also give an overview of the individual subpackages and their interplay. In Sec. 3.6 the main extensions and modifications of the package during the time of my PhD are discussed. Furthermore, we briefly touch on some more general concepts and tools for maintaining a small open-source project like Ubermag. This section might be of use for similar open-source projects.

3.2 Computational workflow in micromagnetics

Computer simulations are a widely used tool to complement experiments and theoretical research. Carrying out micromagnetic simulations, like many simulations in other fields, commonly can be divided into five major steps, which are discussed below. In this discussion, we ignore the option to control simulations through a GUI, which some simulation packages provide. The steps are (Beg et al., 2022):

1. Decide on the physical problem to solve.
2. Express physics in a language understood by the simulation tool (typically some sort of configuration file).
3. Run the calculation: the simulation software writes data files—the simulation results.
4. Post-processing of the data files to analyse and visualise the simulation results.
5. Run multiple similar simulations to gain more insight, e.g. by studying the parameter space of a material parameter or the sample geometry. This implies repeating steps 2 to 4 in some sort of loop while varying one or more parameters.

In the micromagnetic context, several open-source packages with their main focus on step 3 are available, e.g. OOMMF (Donahue & Porter, 1999) and Mumax^3 (Vansteenkiste et al., 2014). In order to use these packages, we have to write configuration files. Each package defines its own syntax for these files. They are typically either written in a scripting language used in the simulation package, e.g. `tcl`-based input files for OOMMF, or have a custom syntax inspired by the language used to write the simulation software, e.g. `go`-inspired input files for Mumax^3.

For post-processing, the packages commonly provide a limited set of additional functionality, e.g. through a number of (small) additional utility programmes.

The packages' strong focus on numerically solving the problem in combination with the way they are used implies several difficulties that can together result in a steep learning curve. First, the user generally has to learn either a new scripting language, which might not be widely used (any more), or the tool-specific syntax to write input files. In both cases it can be potentially difficult to find enough training resources and documentation. Furthermore, writing input files generally is a mixture of two conceptionally independent steps: (i) defining the physics of the problem (such as the energy and dynamics equation) in a machine-readable format and (ii) defining numerically required "details" such as how to discretise the problem. Ideally, the two steps would be separated: step (i) would be done in a more abstract format that more closely follows the analytic description of the problem. Afterwards, the user would define numerical details in step (ii) and the software would automatically translate the high-level problem description taking these details into account.

Further difficulties arise during the data analysis (step 4). Data files are often written in custom formats that are not used outside the micromagnetics context. This does not cause any problems as long as all post-processing can be done using the provided auxiliary tools. However, research, due to its very nature, often requires the researcher to come up with new analysis methods. Not only does this imply knowing a (second) language suitable for data analysis and visualisation, the researcher also has to understand the structure of the data files and write custom code to parse the data files and convert them into data structures suitable for further analysis—a time-consuming and potentially error-prone additional task.

Step 5, running multiple similar simulations, is generally not directly supported by the simulation packages. It requires the researcher to write additional code to control the individual simulations, e.g. by automatically creating suitable input files for each configuration. Again, this requires knowledge of a separate language. Furthermore, prior experience with some sort of template mechanism is typically required to generate the individual input files.

The aim of Ubermag is to simplify steps 2, 4, and 5. For that purpose, Ubermag introduces an abstraction layer, written in Python, sitting above (German "über") existing micromagnetic simulation packages. This additional layer introduces a number of simplifications and circumvents the problems outlined above. Running micromagnetic simulations through Ubermag only requires Python knowledge, one of the most popular and widely used programming languages. Python is deemed to be an easy-to-learn language (Bogdanchikov et al., 2013) and extensive documentation and plenty of tutorials and video courses can be found online. Many researchers even have some previous programming experience with Python. The researcher can use the same language to describe the problem (step 2), for data analysis (step 4), and to control multiple simulations (step 5). To simplify step 2, Ubermag introduces a machine-readable high-level syntax to describe the physics of the problem and—separately—numerical details such as discretisation. Ubermag then converts these into configuration files required by

the simulation packages. There are similar projects with the goal to simplify using simulation software in other fields, e.g. the Atomic Simulation Environment (ASE) (Larsen et al., 2017) and pyiron (Janssen et al., 2019).

3.3 Reproducibility

Confirmation and reproduction of scientific results is a key-element to make research trustworthy. The most powerful way to confirm scientific claims is replicability, i.e. a different group or person performs a similar study using a different method and obtains the same scientific result. However, replication is not always possible, e.g. due to the required resources (Peng, 2011). An alternative is reproducing the results using the same method. The repeating study may be conducted by the same researcher or a different person or group. In this work, we combine both options under the term reproducibility and note that the term is not used consistently across literature. Reproducibility is not only important to confirm scientific claims. It is also a requirement to conduct further research based on previous findings. Lastly, it can greatly simplify starting to work in a new field, e.g. as a PhD student.

A recent survey shows that many research results in various scientific fields are not reproducible (Baker, 2016): in the survey, close to 70% of the participants in the field of physics and engineering reported that they failed reproducing someone else's results and over 50% failed reproducing their own results. Many factors contribute to the lack of reproducibility. Two of the most commonly perceived problems are the "pressure to publish and selective reporting" (Baker, 2016). Making research reproducible requires additional effort and time from the researcher and is generally not reflected in the metrics used to judge scientific reputation.

Reproducible research is increasingly gaining attention. Several journals by now require data and protocols to be available and reserve the right to tag publications that are not reproducible.[2] Many works in various fields of research aim at making research more reproducible, e.g. by simplifying the process of recording required information and establishing new standards for data exchange. Examples can be found in earth observation (Giuliani et al., 2019), molecular dynamics simulations (Bonomi et al., 2019), neuroscience (Mulugeta et al., 2018), multi-physics simulations (Tylissanakis & Cotronis, 2009), and computational drug discovery (Schaduangrat et al., 2020), among others.

Here, we are particularly interested in computer simulations. Many difficulties in making numerical simulations reproducible can arise (Peng, 2011; Beg et al., 2021): One set of problems is related to a lack of reported details when publishing results. Commonly missing information are a full list of simulation parameters, a detailed simulation protocol, or exact versions of all software packages used (including all libraries or indirect dependencies). One reason for this is that reporting such simulation details is not enforced by current publication standards.

[2] https://www.nature.com/nature-portfolio/editorial-policies/reporting-standards, accessed on July 27, 2023

Sometimes unawareness of the existence or importance of certain parameters (such as hard-coded default values of the simulation software) can also contribute. The problem of missing information on the used software versions is enhanced by a lack of support for recording such information in many of the tools used to write and compile research software. Further software-related difficulties can arise even if versions are recorded. Old versions might not be available any more, in particular for commercially available, closed-source software. Old versions of open-source software, although probably more easily available, might rely on old versions of system libraries, which in turn can make it (nearly) impossible to re-compile the software on more modern operating systems. A third set of problems can arise from inevitable numerical deviations as a consequence of floating-point inaccuracies and non-deterministic execution order of parallelised code (Diethelm, 2012). This is a fundamental property of computer simulations and can only be dealt with by raising awareness for the phenomenon and providing proper training for end-users of simulation code.

The difficulties of re-creating the same software environment can, at least for open-source software, for instance, be addressed by archiving and publishing containers containing the full software stack. Virtualisation in containers such as Docker or Apptainer ensures independence of the host's (system) libraries, whereby it simplifies the use of software that relies on old versions of (system) libraries, which may be incompatible with other software used on the same system.

One tool that can help to record a detailed simulation protocol and simulation parameters are Jupyter Notebooks (Kluyver et al., 2016). In recent years, Jupyter notebooks have evolved into a tool that is widely used in computational research, data science, and many other communities. The Jupyter Notebook can combine code, data, visualisation, and textual explanations including equations in a single document. These features allow for expressing computational narratives in Jupyter Notebooks (Granger & Pérez, 2021). By conducting the whole simulation in a single notebook, the full simulation input, the order of subsequent simulations, and the obtained results can be recorded (Beg et al., 2021). The resulting notebooks can easily be shared or exported to common formats such as static HTML or PDF. Services like Binder[3] allow users to re-execute notebooks in the cloud using a software environment defined by the notebook creator and hence have the potential to be used to reproduce central figures of a publication. Binder does not require any software installed locally, it fully runs inside a web browser, and executes the notebook inside a container in the cloud. Standard file formats of the relevant programming ecosystems are used to define the required software environment of that container. We note that computational resources on Binder are limited. Hence, it is not suitable for computationally demanding simulations but may still be used to analyse pre-computed datasets.

As a consequence of their great flexibility, Jupyter Notebooks are not by default reproducible: code cells can be executed in arbitrary order, code cells can be removed or modified after execution, and new cells can be added later on. All these changes potentially break a top-down

[3] https://mybinder.org/

re-execution of the notebook, rendering the notebook not reproducible (Pimentel et al., 2021). Furthermore, Jupyter Notebooks do not record software versions used when executing the notebook. This has to be done separately, e.g. using the standards the Binder project relies on. To circumvent the problems of execution order or modifications post execution, tools have been developed to identify and warn about potential problems during notebook creation (Pimentel et al., 2021) or to try reconstructing execution order of an existing notebook (Wang et al., 2021). Rule et al. (2018) have formulated a set of rules to follow to make research in Jupyter Notebooks reproducible.

3.4 Example: vortex dynamics

In this section, we demonstrate how to use Ubermag by discussing a simple example: the dynamics of a magnetic vortex in a ferromagnetic permalloy nanostructure. Ubermag is a collection of several Python packages, that each address a specific sub-part of running a micromagnetic simulation and can be related to the individual steps outlined in the Sec. 3.2 (see Sec. 3.5 for a detailed discussion of all sub-packages).

In this introductory example, we only cover three packages. We use `micromagneticmodel` to define the physics of our system, i.e. the energy and the dynamics equation. The simulated "sample", i.e. the shape and discretisation of the simulated region and the saturation magnetisation, is defined using `discretisedfield`. We use OOMMF as the backend to solve the problem numerically. To communicate with OOMMF we use `oommfc`.

The use of Python as a language for the Ubermag packages makes it possible to control the simulation from a Jupyter Notebook. Ubermag controls the external micromagnetic solver used in the background and transfers the results back to the notebook. This allows plotting and further analysis in the same notebook. Figures 3.1 and 3.2 show the notebook for the vortex-dynamics example. The notebook is split into two figures because it does not fit onto a single page. We explain the workflow for this simulation in the remainder of this section.

First, we import the required packages in cell 1 (Fig. 3.1). Additionally, we change the default figure format to svg to improve the figure rendering inside the notebook.

The whole simulation information is stored inside a so-called `system` object, defined in cell 2. We have to provide a system name, which affects where the simulation will be stored on disk, and which can be used to later access the simulation results. We define the energy equation and the dynamics equation in cells 3 and 4, respectively. In the notebook, both can be rendered using LaTeX after they are defined. In this example, we include exchange energy with $A = 13\,\mathrm{pA/m}$ and demagnetisation energy, material parameters are based on permalloy. The magnetisation dynamics is governed by the Landau-Lifshitz-Gilbert equation and consists of a precession term with the reduced gyromagnetic ratio $\gamma_0 = 2.211 \times 10^5\,\mathrm{m/(As)}$, pre-defined in

[1]:
```
%config InlineBackend.figure_formats = ['svg']
import discretisedfield as df
import micromagneticmodel as mm
import oommfc as oc
```

[2]:
```
system = mm.System(name='vortex_dynamics')
```

[3]:
```
system.energy = mm.Exchange(A=13e-12) + mm.Demag()
system.energy
```

[3]: $-A\mathbf{m}\cdot\nabla^2\mathbf{m} - \frac{1}{2}\mu_0 M_\mathrm{s}\mathbf{m}\cdot\mathbf{H}_\mathrm{d}$

[4]:
```
system.dynamics = mm.Precession(gamma0=mm.consts.gamma0) + mm.Damping(alpha=0.2)
system.dynamics
```

[4]: $-\frac{\gamma_0}{1+\alpha^2}\mathbf{m}\times\mathbf{H}_\mathrm{eff} - \frac{\gamma_0\alpha}{1+\alpha^2}\mathbf{m}\times(\mathbf{m}\times\mathbf{H}_\mathrm{eff})$

[5]:
```
region = df.Region(p1=(-50e-9, -50e-9, -2.5e-9), p2=(50e-9, 50e-9, 2.5e-9))
mesh = df.Mesh(region=region, cell=(5e-9, 5e-9, 5e-9))
mesh.mpl()
```

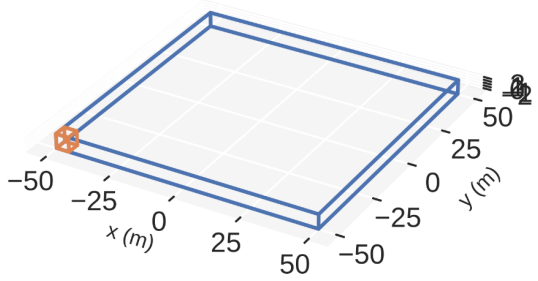

[6]:
```
def init_m(p):
    return (-1e9*p[1], 1e9*p[0], 1)
system.m = df.Field(mesh, nvdim=3, value=init_m, norm=8e5)
```

[7]:
```
md = oc.MinDriver()
md.drive(system)
```

```
Running OOMMF (ExeOOMMFRunner)[2023/05/09 11:43]... (0.4 s)
```

[8]:
```
system.m.orientation.sel('z').mpl(scalar_kw={'clim': (0, 1)})
```

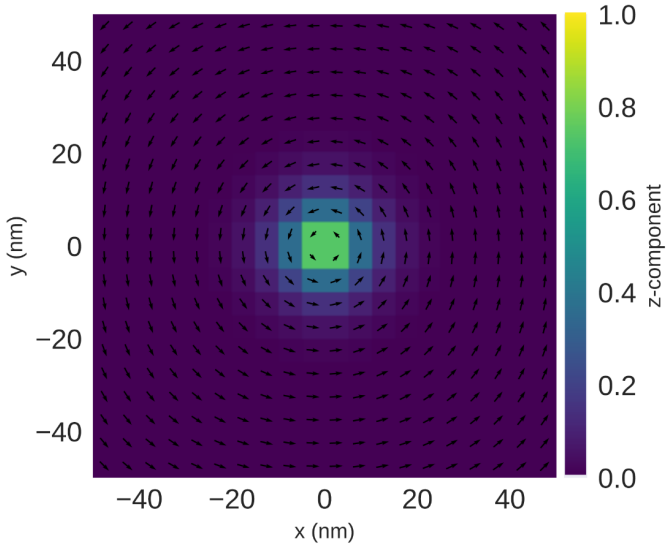

FIGURE 3.1: Part 1 of the example notebook to demonstrate the use of Ubermag. This part demonstrates the system set-up and the initial energy minimisation. The overlapping labels in cell 5 are a shortcoming of the simplified visualisation method, see main text for details.

```
[9]: system.energy += mm.Zeeman(H=(1e4, 0, 0))
     md.drive(system)
```

```
Running OOMMF (ExeOOMMFRunner)[2023/05/09 11:43]... (0.4 s)
```

```
[10]: system.m.orientation.sel('z').mpl(scalar_kw={'clim': (0, 1)})
```

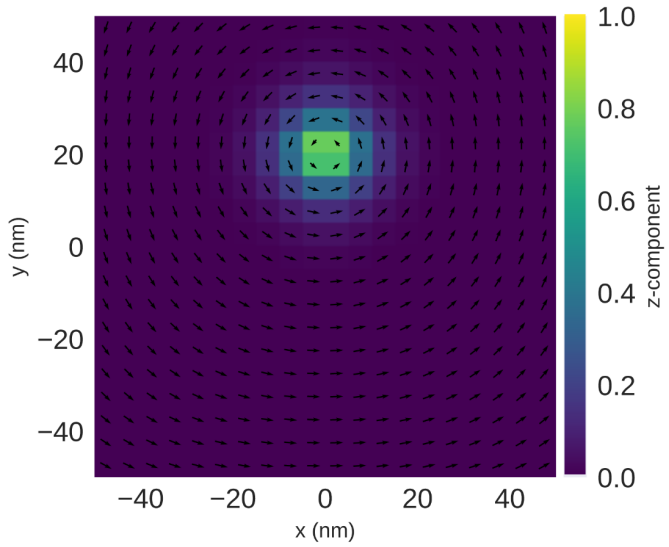


```
[11]: system.energy.zeeman.H = (0, 0, 0)
      td = oc.TimeDriver()
      td.drive(system, t=5e-9, n=200)
```

```
Running OOMMF (ExeOOMMFRunner)[2023/05/09 11:43]... (3.4 s)
```

```
[12]: system.table.mpl(y=['mx', 'my'])
```

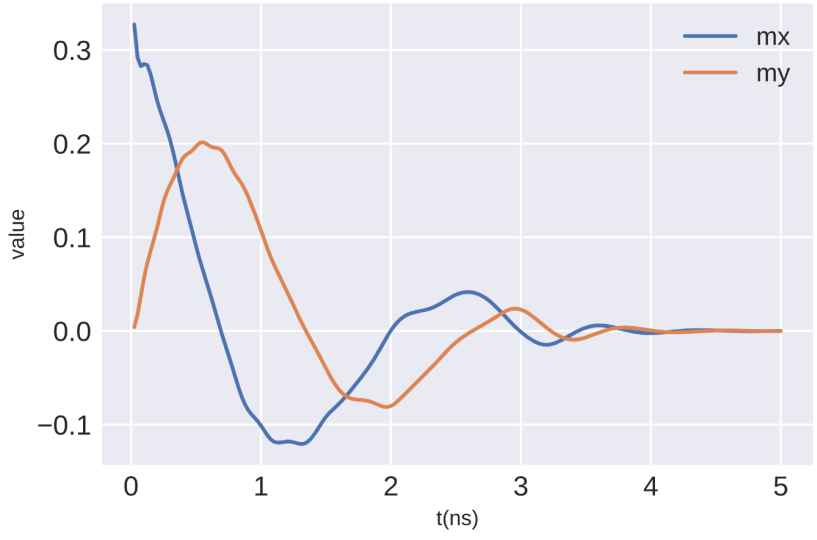

FIGURE 3.2: Part 2 of the example notebook to demonstrate the use of Ubermag. This part demonstrates running additional simulations after the first energy minimisation, changing terms in the energy equation, and analysing time-resolved data.

micromagneticmodel, and the Gilbert damping term with $\alpha = 0.2$. The damping constant is set to an exceptionally large value in order to simplify the dynamics in this example.

The second part of the initialisation is defining the "sample". This step comprises defining the size of the simulation region, defining a mesh to discretise this region, and defining the initial configuration and the saturation magnetisation of the sample on this mesh (stored in system.m). In cell 5, we define the shape of the sample. We simulate a cuboidal sample with edge lengths $l_x = l_y = 100\,\text{nm}$ and thickness $l_z = 5\,\text{nm}$, called region in the notebook. This region is then divided into cells with 5 nm edge length to obtain a finite-difference mesh. We can plot the region and one cell to visually inspect the mesh and cell size. In the output in cell 5 (generated from mesh.mpl()) we can see the region in blue and the size of one discretisation cell in orange. We note that while this method is very convenient for quick checks it has some limitations. In particular, the automatic aspect ratio adjustment does not work well together with the automatic axis labeling. This leads to a blob of overlapping tick labels for the z axis in cell 5. More custom code would be required to resolve this problem when a high-quality plot is required.

In cell 6, we define the initial magnetisation. We start from a vortex configuration by initialising the magnetisation at each point $\mathbf{r} = (x, y, z)$ in the sample with:

$$\mathbf{m}(\mathbf{r}) = (m_x, m_y, m_z) \propto (-cy, cx, 1), \tag{3.1}$$

with $c = 10^9\,\text{m}^{-1}$ and a saturation magnetisation $M_\text{s} = 8 \times 10^5\,\text{A/m}$. The z component is chosen to be positive to control the polarisation of the final vortex, its exact value has no effect. We can express the initial state by defining a Python function (init_m), which will be called for each cell centre point p (the position $\mathbf{r}$ of that cell) in the mesh. By passing a value to the optional argument norm, Ubermag automatically normalises the magnetisation to M_s when initialising the Field object system.m.

We now minimise the energy of the initial configuration. In cell 7, we create a MinDriver object to communicate with OOMMF. To minimise the energy of the initial configuration, we can use the drive method of this object. This method automatically generates the required input for OOMMF based on our definition in the cells above and calls OOMMF in the background. When the simulation is finished, oommfc will automatically read the results and update the system object. In the notebook, we can see some status information, such as which calculator was used and the calculator's run time.

In cell 8, we plot the new magnetisation configuration obtained from the simulation. In this example, we create a static plot showing the magnetisation in one cut plane. We could also create interactive plots (see Fig. 3.5 for an example) or 3D visualisations. We plot the normalised magnetisation in the xy plane centred in the z direction. The arrows show the in-plane $\mathbf{m}_{xy}$ components, and the colour plot shows the out-of-plane m_z component. We can see that the initial magnetisation has relaxed into a vortex configuration.

Now, we can run the next simulation starting from this vortex state. This is shown in the second half of the notebook in Fig. 3.2. In this example, we run two more simulations. First, we apply an external Zeeman field in the $+x$ direction and again minimise the system's energy in cell 9. Cell 10 shows the configuration obtained from this energy minimisation. We can see that the vortex is shifted in the $+y$ direction. The shift can easily be understood: the shift of the vortex core results in a larger part of the magnetisation pointing in the $+x$ direction, parallel to the external field, minimising the Zeeman energy. However, the external field is not strong enough to fully saturate the sample and push the vortex out of the system.

In the final step, cell 11, the Zeeman field is removed and the time evolution of the free system is simulated for $t = 5$ ns. For this simulation, we request that OOMMF saves the magnetisation and spatially averaged data such as the total energy at $n = 200$ equidistant time steps.

In cell 12, we analyse the results of the last simulation. The `system` object provides access to spatially averaged simulation results of the last simulation, e.g. averaged magnetisation along different spatial directions and total energy. Here, we plot the averaged m_x and m_y components of the normalised magnetisation. We can see that initially (after applying the external magnetic field) $m_x > 0$, i.e. the vortex is shifted in $+y$ direction and a larger part of the magnetisation points in $+x$ direction. Furthermore, $m_y = 0$, i.e. the vortex is centred in x direction. We have already seen this configuration in the plot in cell 10. As a function of time, we can see a damped oscillation of the m_x component back to $m_x = 0$, i.e. the vortex being centred in y direction. Additionally, we can also see a damped oscillation of the m_y component with a $\pi/2$ phase shift compared to the m_x component. Overall, this describes a spiralling movement of the vortex, initially displaced in $+y$ direction, back to the sample centre. The final configuration is the same as initial configuration shown in Fig 3.1, cell 8.

A slightly modified version of the notebook discussed in this section is available on the Ubermag website.[4] The notebook on the website can be executed and modified interactively inside a browser via the Binder service.

3.5 Ubermag design

In the previous section, we have discussed some of the ideas behind Ubermag by looking at an example notebook that outlines a typical workflow for interactive exploration. In this section, we will discuss the design of Ubermag on a higher level.

Ubermag consists of eight user-facing subpackages and additional internal utilities. We have already seen a few of the most commonly used packages in the example discussed in the previous section. Figure 3.3 gives an overview over all user-facing subpackages and groups them according to their use case, hence `discretisedfield` appears twice. The `ubermag` meta-package, primarily used to simplify the installation process and guarantee matching versions

[4] https://ubermag.github.io/demo.html

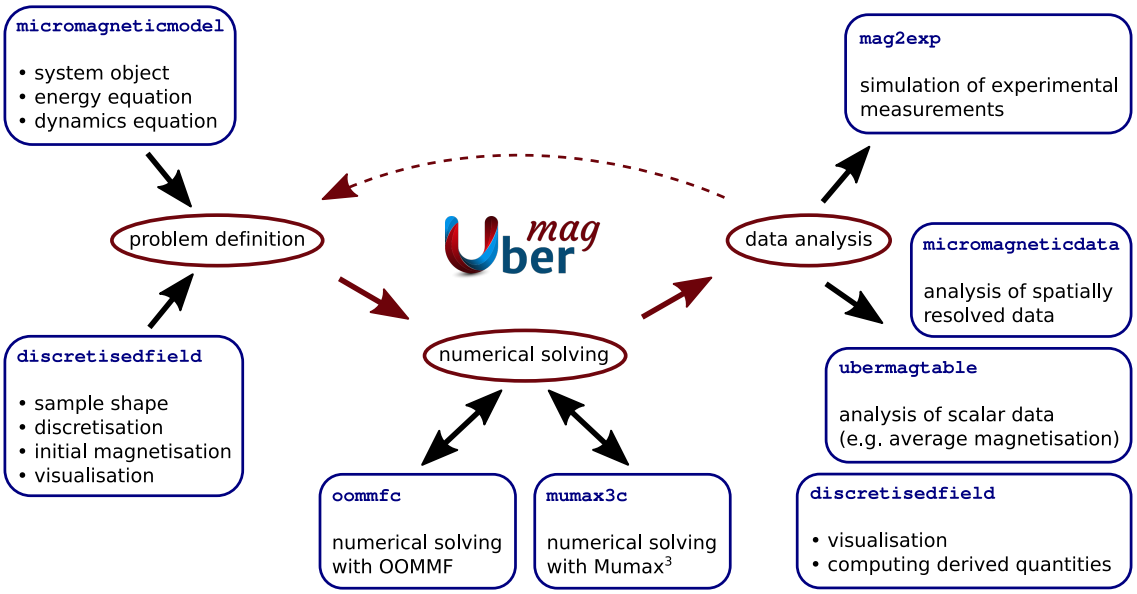

FIGURE 3.3: Overview of the packages in Ubermag.

of the individual subpackages, is not shown. The individual groups can be related to the typical steps of a simulation outlined in Sec. 3.2. For easier reference we briefly repeat them here: (1) select physical problem, (2) express physics in a machine-readable format, (3) run the simulation, (4) analyse data, and (5) loop over steps 2–4. In the following discussion, we ignore the more general step 1.

The first part (step 2) is defining the problem in a machine-readable format. In Ubermag the whole simulation is controlled using the so-called `system` object, which we have to define and populate. This consists of two sub-steps: `micromagneticmodel` is used to define the physics of the system, i.e. the energy equation and the dynamics equation; `discretisedfield` is used to define the sample (shape and saturation magnetisation) in a finite-difference form suitable for numerical treatment.

The second part (step 3) is numerically solving the problem. Ubermag converts the `system` object into input files understood by the micromagnetic calculator used in the background. This is done using the *calculator* packages `oommfc` or `mumax3c`. These calculator packages also handle communication with the calculators: they trigger the simulation after writing the required input files and update the `system` object after the simulation has finished. Multiple simulations (called drives) can be performed in sequence using the same `system` object (potentially using different calculators for the individual simulations). Doing this inside a single notebook (or script) allows us to record the full simulation workflow and contributes to simplifying step 5. We will discuss the advantages in more detail later on.

The third part (step 4) is analysing and visualising the simulation results. Ubermag provides two dedicated packages for this. `ubermagtable` can read tabular data files written by the calculators and provide them in a standard format, a `pandas.DataFrame`. These tables

contain data such as the averaged magnetisation or total energy for each simulation step. The `micromagneticdata` package provides access to (time-resolved) spatially resolved magnetisation files written by the calculator. The user can specify some simulation metadata, which determine the location on disk, to load data of a specific simulation and then gain convenient access to all simulation results. Individual magnetisation snapshots can be loaded and are returned as `discretisedfield.Field` objects. For post-processing and data analysis, `discretisedfield` provides a number of different plotting methods for 2D and 3D visualisation, several pre-defined functions to compute commonly-used quantities such as topological charge, and support for mathematical operations, ranging from simple operations such as addition to numeric derivation or integration and Fourier transformation, to compute more specialised quantities. It is also easily possible to integrate external Python packages, e.g. for image processing or machine learning, into the analysis process. Combined functionality from `micromagneticdata` and `discretisedfield` allows for analysing time-resolved simulations in interactive plots (using a slider for the time axis) inside Jupyter Notebooks with a single line of Python code. `micromagneticdata` also provides direct access to the associated tabular results provided by the `micromagnetictable` package. Going beyond pure data analysis, the package `mag2exp` can use simulation results (the magnetisation configuration) to simulate the outcome of a range of experimental techniques, such as Lorentz transmission electron microscopy, torque magnetometry, or small-angle neutron scattering, among others. Together, these packages provide flexible and powerful post-processing capabilities that are easily adaptable and extensible and do not restrict researchers to a limited set of functionality.

In a typical study, we would cycle between the individual steps multiple times (step 5). We start with a problem definition, solve the problem numerically, and analyse the results. Then we go back to the problem definition and modify one parameter (e.g. the sample shape or the strength of an external field), re-run the simulation, and analyse the new data. Ubermag significantly simplifies this process. First, the whole simulation is controlled using the `system` object. Inside a Jupyter Notebook, we can naturally perform our first simulation and analyse the results, then modify the `system` object, and perform the next simulation. We have already seen this in the example in Sec. 3.4, where we first minimise the energy of our sample (Fig. 3.1, cells 2–8), subsequently add an external field and minimise the energy (Fig. 3.2, cell 9), and in the final step remove the external field and simulate a time evolution (Fig. 3.2, cell 11). Second, defining the whole simulation inside Python makes it straightforward to introduce additional loops to control parameters of the simulation. To make this clearer, we discuss two different examples. (i) We can use a loop to e.g. vary the geometry of our sample, create a `system` object for each geometry, and run the same simulation steps for all geometries. (ii) We can initialise the `system` once and use it as a starting point for multiple independent subsequent simulations, where we e.g. use a loop to vary the strength of an applied field and simulate the time evolution for each field strength starting from the same initial configuration. For more comprehensive studies, both ideas can be combined and extended arbitrarily.

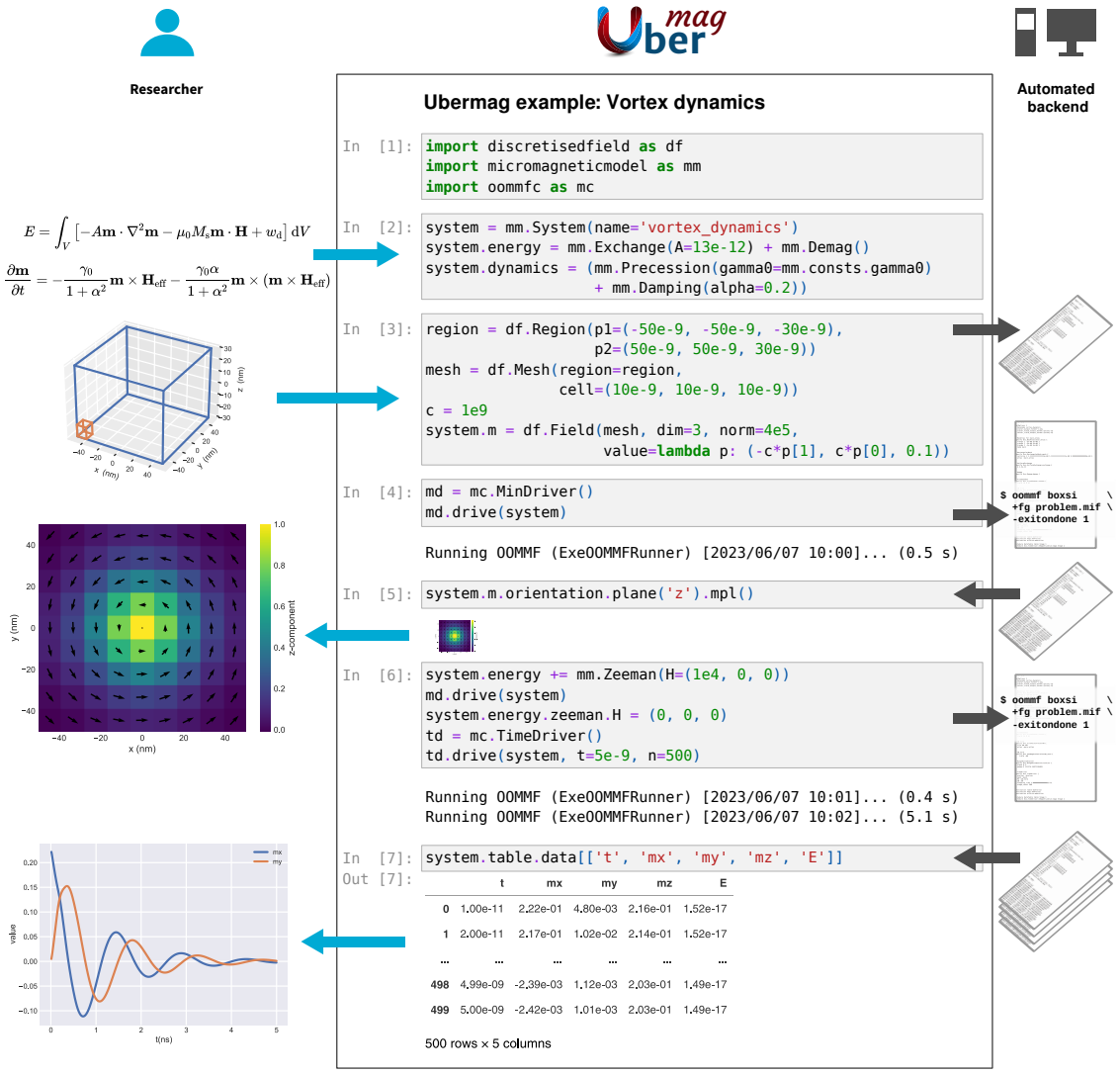

FIGURE 3.4: A typical simulation workflow and the abstractions introduced by Ubermag. The whole simulation can be driven from a single Jupyter Notebook as shown in the central column. The researcher defines the physical problem (cell 2) and the system to study (cell 3). Both can be visualised directly inside the notebook as indicated on the left-hand side. Ubermag internally communicates with a low-level simulation tool (cells 3, 4 and 6) shown as the autonomous backend in the right column, and returns the simulation results in a high-level format (cells 5 and 7). Plots of the simulation results and further data analysis are part of the notebook.

To better demonstrate how the high-level interface introduced by Ubermag, which separates researcher and low-level calculators, relates to the use inside a Jupyter Notebook, we repeat the notebook discussed in Sec. 3.4. Figure 3.4 shows a slightly shortened and modified version of the notebook: in order to highlight the key ideas of Ubermag, the notebook shown in this figure has been manually modified and in particular the plots have been rearranged. The separation of the researcher and the numerical backend through Ubermag is visualised with a three-column layout. The researcher (left) would define the physics using equations and can best understand the numerical results using plots. The numerical backend (right) needs input files in a specific format and returns text or binary files with simulation results. Their specific format is generally not important to the researcher (hence not readable in the figure). Ubermag (middle) helps to mediate between the two by introducing a comparatively simple Python-based intermediate layer that can be used inside a Jupyter Notebook or Python script.

Ubermag as a human-centred framework for micromagnetic simulations can help make simulation studies more reproducible. It is designed to be used inside Jupyter Notebooks, whereby the whole simulation workflow is recorded. The domain-specific language introduced primarily in `micromagneticmodel`, which is both human and machine-readable, can serve as a self-documenting description of the simulation and does not require calculator-specific knowledge. Additional textual explanations can be added directly in the notebook to complement and explain code and figures. The Python ecosystem provides tools to record all software used to perform a specific study (excluding some of the external calculators used in the background). When publishing their work, researchers can create an accompanying Binder-enabled GitHub repository that contains notebooks to repeat all simulations and re-create central figures of the publication. A separate DOI can be assigned to this GitHub repository via research repositories such as Zenodo. To give a concrete example, we refer to our study of multiple Bloch points (Lang et al., 2023a), discussed in the next chapter, that is accompanied by such a repository (Lang et al., 2022).

3.6 Open-source project Ubermag

A part of my time as a PhD student was dedicated to maintaining and extending Ubermag. I started contributing to Ubermag during my first year as a PhD student and have been the lead developer of Ubermag since mid 2021. This section gives a short overview over notable extensions in Ubermag during this time period. Furthermore, we briefly describe useful tools and best practices for maintaining a small open-source project. This might be a useful reference for other people working on similar projects.

The main activities in Ubermag during the time of my PhD were improving data analysis and plotting, a number of comparatively small but very effective performance improvements, adding support for Mumax[3] as a second backend in addition to OOMMF, and integrating a new package to simulate magnetic experiments.

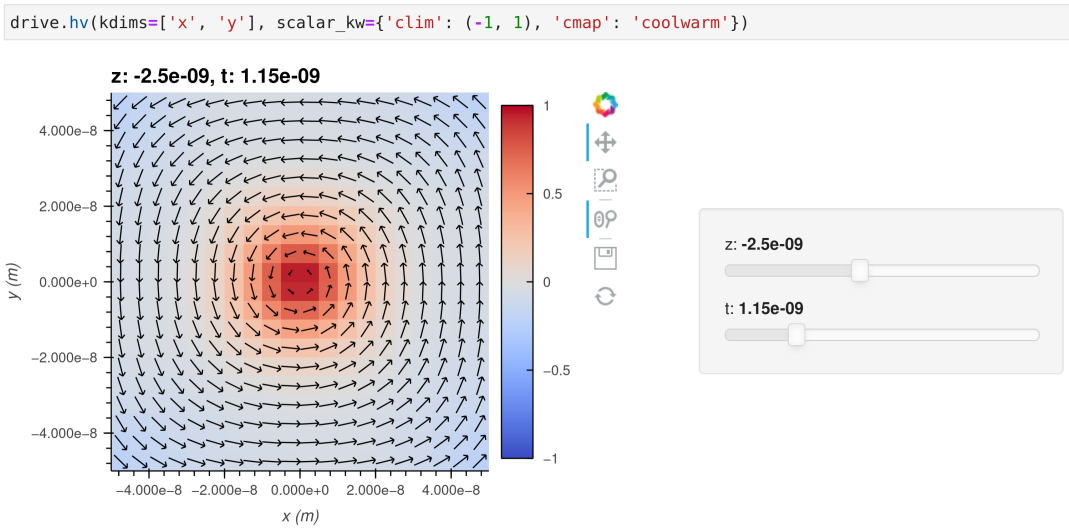

FIGURE 3.5: Interactive visualisation in a Jupyter Notebook.

The central improvement for data analysis was adding new interactive plotting functionality based on `holoviews` (Rudiger et al., 2023). The use of a JavaScript-based plotting library (`bokeh`) via the high-level interface `holoviews` makes it possible to create responsive plots. The new plotting can be used inside Jupyter Notebooks and allows plotting two-dimensional slices of higher-dimensional data (e.g. a single magnetisation field with three spatial coordinates or a time series of magnetisation fields with three spatial coordinates and one time coordinate) by automatically creating sliders for all dimensions not shown along the plot axes.

An example of such an interactive plot is shown in Fig. 3.5, where we plot a vortex similar to the one discussed in the example in Sec. 3.4. Different from the discussion in Sec. 3.4, we here use a sample with multiple layers in z direction in order to better show the interactive controls provided by `holoviews`. We plot one step of a time evolution, similar to the simulation in cell 11 in the notebook shown in Fig. 3.2. The plot shows the xy plane, a slider is automatically generated for the z direction. In the example, we look at $z = -2.5\,\text{nm}$. A second slider is provided for the time axis, in the example we can see the step $t = 1.15\,\text{ns}$.

The new plotting functionality was added to `discretisedfield` and `micromagneticdata` and a thin additional wrapper layer provides a simple interface that only requires very few lines of code to create fully interactive plots. The wrapper layer helps provide a consistent user interface for all plotting functionality in Ubermag, independent of the underlying library. The code is structured in a way that facilitates plotting long time evolutions where the total simulation data would exceed the main memory of the computer. The new interactive plotting functionality simplifies analysing and understanding magnetisation configurations. Furthermore, it can significantly speed up visually inspecting long time evolutions. It proved to be very effective for my simulations.

Ubermag as an additional layer above other packages such as OOMMF introduced some computational overhead. I could reduce this overhead by re-writing some performance-critical

parts in `discretisedfield` that are related to the field initialisation and saving fields to disk, in order to use them as input for OOMMF, as well as reading OOMMF output. After this re-write, the overhead introduced by Ubermag is now negligible, independent of the number of simulation cells. Previously, running large simulations did come with a disproportionately large overhead.

In a joint work with two postdoctoral researchers in our group, Samuel Holt and Swapneel Amit Pathak, we have added support for Mumax^3 (Vansteenkiste et al., 2014) as a second backend in addition to OOMMF. While fully implementing support for Mumax^3, I have also improved and generalised the abstractions in `micromagneticmodel` that describe the high-level user interface of an external calculator inside Ubermag. This will simplify adding additional external calculators in the future.

The last major improvement was adding the new package `mag2exp`, which can simulate experimental measurement techniques commonly utilised to study magnetism. The initial version of the code was written by Samuel Holt during his PhD (Holt, 2021). Samuel Holt and I integrated the code into the Ubermag package collection, making use of existing functionality of the other packages such as `discretisedfield` to simplify the code and avoid duplication. Furthermore, we re-designed the user interface to have a concise and consistent interface that integrates well with the other packages in Ubermag. My primary contribution was the software development side of `mag2exp`, i.e. re-designing the user interface, overall code structure, ensuring re-use of existing functionality where possible, and packaging the code. I was not involved in developing any of the measurement-related functionality.

In the remainder of this section we outline infrastructure that can help maintain a small open-source project such as Ubermag. The two most important aspects for development are version control and automated testing (generally referred to as continuous integration). We use `git` for version control and publicly host the code on GitHub.[5] All sub-packages have comprehensive test suites that are used for continuous integration, i.e. all changes in the code are tested to avoid regressions and incompatibilities in the code base. GitHub provides infrastructure for continuous integration (called GitHub Actions), which facilitates automatically testing all commits.

We use pre-commit hooks for automatic formatting and style checking. This ensures a consistent code style independent of the programmer, which significantly simplifies browsing through larger parts of the code base. To automate repetitive tasks, such as making releases, we use command line scripts that are based on a Python library called `invoke`. The use of Python for these tasks comes with two benefits. First, it is the same language that is also used for Ubermag, hence developers are familiar with it. Second, the Python-based approach allows us to have platform-independent automation scripts that can be used on all operating systems. We deliberately chose not to use GitHub Actions for these tasks to avoid vendor lock-in.

[5] https://github.com/ubermag

The choice of Python as a language to implement Ubermag comes with a several of benefits. Python is very widely used for all sorts of data-analysis, and the community therefore provides numerous powerful packages. By directly exposing the data from micromagnetic simulations to this ecosystem, it is straight-forward to make use of libraries such as NumPy (Harris et al., 2020), SciPy (Virtanen et al., 2020), Xarray (Hoyer & Hamman, 2017), pandas (McKinney, 2010), Matplotlib (Hunter, 2007), HoloViews (Rudiger et al., 2023), or PyVista (Sullivan & Kaszynski, 2019) for data analysis and visualisation. We use all of these packages for our work, many are directly integrated into Ubermag. Furthermore, Ubermag integrates well into the Jupyter ecosystem (Kluyver et al., 2016; Granger & Pérez, 2021), which simplifies research and can help to improve reproducibility, as explained in the previous section.

We provide packages for the two main package indices relevant for Python-based scientific computing—PyPI, the Python package index, for the package manager `pip`, and conda-forge, a community-based channel for the package manager `conda`—to easily make Ubermag available to a wider audience. Furthermore, the releases can help improve reproducibility by (i) making it possible to precisely record the versions of packages used to carry out a specific study in a standardised format and (ii) can simplify reproducing the same software environment to reproduce simulation results of a publication. One example for this, as mentioned before, is our publication on the stability of multiple Bloch points (Lang et al., 2023a) and the accompanying repository (Lang et al., 2022). Here, we specify the required conda packages to re-run our simulations and allow re-executing the notebooks in this environment using Binder.

Key elements to make Ubermag accessible to a wider audience are documentation and community interaction. The documentation of Ubermag is divided into API reference and Jupyter Notebooks. The notebooks focus either on a specific set of functionality (e.g. plotting with Holoviews) or on how to solve a particular research question (e.g. simulating a skyrmion in a disk). Users can start from an existing notebook and modify it for their needs. To make the documentation more accessible I have re-created the website of Ubermag. The new website combines the documentation of all individual sub-packages in one central place. This simplifies browsing the documentation and jumping back and forth between the different sub-packages. Several users have confirmed that the new website makes the available learning resources much more accessible. All notebooks shown on the website contain a link to Binder on which users can execute and modify the notebook inside the browser without installing any software on their own machine. This provides a good starting point for new users.

The extensive documentation in the form of notebooks and their easy execution on Binder has also been used for teaching numerical methods as part of the class “Magnetic Materials and Applications” in the Department of Materials Science and Engineering at the University of Illinois at Urbana-Champaign (Lonsky et al., 2023). As part of this class, small groups of students work together on micromagntic problems using Ubermag. The authors report that the project work seems to facilitate a more in-depth understanding of the course contents. I was involved in this work via the development of Ubermag, work on the tutorial notebooks for Ubermag, and maintenance of required configuration for the execution on Binder.

We use a number of different channels to communicate with Ubermag users. We have a mailing list to notify users about new releases, and we provide support in a dedicated GitHub repository and on a public chat instance on Zulip. All channels can also be used to report bugs or request new features. Support queries are generally open to the public and provide a valuable additional source of information in addition to the documentation. Several Ubermag tutorials have been organised to which I contributed.

In hindsight, in particular the use of GitHub issues as a forum works quite well. The public chat instance has only been used by very few people and the number of subscriptions to the mailing list is relatively small. In parts, this is probably due to the fact that GitHub issues was the first communication channel that we have used for community interactions.

As open-source software, Ubermag can be freely used by anyone doing micromagnetic simulations. The total number of users is difficult to assess and fluctuating. The two papers describing Ubermag, Beg et al. (2017b, 2022), have been cited 16 times in 2021 and 28 times in 2022 according to Google Scholar. Web of Science reports 9 citations in 2021 and 17 citations in 2022. The GitHub issues,[6] that serve as an archive of user queries, have collected more than 200 different topics.

[6] https://github.com/ubermag/help/issues

Chapter 4

Multiple Bloch points

Preface

The work described in this chapter has been published as Lang et al. (2023a). Compared to the publication, the introduction is shortened as it would duplicate information given in Sec. 2.8.4. The discussion of the simulation procedure in Sec. 4.2 and 4.3 and the discussion of the classification of Bloch points in Sec. 4.5 have been extended. All results in this chapter can be reproduced from the accompanying repository (Lang et al., 2022).

4.1 Introduction

In this chapter, we demonstrate that chiral two-layer nanostrips can host multiple Bloch points in an arbitrary combination of the two different Bloch-point types. First, we discuss the two-layer system in Sec. 4.2 and the simulation scheme used to obtain arbitrary numbers of Bloch points in a controlled fashion in Sec. 4.3. In Sec. 4.4, we explain the two different configurations containing two Bloch points. We have developed a classification scheme to automatically detect Bloch points in the simulation results, which we present in Sec. 4.5. Such a scheme is required to classify the large number of simulations performed in this work. In Sec. 4.6, we demonstrate that multiple Bloch points can coexist in rectangular two-layer nanostrips. We find that all possible sequences of head-to-head and tail-to-tail Bloch points can be realised. Different combinations have different energy densities depending on the number of neighbouring Bloch points of the same type. We focus on systems containing up to eight Bloch points initially. Based on these results, we can predict a suitable strip geometry for an arbitrary number of Bloch points. We conclude with a demonstration of encoding a 10-byte string using 80 Bloch points: we identify one Bloch-point type with the binary “1” and the other type with the binary “0” to encode and store the equivalent of an 80-bit long sequence (Sec. 4.7).

4.2 System

We simulate rectangular two-layer nanostrips with opposite chirality (opposite sign of D) in the two layers. We vary strip length l and width w, the thickness of both layers is fixed (bottom layer: 20 nm, top layer: 10 nm). We focus on up to eight Bloch points and accordingly choose nanostrips with lengths between 100 nm and 1400 nm, and widths between 100 nm and 200 nm. The geometry is shown in Fig. 4.1, which we discuss in more detail in the next section.

The energy equation

$$E = \int \mathrm{d}^3 r \, (w_{\mathrm{ex}} + w_{\mathrm{dmi}} + w_{\mathrm{d}}) \tag{4.1}$$

contains exchange energy density w_{ex}, bulk Dzyaloshinskii-Moriya energy density w_{dmi}, and demagnetisation energy density w_{d}. The magnetisation dynamics is simulated using the Landau-Lifshitz-Gilbert equation (Landau & Lifshitz, 1935; Gilbert, 2004), discussed in Sec. 2.4:

$$\frac{\partial \mathbf{m}}{\partial t} = -\gamma \mathbf{m} \times \mathbf{H}_{\mathrm{eff}} + \alpha \mathbf{m} \times \frac{\partial \mathbf{m}}{\partial t}, \tag{4.2}$$

where γ is the gyromagnetic ratio, α is the Gilbert damping constant, and $\mathbf{m}$ the normalised magnetisation:

$$\mathbf{m} = \frac{\mathbf{M}}{M_{\mathrm{s}}}. \tag{4.3}$$

Material parameters are based on FeGe (Beg et al., 2015): $A = 8.87\,\mathrm{pJ\,m^{-1}}$, $D = 1.58\,\mathrm{mJ\,m^{-2}}$, $M_{\mathrm{s}} = 384\,\mathrm{kA\,m^{-1}}$, and $\alpha = 0.28$ (Beg et al., 2017a). We use finite-difference micromagnetic simulations to minimise the energy. All simulations are done using Ubermag (Beg et al., 2022) with OOMMF (Donahue & Porter, 1999) as the computational backend and an extension for DMI of crystallographic point group T (Cortés-Ortuño et al., 2018b, 2018a).

In a recent work by Winkler et al. (2023), we have compared the Bloch point in the two-layer system in micromagnetic and atomistic simulations. We could show that both models produce qualitatively similar results, both for the statics and the dynamics of the Bloch point. Deviations between the two models are predominantly caused by different discretisation sizes. The micromagnetic model reproduces the atomistic model when the cell size matches the atomistic lattice spacing. Hence, the micromagnetic model is suitable to describe systems containing Bloch points despite the fact that the assumption of slowly varying magnetisation is not fulfilled in the close vicinity of the singularity.

4.3 Simulation procedure

All simulations in this study follow a three-step initialisation and minimisation scheme: (i) initialisation, (ii) fixed minimisation, (iii) free minimisation. In the micromagnetic framework the system is studied at zero temperature, i.e. without thermal fluctuations. Therefore, it is

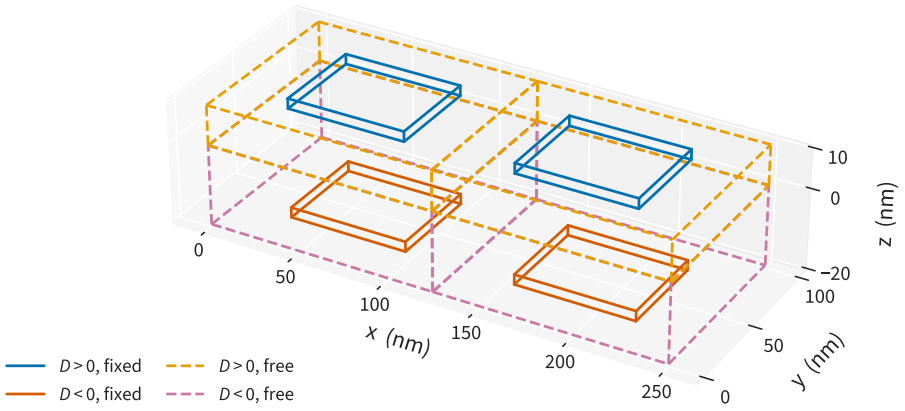

FIGURE 4.1: Subregions used for the initialisation and fixed energy minimisation, and to define the two-layer geometry with opposite chirality (opposite sign of D) in the two layers for a nanostrip that shall contain two Bloch points. The magnetisation inside the subregions shown with solid lines is kept fixed during the first energy minimisation. Magnetisation in the top fixed subregions is initialised with reversed z component of the magnetisation (see Fig. 4.2). In the plot the z axis is stretched for better visibility. The fixed subregions are located at the strip boundaries.

only possible to find local minima that are accessible from the initial configuration. Starting from experimentally feasible initial configurations, such as full saturation, we are able to find magnetisation configurations containing a single or multiple Bloch points depending on the strip geometry.

To facilitate the process of studying arbitrary Bloch-point configurations, independent of the strip geometry, in a systematic way, we have developed a simulation scheme that guarantees a magnetisation configuration containing a predictable number of Bloch points. We note that this scheme can probably not be applied directly to an experimental setup. In this section, we discuss two examples for configurations containing one and two Bloch points, respectively.

For the initialisation, step (i), we start by dividing the nanostrip into equally sized regions (in the x direction), one region per Bloch point. Each region is then divided into four subregions. Figure 4.1 shows the eight subregions that are used to obtain a configuration containing two Bloch points. Four subregions are located below $z = 0$ and have a negative DM energy constant D, and four above $z = 0$ with positive D. The four small subregions, shown with solid lines, are located at the top and bottom sample boundaries. Each of the small subregions is contained within one surrounding subregions shown with dashed lines. The strip geometry in Fig. 4.1 is enlarged in the z direction for better visibility.

To enforce the formation of a Bloch point, the magnetisation in each region is initialised as follows: for a head-to-head Bloch point, we initialise the small subregions at the top sample boundary with $\mathbf{m} = (0, 0, -1)$ and all other cells with $\mathbf{m} = (0, 0, 1)$. A region hosting a tail-to-tail Bloch point is initialised with reversed z component of the magnetisation. Figure 4.2a shows an example for a configuration containing a single HH Bloch point. The system geometry

is 100 nm × 100 nm × (10 + 20) nm. This system only needs four subregions, i.e. one "column" of subregions in Fig. 4.1 (e.g. only the subregions for $x < 125$ nm).

We then minimise the energy in two steps. During the first energy minimisation, step (ii), we keep the magnetisation in the small subregions at the sample boundaries, shown with solid lines in Fig. 4.1 and highlighted in Fig. 4.2b, fixed. This ensures the formation of the Bloch point at the interface between the two layers in a controlled manner. During the second energy minimisation, step (iii), magnetisation in all cells can freely change and Bloch points could move in any direction to further minimise the energy of the configuration. In this step, the system can find the local energy minimum, leading to the magnetisation shown in Fig. 4.2c.

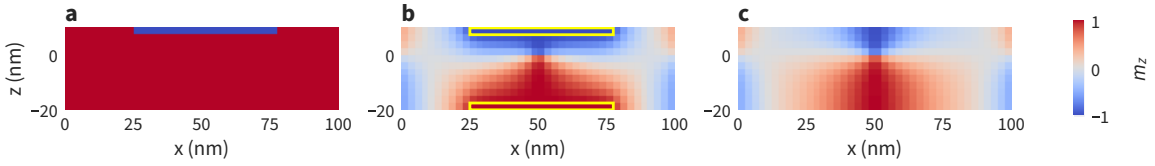

FIGURE 4.2: Initialisation and energy minimsation for a single head-to-head Bloch point (cross-section at $y = 50$ nm). (a) The magnetisation is initialised with $\mathbf{m} = (0, 0, 1)$ with the exeption of a top subregion where $\mathbf{m} = (0, 0, -1)$. (b) During the first energy minimisation, the magnetisation is kept fixed inside the yellow-highlighted subregions (see Fig. 4.1 for a 3D plot). The formation of a Bloch point is enforced by the opposite m_z values in the two fixed subregions. (c) During the second energy minimisation, magnetisation in all cells can freely change.

4.4 Two Bloch points

A pair of neighbouring Bloch points in multi-Bloch-point configurations can occur in two fundamentally different combinations. The Bloch points can either be of the same type, for example: a head-to-head (HH) Bloch point next to another HH Bloch point (HH-HH) as shown in the right column of Fig. 4.3. Alternatively, the Bloch points can be of opposite type, for example a HH Bloch point next to a tail-to-tail (TT) Bloch point (HH-TT) as shown in the left column of Fig. 4.3.

The topmost row (Fig. 4.3a, b) shows a schematic drawing of the nanostrip highlighting the two-layer structure and the geometry. Additionally, position and type of the Bloch points visible in the simulations are indicated with arrows, where the colour of the arrows encodes the z component of the magnetisation (red: $+z$, blue: $-z$).

Figure 4.3c and d show 3D renderings of the simulation results. The isosurfaces (as used by Hertel & Schneider, 2006 to visualise magnetic vortices) show $m_z = \pm 0.9$ ($\mathbf{m}$ is the normalised magnetisation), colour indicates the z component. The isosurfaces above/below the Bloch point have a paraboloidal-like shape pointing towards the Bloch point (similar to the single-Bloch-point simulation results in Fig. 2.7c, d). The Bloch point itself is not directly visible in this visualisation. The configuration in Fig. 4.3d additionally contains one antivortex between

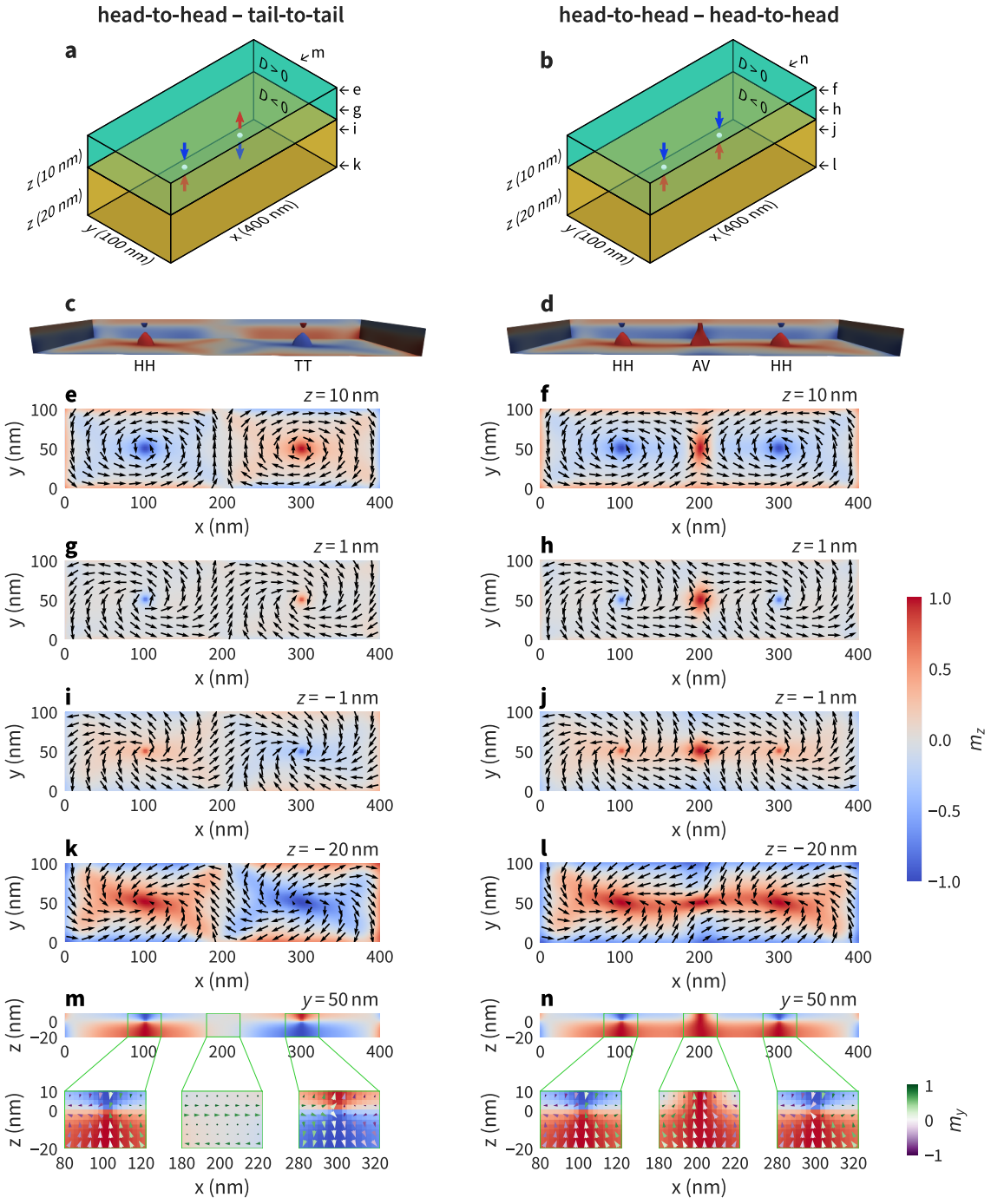

FIGURE 4.3: Magnetisation profile of the two fundamentally different configurations containing two Bloch points: opposite-type Bloch points (head-to-head and tail-to-tail, left column) and same-type Bloch points (head-to-head and head-to-head, right column). The 3D renderings in (c) and (d) show isosurfaces for $m_z = \pm 0.9$, colour indicates the z component. Several different cut planes in xy and xz are shown to reveal the three-dimensional structure of the Bloch points forming at the interface ($z = 0$ nm). For the xz plane (subfigures m and n) we also show enlarged plots around the Bloch point and antivortex position. The cones in (m) and (n) are coloured according to their m_y component, as indicated by the small colour bar in the right bottom corner of the figure.

the two Bloch points. The $m_z = 0.9$ isosurface of the antivortex extends throughout the whole thickness (z direction) of the two-layer system. The antivortex core shrinks towards the top sample boundary.

To reveal the full three-dimensional structure of the magnetisation field surrounding the Bloch points the magnetisation of each configuration is plotted in five different cut planes for each column (as indicated in the schematic drawings Fig. 4.3a, b). Four different cut planes show the magnetisation in the xy plane (Fig. 4.3e – l), at the top sample boundary ($z = 10\,\mathrm{nm}$) in Fig. 4.3e and f, above the interface ($z = 1\,\mathrm{nm}$) in Fig. 4.3g and h, below the interface ($z = -1\,\mathrm{nm}$) in Fig. 4.3i and j, and at the bottom sample boundary ($z = -20\,\mathrm{nm}$) in Fig. 4.3k and l. Colour encodes the z component of the magnetisation vector field, arrows the in-plane component.

Figure 4.3m and n show the z component of the magnetisation in an xz cut plane going through the Bloch points at $y = 50\,\mathrm{nm}$. Magnified subplots show the full magnetisation around the Bloch-point positions and in the centre region between the two Bloch points. The colour of the cones in the magnified areas encodes the y component of the magnetisation vector field.

The results shown in Fig. 4.3 show that Bloch points form at $x \approx 100\,\mathrm{nm}$ and $x \approx 300\,\mathrm{nm}$ in both cases, i.e. in both columns. Bloch-point pairs of the opposite type (Fig. 4.3, left column) show opposite circularity of the magnetisation within the xy plane around the Bloch-point cores. In this case, the in-plane magnetisation (xy component) between the two Bloch points (from $x \approx 100\,\mathrm{nm}$ to $x \approx 300\,\mathrm{nm}$) shows a smooth transition from one Bloch point to the other. Focusing only on the top layer (or focusing only on the bottom layer), the configuration can also be described as a micromagnetic configuration containing two vortices of opposite polarisation and circularity (most clearly seen in Fig. 4.3e). In contrast, an additional antivortex forms between two same-type Bloch points (Fig. 4.3, right column) at $x \approx 200\,\mathrm{nm}$ to mediate between the incompatible magnetisation configurations that originate from the two same-circularity vortices. Differing from the magnetisation of the Bloch-point cores, the magnetisation of the antivortex core (at $x \approx 200\,\mathrm{nm}$) does not change significantly along the z direction (middle inset in Fig. 4.3n). This configuration can be described as a micromagnetic configuration containing a cross-tie domain wall (Huber et al., 1958; Middelhoek, 1963) in each layer. The cross-tie wall consists of alternating vortices and antivortices, the structure is most clearly visible in Fig. 4.3f.

4.5 Classification

In the micromagnetic framework, it is not possible to directly observe Bloch points because of the fixed norm of the magnetisation vector. As discussed in Sec. 2.8.4, a single Bloch point is characterised by the integral value of the topological charge density over a closed surface S

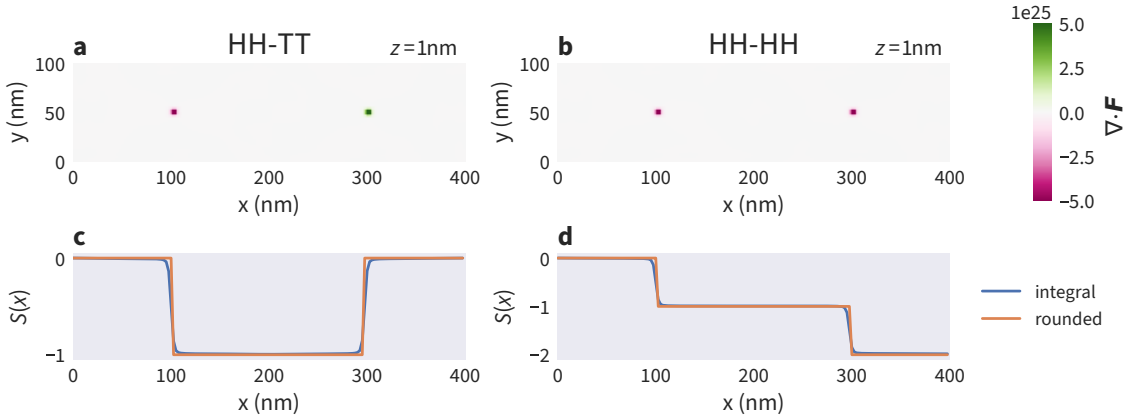

FIGURE 4.4: Classification of the two configurations containing two Bloch points shown in Fig. 4.3. The divergence of the emergent magnetic field for the two opposite- and same-type Bloch points is shown in panels (a) and (b), respectively. The xy plane visualised here is located at $z = 1$ nm, just above the interface. (c, d) The result of the convolution (4.5), which is used to identify the occurrence of Bloch points and their type due to the steps $\Delta S = \pm 1$.

surrounding the Bloch point (Eq. 2.47):

$$S = \frac{1}{4\pi\hbar} \int_s \mathrm{d}\mathbf{s} \cdot \mathbf{B}^\mathrm{e} = \pm 1, \tag{4.4}$$

where $\mathbf{B}^\mathrm{e}$ is the emergent magnetic field defined in Eq. 2.37. To detect a single Bloch point in a sample the integral can be computed over the whole sample surface and the exact position of the Bloch point does not need to be known.

This method is not directly applicable to multiple Bloch points when their positions are unknown: the sign of the topological charge of a Bloch point depends on its type (HH: $S = -1$, TT: $S = +1$). Therefore, contributions to the surface integral from Bloch points of opposite type cancel out. Figure 4.4 shows the divergence of the emergent field $\nabla \cdot \mathbf{B}^\mathrm{e}$ for a HH and a TT Bloch point (a) and two HH Bloch points (b), the two configurations discussed in Fig. 4.3.

To classify nanostrips that potentially contain multiple Bloch points, we compute the convolution of the divergence of the emergent magnetic field with a Heaviside step function:

$$S(x) = \frac{1}{4\pi\hbar} \int_{V'} \mathrm{d}^3 r' \, \Theta(x - x') \nabla_{\mathbf{r}'} \cdot \mathbf{B}^\mathrm{e}(\mathbf{r}'). \tag{4.5}$$

Due to numerical inaccuracies, the result of the integral deviates from integer values. By translating the surface integral into a volume integral over the divergence of the emergent magnetic field using divergence theorem the accuracy can be improved by roughly one order of magnitude.

In our set-up Bloch points are expected to be distributed along x following the strip geometry, which justifies computing S as a function of x. The convolution can be interpreted as computing a series of integrals over increasing sub-volumes V' of the nanostrip starting at the left boundary

($x = 0$ nm). We round $S(x)$ to integer values and count steps ΔS in this function. Rounding to integer values is justified because deviations from integer values in the integral are a direct consequence of the limited accuracy due to the discretisation (see below).

Figure 4.4c and d show $S(x)$ for the two example configurations discussed in Fig. 4.3. A head-to-head Bloch point is identified by $\Delta S = -1$, a tail-to-tail Bloch point by $\Delta S = +1$ corresponding to the topological charge of a Bloch point being $S = \pm 1$.

To confirm that the rounding to integer values is justified, we compare the deviations of $S(x)$ from integer values for different cell sizes. Figure 4.5a shows an example of a configuration containing eight Bloch points in the pattern TT-HH-TT-TT-TT-TT-HH-TT. We compute $S(x)$ for three different cell sizes with cubic cells with edge lengths $l_c = 5$ nm (Fig. 4.5b), $l_c = 2.5$ nm (Fig. 4.5c), and $l_c = 1$ nm (Fig. 4.5d). For each cell size, we show the integral result (solid lines) and rounded values (dashed lines). We can see that the difference (i.e. the inaccuracy) significantly decreases with decreasing cell size. For $l_c = 1$ nm integral and rounded values cannot be distinguished visually. We use a cell edge length $l_c = 2.5$ nm in all simulations.

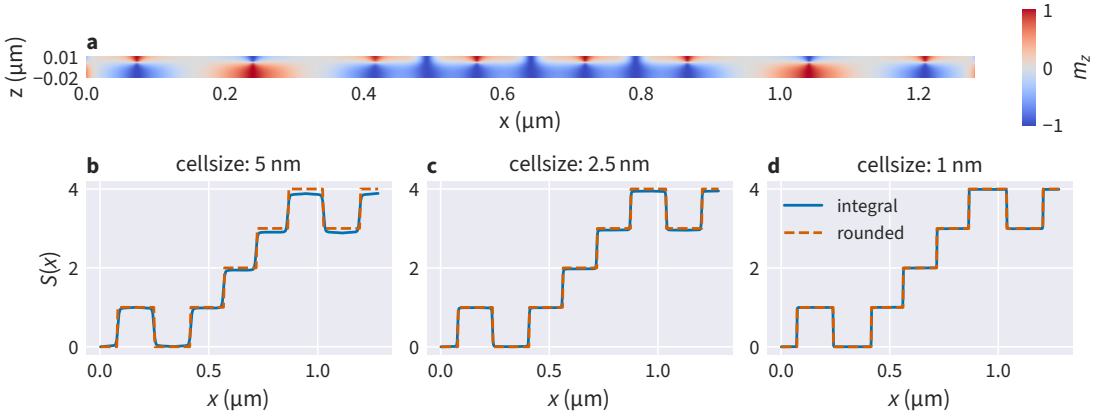

FIGURE 4.5: Accuracy of the classification for a configuration containing eight Bloch points. (a) shows a cross-section of the magnetisation of configuration TT-HH-TT-TT-TT-TT-HH-TT in the xz plane located at the Bloch-point position ($y = 50$ nm). With decreasing cellsize—cell edge lengths: 5 nm (b), 2.5 nm (c), and 1 nm (d)—the difference between the integral $S(x)$ and the corresponding integer values decreases.

4.6 Parameter-space diagram and energy density

The spatially averaged energy density (total energy of the system divided by the system volume) of a Bloch-point configuration depends on the number of Bloch points, their individual types, and the strip geometry. Furthermore, different spatial arrangements can be realised, e.g. four Bloch points on a line, or in the corners of a rectangle or diamond shape. Here, we only consider magnetisation configurations containing between one and eight Bloch points in a row, distributed in x direction (strip length) and centred in y direction (strip width).

In Fig. 4.3 we have seen the two fundamentally different configurations containing two Bloch points, head-to-head and tail-to-tail (HH-TT), and head-to-head and head-to-head (HH-HH). Now, we investigate a system containing three Bloch points. In total, eight configurations can be realised. Three configurations are fundamentally different, namely HH-HH-HH, HH-HH-TT, and HH-TT-HH, because they contain distinct numbers of additional antivortices. The other five configurations are equivalent either because HH and TT swap roles (e.g. TT-TT-TT), or because of the symmetry of the system geometry along the x axis (e.g. TT-HH-HH).

The fundamentally different configurations (HH-HH-HH, HH-HH-TT, HH-TT-HH) are shown in Fig. 4.6d in a system with strip length $l = 400\,\mathrm{nm}$. We find one and two additional antivortices (AVs) for configurations HH-HH-TT and HH-HH-HH, respectively. The table in Fig. 4.6 lists all eight configurations and the respective number of antivortices. In different terms, the three configurations in Fig. 4.6d could also be described as (in each layer) containing one long cross-tie wall (top), a cross-tie wall and one vortex (middle), and three vortices (bottom).

For each of the three fundamentally different configurations, we compute the spatially averaged energy density of the micromagnetic configuration and plot the three values in Fig. 4.6a (at $l = 400\,\mathrm{nm}$).

We find that the micromagnetic configuration containing three Bloch points in the HH-TT-HH configuration has the lowest energy density and the micromagnetic configuration containing three Bloch points in the HH-HH-HH configuration the highest energy density. Hereinafter, we will refer to a micromagnetic configuration containing n Bloch points as the n-Bloch-point configuration to simplify the text. Note that we always mean the entire micromagnetic configuration with embedded Bloch points and not isolated Bloch points, e.g. when talking about the "energy of the Bloch points" (which should be read as "energy of the micromagnetic configuration containing Bloch points"). It is well-known that the Bloch points "themself", i.e. the point singularities, do not affect the energy of the micromagnetic configuration (Feldtkeller, 1965). We will later discuss in more detail how the presence of antivortices between Bloch points generally increases the energy density of the system. The alternating configuration HH-TT-HH does not contain any antivortices, as these are only needed to mediate the local rotation of the magnetisation between neighbouring vortices that enclose Bloch points of the same type.

The three yellow lines (filled and open diamonds) in Fig. 4.6a show the spatially averaged energy density for the three different configurations as a function of strip length. Not all configurations are stable for all strip lengths: for example the HH-HH-TT configuration is only stable for $l \geq 300\,\mathrm{nm}$. If we try to create the three-Bloch-point configuration HH-HH-TT in a shorter nanostrip, e.g. at $l = 275\,\mathrm{nm}$, then the configuration is not stable and will change into a lower-energy configuration, in this case the HH-TT configuration containing only two Bloch points. In other words, the cross-tie walls enclosing the HH-HH Bloch-point pair are not stable in too short nanostrips and collapse. This has in detail been studied for cross-tie walls in single-layer materials (Hertel & Schneider, 2006). We can see that the energy generally

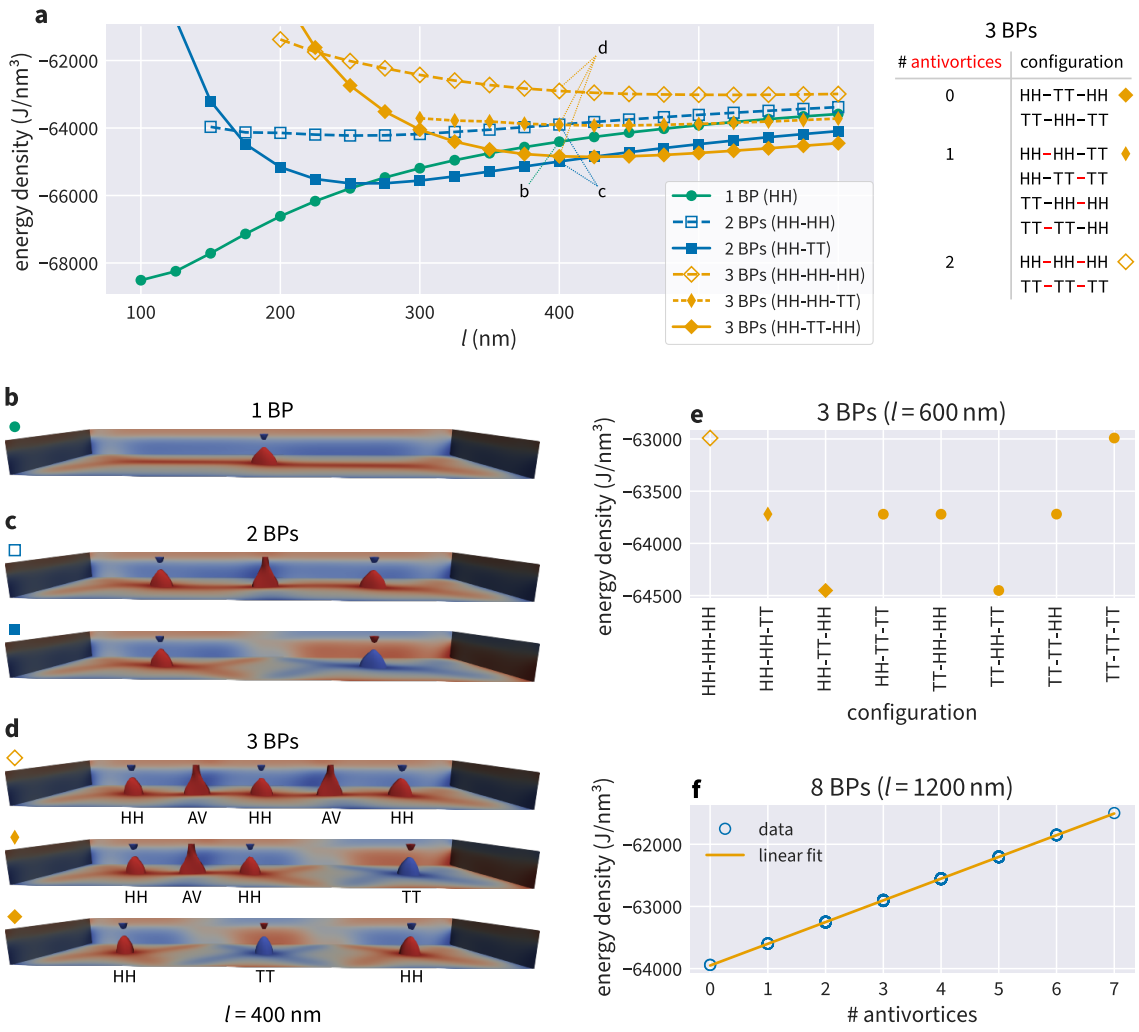

FIGURE 4.6: (a) Energy densities for energetically different micromagnetic configurations containing at most three Bloch points for different strip lengths l at a strip width $w = 100\,\text{nm}$. Simulations have been performed in steps of $\delta l = 25\,\text{nm}$, the solid lines are shown to guide the eye. (b – d) Magnetisation profiles for the six different configurations shown in (a) at $l = 400\,\text{nm}$. Isosurfaces show $m_z = \pm 0.9$, colour indicates the z-component. (e) Energy density for all possible configurations containing three Bloch points. The first three configurations are show in (d) as indicated with the distinct marker symbols (at a different strip length). The table in (a) lists all different configuration containing three Bloch points, highlighting the number and position of the additional antivortices in the different configurations. (f) Energy densities for all configurations containing eight Bloch points. Energy densities for a fixed number of antivortices are nearly identical but cause some "smearing" of the marker symbols.

increases with increasing number of antivortices as mentioned in the previous paragraph. However, there is a deviation visible for $l \leq 225$ nm where the HH-HH-HH configuration has a lower energy density than the HH-TT-HH configuration. This deviation is a result of the short strip length near the stability limit. We exclude these regions near the minimal stability strip length in the rest of our discussion.

The blue filled and open squares in Fig. 4.6a show the energy density for a system containing only two Bloch points. The corresponding magnetisation field for $l = 400$ nm is visualised in Fig. 4.6c, and in more detail in Fig. 4.3. The green circles in Fig. 4.6a show the energy density for a configuration containing a single Bloch point and its magnetisation configuration for $l = 400$ nm is shown in Fig. 4.6b.

For a given strip length l we describe the configuration with the lowest energy density as the energetically most favourable configuration: below $l = 250$ nm a single Bloch point (green circles) has the lowest energy density. (Note that the energy of the micromagnetic configuration containing one Bloch point is lower than the energy of a vortex expanding throughout the system because of the two-layer system with opposite chirality in the two layers.) Two opposite-type Bloch points (blue squares) have the lowest energy density for $250 \text{ nm} < l <= 400 \text{ nm}$ and three Bloch points of alternating opposite type (yellow diamonds) have the lower energy density above $l = 400$ nm.

Figure 4.6e shows a representation of the energy densities for all possible three-Bloch-point configurations at $l = 600$ nm. As already discussed, there are three fundamentally different configurations characterised by the number of additional antivortices contained in the configuration (as shown in the table in Fig. 4.6). Different realisations of the same configuration type (swapping HH and TT or using the strip symmetry) exhibit the same energy density.

In Fig. 4.6a we have seen that the number of Bloch points in the energetically most favourable configuration changes depending on the strip length l. Figure 4.7 contains a parameter-space diagram showing the energetically most favourable configuration as a function of the strip length and strip width, using the Bloch point number as a label. To create Fig. 4.7, we ask for each strip length l and a given strip width w, which configuration has the lowest energy density. For example: all data points in Fig. 4.6a are for a width of $w = 100$ nm. Close to $l \approx 400$ nm, we see that for $l \leq 400$ nm the two-Bloch-point configuration HH-TT (blue squares) has the lowest energy density but that for $l > 400$ nm the three-Bloch-point configuration HH-TT-HH (yellow diamonds) has the lowest value. Figure 4.7 shows (for $w = 100$ nm on the y axis) that the two-Bloch-point configuration has the lowest energy density up to $l \approx 400$ nm, and the three-Bloch-point configuration for larger l (up to $l \approx 600$ nm). All configurations with lowest energy density are of the alternating Bloch-point type, i.e. left and right neighbours of a HH Bloch point are always of type TT, and vice versa (see discussion below), and hence do not contain additional antivortices.

Figure 4.7 shows that with increasing strip length, the number of Bloch points that are present in the lowest-energy-density configuration (as shown Fig. 4.6a for $l \leq 600$ nm) increases: for

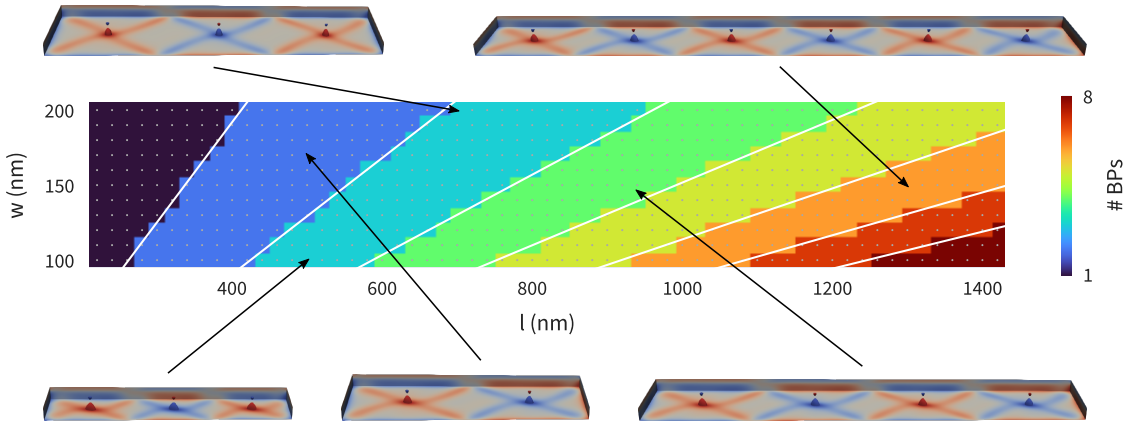

FIGURE 4.7: Parameter-space diagram showing the energetically most favourable Bloch point number as a function of length l and width w. All configurations contain Bloch points of alternating opposite type (so the micromagnetic configurations do not contain additional antivortices). Magnetisation profiles for selected configurations reveal the similarity of the different configurations, isosurfaces show $m_z = \pm 0.9$.

nanostrips with lengths above $l \approx 1300\,\text{nm}$ and width $w = 100\,\text{nm}$, we find eight Bloch points. Furthermore, Fig. 4.7 shows that increasing the width of the nanostrip leads to a reduced number of Bloch points in the energetically most favourable configuration.

Figure 4.7 also shows magnetisation profiles for selected configurations revealing the similarities in the magnetisation profile in different strip geometries. The isosurfaces show $m_z = \pm 0.9$, colour indicates the z component. All configurations shown in Fig. 4.7 contain Bloch points of alternating opposite type, i.e. all the lowest-energy configurations do not contain antivortices.

In the discussion of the fundamentally different configurations containing three Bloch points, we have noted that the different configurations can be characterised by the number of additional antivortices contained in the structure. Figure 4.6f summarises similar findings for eight Bloch points where configurations can contain between zero antivortices (Bloch points of alternating opposite type) and seven antivortices (all Bloch points of the same type). In total, 256 configurations can be realised. The plot in Fig. 4.6f shows the data for all configurations and a linear fit to the data. Different realisations with the same number of antivortices cannot be distinguished in this plot as their energies are nearly identical, but cause slight vertical shifts of the blue open circles used to mark the energy densities of the different configurations for intermediate numbers of antivortices. The energy density increases linearly with the number of antivortices (or equivalently, the cross-tie wall size).

There is an important difference between three Bloch points (Fig. 4.6e) and eight Bloch points (Fig. 4.6f). For a fixed number of antivortices, all different three-Bloch-point configurations are equivalent because of the system's symmetry (globally replacing HH with TT and vice versa (and adjusting the antivortex polarisation) or π rotations around the z direction) and therefore must have the same energy density. Let us give two examples: we start from the configuration HH-HH-TT. First, we can obtain an equivalent configuration by swapping HH

and TT Bloch points, namely the configuration TT-TT-HH. Globally swapping all Bloch-point types (and adjusting the antivortex polarisation) does not affect the system's physics in the context discussed here. Second, we can rotate the system around the z direction and obtain the configuration TT-HH-HH. Again, the two configurations are equivalent. However, for eight Bloch points we additionally find that different configurations that are not related via symmetry (globally swapping HH and TT or rotating the system around the z direction) also have the same energy density if they contain the same number of antivortices. For example, the configurations HH-HH-HH-HH-HH-HH-HH-TT and HH-HH-HH-HH-TT-TT-TT-TT both contain 6 antivortices (located between neighbouring same-type Bloch points, i.e. HH-HH and TT-TT pairs) but cannot be transformed into each other by swapping HH and TT or rotating the system. Yet, they exhibit the same spatially averaged energy density. Our findings suggest that the energy density of the micromagnetic configuration around the Bloch points is independent of the configuration around other Bloch points in the system (the Bloch point itself, i.e. the point singularity, is known to not affect the energy of the micromagnetic configuration containing it Feldtkeller, 1965). The energy density of any Bloch-point configuration can be obtained from a configuration containing Bloch points of alternating opposite type with additional contributions originating from the additional antivortices between neighbouring same-type Bloch points.

This is the reason for the lowest-energy-density configurations shown in Fig. 4.7 consisting of pairs of Bloch points of alternating type: for same-type neighbours an antivortex is required to mediate the magnetisation between the Bloch points of the same type, and the presence of such antivortices would increase the spatially averaged energy density.

We can make one additional observation in Fig. 4.6a. The energy density of a configuration changes as a function of strip length l. All configurations containing two or three Bloch points have one energy minimum at a certain length that we call the *optimal length* l_o. For example, the optimal length for the HH-TT configuration (blue filled squares in Fig. 4.6a) is $l_\mathrm{o} \approx 275\,\mathrm{nm}$.

4.7 Predicting strip geometries for larger systems

So far, we have focused on small systems containing at most eight Bloch points. Based on this information we can predict strip geometries suitable for an arbitrary number of Bloch points.

Figure 4.6a shows that meta-stable configurations containing multiple Bloch points can be realised over a broad range of strip lengths but need a certain minimal strip length. This minimal length depends on the number of Bloch points and additional antivortices in the configuration. In our simulations, we also see that a certain maximum strip length cannot be exceeded for a given configuration. If the strip is too long, the configuration could not be stabilised and additional Bloch points appear. Furthermore, Fig. 4.6a shows that all configurations have a minimum in the energy density at a certain optimal length l_o.

To predict strip geometries suitable for an arbitrary number of Bloch points we focus on configurations containing up to eight Bloch points of alternating opposite type. We find that the optimal length l_o increases linearly with the number of Bloch points (Fig. 4.8c) with the slope defining the optimal Bloch point spacing s_o. Furthermore, we find that s_o increases linearly with increasing strip width (Fig. 4.8d). We obtain $s_{o,w=100\,\mathrm{nm}} \approx 165\,\mathrm{nm}$ and $s_{o,w=200\,\mathrm{nm}} \approx 272\,\mathrm{nm}$ with an estimated accuracy of $\delta s_o \approx 3\,\mathrm{nm}$. These observations lead to our working hypothesis that the ideal Bloch-point spacing s_o is independent of the number of Bloch points in the system and suitable to predict geometries for more than eight Bloch points. This prediction can be used for arbitrary configurations not only alternating opposite-type Bloch points.

As an illustrative example, we simulate one specific configuration containing 80 Bloch points, encoding the 10-character word `Blochpoint` in ASCII code (eight bits per letter). We simulate a strip with the predicted length $l = 80 s_o = 13.2\,\mu\mathrm{m}$ at a width of $w = 100\,\mathrm{nm}$ and with $s_o = 165\,\mathrm{nm}$.

We minimise the energy of a suitable initial configuration resulting in the 80-bit configuration as shown in Fig. 4.8a, b. The cross sections show the xy plane at $z = 1\,\mathrm{nm}$ (Fig. 4.8a) and the xz plane at $y = 50\,\mathrm{nm}$ (Fig. 4.8b). Note that the aspect ratio is not correct in order to improve visibility. Figure 4.8e shows contour lines for m_z for a part of the nanostrip (correct aspect ratio) as indicated in Fig. 4.8a. Bloch points in Fig. 4.8e are located at the small red and blue dots. The larger red circles ($m_z > 0.5$) show antivortices between same-type Bloch points.

To test the stability of the 80-Bloch-point configuration, we apply a short magnetic field pulse in the $+y$ direction ($H = 25\,\mathrm{mT}/\mu_0$, applied for $t = 0.5\,\mathrm{ns}$). The modified magnetisation field configuration at the end of the 0.5 ns period is shown in Fig. 4.8f. Then, we set the applied field back to zero and let the system evolve freely by carrying out a time integration. We find that the magnetisation converges back to the initial state: Fig. 4.8g shows the configuration after $t = 5\,\mathrm{ns}$ of free relaxation.

To understand the robustness of the predicted geometry, we vary the strip length l and find that the desired 80-Bloch-point configuration can be stabilised over a range of strip geometries. The minimal strip length is around $0.66 l_o$ the maximal strip length around $4 l_o$.

Within the range of stability of the 80-bit configuration ($0.66 l_o \leq l \leq 4 l_o$), we find that the length l_o is closer to the lower stability boundary ($\approx 0.66 l_o$) than to the upper limit ($\approx 4 l_o$). This is consistent with the energy density curve for the HH-TT configuration in Fig. 4.6a (blue filled squares), where we see that the energy density as a function of the strip length is asymmetric and that its energy minimum, located at strip length l_o, is located at a comparatively small strip length within the range of possible strip lengths over which the configuration is meta-stable (stability limits are not visible in Fig. 4.6a).

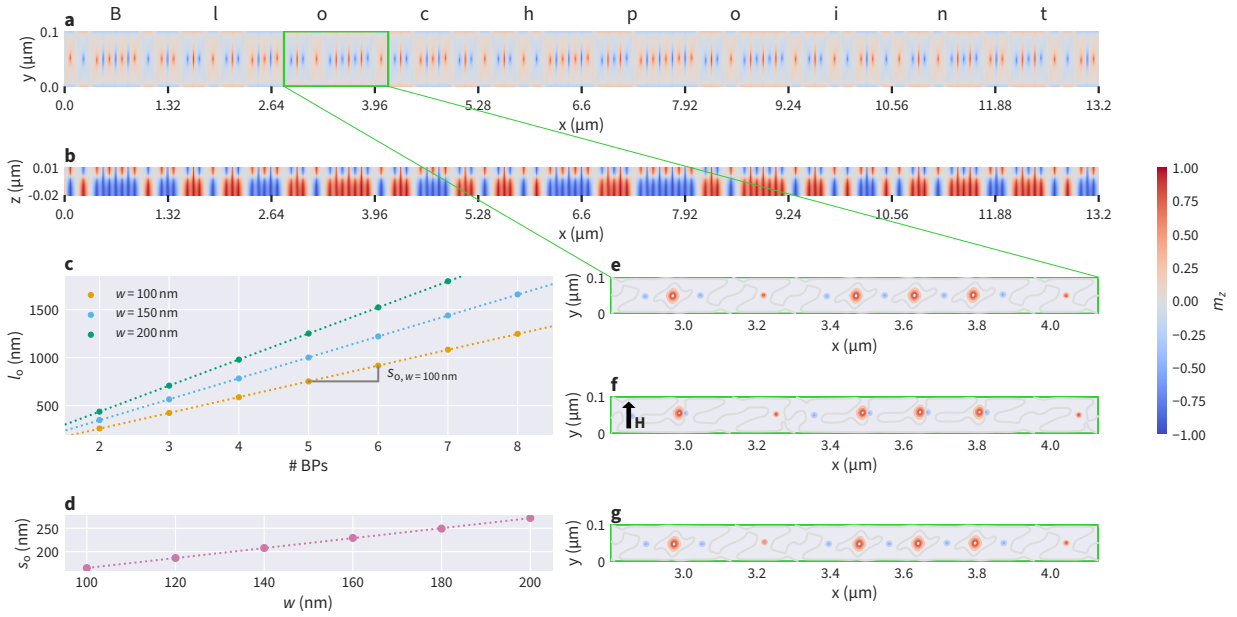

FIGURE 4.8: (a, b) ASCII encoding of the string Blochpoint using 80 Bloch points, a HH Bloch point represents a binary "1" and a TT Bloch point represents a binary "0". Cross sections show (a) the xy plane at $z = 1$ nm and (b) the xz plane at $y = 50$ nm. The strip length is chosen according to the predicted value for a nanostrip with width $w = 100$ nm. Labels on the x axis mark blocks of eight Bloch points, i.e. individual bytes. Note that the aspect ratio is not correct in order to improve visibility. (c) Optimal lengths l_o for two to eight Bloch points. The fit is used to predict lengths for more than eight Bloch points. (d) Optimal Bloch point distance s_o as a function of strip width w. (e – g) show an enlarged part of the nanostrip (correct aspect ratio) as highlighted in (a) to demonstrate the stability of the configuration: (e) initial configuration after energy minimisation; (f) an external magnetic field $H = 0.25\,\mathrm{T}/\mu_0$ is applied in the $+y$ direction for 0.5 ns; (g) after removing the external field the system evolves freely and converges back to the initial state (snapshot after 5 ns). (e – g) show contour lines of the m_z component to improve visibility of the disturbance introduced by the external magnetic field. Bloch points are located at the small red and blue dots, the larger red circles show the additional antivortices.

4.8 Discussion

Our results show that two-layer FeGe nanostrips can host multiple Bloch points in any combination of head-to-head (HH) and tail-to-tail (TT). The Bloch-point configuration originates from vortices with identical circularity, but opposite polarisation, which are stabilised through the DMI of the material, which fixes the core orientation relative to circularity through the left- or right-handed chirality. The Bloch points form an interesting topological excitation in a helimagnetic system, which extends the set of well-known magnetic structures such as domain walls, vortices, and skyrmions. In the geometry described here, the Bloch points are in equilibrium and can be manipulated (e.g. with external magnetic fields).

We have found remarkable features of multiple interacting Bloch points in two-layer nanostrips. The two different types—head-to-head (HH) and tail-to-tail (TT)—can be geometrically arranged in any arbitrary order, and this magnetisation configuration resembles a meta-stable

configuration (within certain constraints on the strip width and length). The spatially averaged energy density for a system with n Bloch points increases in fixed steps. The number of steps scales linearly with the number of antivortices in the configuration (or equivalently: the number of neighbouring same-type Bloch points). We can determine an optimal Bloch-point spacing s_0 between Bloch points within a line of Bloch points (corresponding to a distance over which a Bloch point extends). Based on this optimal spacing, we can predict strip geometries suitable for an arbitrary number of Bloch points. We have verified this prediction by studying a system containing 80 Bloch points.

In the following, we speculate about possible future applications of Bloch points. One key-feature distinguishing Bloch points from many other particle-like magnetic configurations is the demonstrated coexistence of Bloch points of two different types in a single sample making Bloch points an interesting candidate for binary data representation. In the racetrack-like designs (Parkin et al., 2008; Sampaio et al., 2013), when realised with magnetic excitations of which only one type exists—such as skyrmions—we need to ensure that skyrmions keep their relative positions to be able to interpret the presence of a skyrmion as "1" and the absence of a skyrmion as "0". The two different types of Bloch points presented here could be used to encode binary data without the need to rely on fixed spacing of magnetic objects: a HH configuration could represent "1" and a TT configuration could represent "0". In the context of skyrmion-based realisation of the racetrack approach, other ideas to overcome the fixed-spacing requirement include the use of a combination of skyrmion tubes and chiral bobbers (Zheng et al., 2018) and the two-lane racetrack memory (Müller, 2017).

Chapter 5

Controlling stable Bloch points with electric currents

Preface

The work presented in this chapter has been published as Lang et al. (2023b). Compared to the publication, the discussion of uniform strips in Sec. 5.3 has been extended significantly in this thesis. All results from the publication can be reproduced from the accompanying repository (Lang et al., 2023c).

The finite-element simulations for the current density profile in non-rectangular nanostrips, Sec. 5.2.3, have been performed by Swapneel Amit Pathak.

5.1 Introduction

In this chapter, we study the motion of one or multiple stable Bloch points in the two-layer system consisting of layers with opposite material chirality under applied spin-transfer torque. In Sec. 5.2 we discuss the micromagnetic simulation procedure, the method used to locate individual Bloch points, and the finite-element simulations used to compute the current density profile in non-rectangular strips. For uniform nanostrips, we find that the Bloch point moves without any Hall effect in the two-layer geometry (Sec. 5.3.1). Multiple Bloch points move collectively, independent of their type or arrangement (Sec. 5.3.2), and we study in detail how the initial Bloch-point distance and their individual type affect details of the motion. Next, we study the effect of geometry variations of the nanostrip on the Bloch-point motion by removing the magnetic material in one or multiple notches at the edge of the nanostrip (Sec. 5.4 and Sec. 5.5). Finally, in Sec. 5.6, we simulate the motion of a Bloch point in a T-shaped geometry and show that we can control the trajectory of the Bloch point with the applied current. Depending on the current direction, the Bloch point can move along different paths, i.e. between arbitrary ends of the structure.

5.2 Methods

5.2.1 Micromagnetic simulation procedure

We simulate two-layer nanostrips with opposite chirality, i.e. opposite sign of the Dzyaloshinskii-Moriya constant D in the two layers. We fix the thickness of the two layers to $t_\mathrm{b} = 20\,\mathrm{nm}$ for the bottom layer and $t_\mathrm{t} = 10\,\mathrm{nm}$ for the top layer. We use a strip width of $w = 100\,\mathrm{nm}$ unless indicated differently. We choose strip lengths that allow for enough space for the Bloch points to move and vary the strip length depending on the number of Bloch points. We show the geometry in Fig. 5.1, the two layers are indicated with dark and light grey. The figure shows a nanostrip with an additional notch studied in Sec. 5.4. The top surface shows the corresponding simulated current density.

The energy equation

$$E = \int \mathrm{d}^3 r \, (w_\mathrm{ex} + w_\mathrm{dmi} + w_\mathrm{d}) \tag{5.1}$$

contains exchange energy density w_ex, bulk Dzyaloshinskii-Moriya energy density w_dmi, and demagnetisation energy density w_d. The magnetisation dynamics is simulated using the Landau-Lifshitz-Gilbert equation (Landau & Lifshitz, 1935; Gilbert, 2004) with currents modelled with the Zhang-Li model (Zhang & Li, 2004):

$$\frac{\partial \mathbf{m}}{\partial t} = -\gamma \mathbf{m} \times \mathbf{H}_\mathrm{eff} + \alpha \mathbf{m} \times \frac{\partial \mathbf{m}}{\partial t} - \mathbf{m} \times [\mathbf{m} \times (\mathbf{u} \cdot \nabla)\mathbf{m}] - \beta \mathbf{m} \times (\mathbf{u} \cdot \nabla)\mathbf{m}, \tag{5.2}$$

where $\gamma = 2.211 \times 10^5\,\mathrm{m/As}$ is the gyromagnetic ratio, α is the Gilbert damping, and

$$\mathbf{u} = \frac{P \mu_\mathrm{B} g}{2 e M_\mathrm{S} (1 + \beta^2)} \mathbf{j}_\mathrm{e} \tag{5.3}$$

is the spin-drift velocity. Here, $\mathbf{j}_\mathrm{e}$ is the electric current density, the vector points along the direction of the electron flow. P is the polarisation, μ_B the Bohr magneton, g the electron

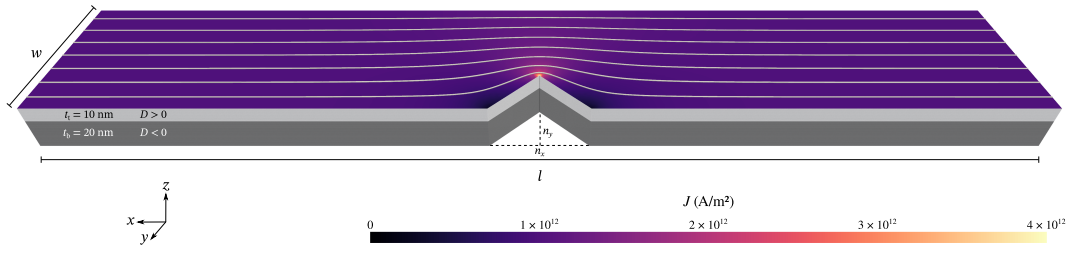

FIGURE 5.1: Geometry of the nanostrips studied in this work. All nanostrips consist of two layers with opposite chirality (light and dark grey), length l and width w are adjusted as required. In a later part of this chapter, we also study the effect of notches with width n_x and depth n_y in the strip. They extend throughout the whole sample thickness, as shown here. The colour and the streamlines on the top surface show the current density and direction in the nanostrip with a notch.

g-factor, e the elementary charge, and β the non-adiabatic parameter (see Sec. 2.5). Material parameters are based on FeGe (Beg et al., 2015): $A = 8.87\,\mathrm{pJ\,m^{-1}}$, $D = 1.58\,\mathrm{mJ\,m^{-2}}$, $M_\mathrm{s} = 384\,\mathrm{kA\,m^{-1}}$, and $\alpha = 0.28$ (Beg et al., 2017a). We use spatially varying current densities $\mathbf{J}$ of different magnitudes in our simulations and keep the other variables in Eq. 5.3 fixed to $P = 0.5$ and $\beta = 2\alpha = 0.56$.

All micromagnetic simulations are performed using Ubermag (Beg et al., 2022) with OOMMF (Donahue & Porter, 1999) as the computational backend and an extension for DMI for crystallographic point group T (Cortés-Ortuño et al., 2018b, 2018a). We have generalised the Zhang-Li OOMMF extension, in order to simulate current flowing in arbitrary directions. The modified extension is available on GitHub (Lang & Fangohr, 2023).

As a starting point for all simulations, we create rectangular nanostrips containing Bloch points at the desired positions, following the protocol that we developed for the study of multiple Bloch points (see Sec. 4.3). For rectangular nanostrips, we can then directly add the Zhang-Li term with a uniform current density to the dynamics equation and simulate the Bloch point dynamics. For more complex geometries, we first modify the nanostrip to have the desired shape and again minimise the energy to start from a relaxed configuration. Then, we add the Zhang-Li current using the current profile obtained form the finite-elements simulations outlined in Sec. 5.2.3.

5.2.2 Locating Bloch points

To analyse the Bloch-point motion we need to locate and track the individual Bloch points. We use a combination of two different methods to precisely locate the Bloch points. Tracking is then simply done based on the distance of Bloch points in consecutive time steps. In all simulations, the Bloch points are clearly separated and their number is kept fixed, hence identifying the individual Bloch points using this simple distance-based method is sufficient.

We first compute the approximate location of the Bloch points (within cell accuracy) based on the classification mechanism described in Sec. 4.5. We briefly summarise the method here. Bloch points can be identified as sources and sinks of the emergent magnetic field. To locate Bloch points along one direction, we compute the flux of the emergent magnetic field through a series of volumes that we increase along the respective direction. We find quantised jumps in the total flux whenever the volume includes an additional Bloch point. Based on the sign of the jump, we can determine the Bloch-point type. The approximate location of the Bloch point is given by the upper integration boundary. To locate a Bloch point in three dimensions, we can repeat this calculation along different directions, where we limit the integration volume along the directions where we have already located the Bloch point. That way we can locate individual Bloch points in a configuration containing multiple Bloch points.

To locate a Bloch point with sub cell-size accuracy, we can compute the centre of mass of the emergent magnetic field $\mathbf{B}^{\mathrm{e}}$ (Sec. 2.6), defined as:

$$\mathbf{r}_{\mathrm{BP}} = \frac{\int_V \mathrm{d}^3 r\, \mathbf{r}\, \mathrm{div}\, \mathbf{B}^{\mathrm{e}}}{\int_V \mathrm{d}^3 r\ \mathrm{div}\, \mathbf{B}^{\mathrm{e}}}. \tag{5.4}$$

This method only works if the considered volume contains a single Bloch point. Furthermore, magnetisation tilts at sample boundaries can affect the result. To get reliable results, we first compute the approximate location of all Bloch points. Then, we can compute the precise location of each Bloch point by only considering a small sub-volume V around the approximate position. In the majority of the work we only use the computationally less expensive locating method with cell-size accuracy.

5.2.3 Current profile

We use Python libraries, which are part of the FEniCSx project (Alnæs et al., 2014; Scroggs et al., 2022a, 2022b), to numerically compute the current profile in non-rectangular nanostrips. Additionally, we use Gmsh (Geuzaine & Remacle, 2009) to create the irregular mesh for the geometry.

For an electric conductor, according to Ohm's law, the electric current density $\mathbf{J}$ is defined via:

$$\mathbf{J} = \sigma \mathbf{E}, \tag{5.5}$$

where $\mathbf{E}$ is the electric field and σ the electric conductivity. Further, the principle of charge conservation yields:

$$\nabla \cdot \mathbf{J} = 0. \tag{5.6}$$

The electric current also induces an Oersted field, which is neglected in this work. According to Maxwell's equations, in the absence of a time varying magnetic field, the electric field is conservative. Hence, it can be expressed in terms of an electric potential as:

$$\mathbf{E} = -\nabla V. \tag{5.7}$$

Combining these equations, we obtain:

$$\nabla \cdot (-\sigma \nabla V) = 0. \tag{5.8}$$

Further, we assume as isotropic material, hence the conductivity is a scalar. This gives a Laplace's equation:

$$\nabla^2 V = 0, \tag{5.9}$$

which we can solve numerically after defining suitable boundary conditions.

Figure 5.1 shows an example for a rectangular nanostrip with a single notch. The calculated current density profile is shown on the top surface. We will discuss this geometry in detail in Sec. 5.4, where Fig. 5.8c shows a cut plane of the same geometry. We assume a constant current flow through the left and right sample boundary with strength J_0 in the $+x$ direction and no current flow through any of the other surfaces. Hence, the Neumann boundary conditions can be expressed as:

$$\frac{\partial V}{\partial n} = \begin{cases} -J_0/\sigma & \text{if } x = 0\,\text{nm} \\ J_0/\sigma & \text{if } x = 600\,\text{nm} \\ 0 & \text{else} \end{cases} . \tag{5.10}$$

In the example we use $J_0 = 10^{12}\,\text{A/m}^2$. The streamlines in Fig. 5.1 (and Fig. 5.8c) indicate the current direction, colour the magnitude of $\mathbf{J}$. We obtain a uniform flux in x direction in the rectangular parts of the nanostrip. Near the notch, the current profile changes as the current flows around the notch. This leads to a variation in the current density with the maximum at the tip of the notch. To include the current into the finite-difference micromagnetic simulations, we interpolate the simulated current profile onto a cuboidal mesh. Visualisations in Fig. 5.8 and Fig. 5.12 are shown on the finite-difference grid used for the micromagnetic simulations.

5.3 Uniform strips

5.3.1 One Bloch point

First, we focus on the motion of a single Bloch point in a uniform strip. We simulate rectangular nanostrips with length $l = 1500\,\text{nm}$ and width $w = 100\,\text{nm}$. We begin by relaxing the system into a state where it contains a single Bloch point near the left sample edge. Then, we apply current of different strengths in the $+x$ direction.

Figure 5.2 shows the m_z component of such a configuration at five different time steps for an applied current density $J_x = 0.7 \times 10^{12}\,\text{A/m}^2$. Initially, at $t = 0\,\text{ns}$, the Bloch point is located at $x_\text{i} \approx 150\,\text{nm}$ and is centred in the y direction (Fig. 5.2a). When current is applied, we can observe a motion of the Bloch point in the $+x$ direction. The Bloch point does not move in the y direction. Subfigures 5.2b to d show the magnetisation configuration at time steps $t = 5\,\text{ns}$ with the Bloch point located at $x \approx 510\,\text{nm}$, $t = 10\,\text{ns}$ with the Bloch point located at $x \approx 860\,\text{nm}$, and $t = 15\,\text{ns}$ with the Bloch point located at $x \approx 1200\,\text{nm}$. Figure 5.2e shows the configuration (with applied current) after the Bloch point reaches its final equilibrium position. The Bloch point is repelled from the sample edge and stops moving at a certain distance from the edge, which depends on the current strength. For $J_x = 0.7 \times 10^{12}\,\text{A/m}^2$ the final position is at $x_\text{f} \approx 1400\,\text{nm}$. Further applied current does not affect the Bloch point because edge repulsion and driving force are in equilibrium. The time step $t = 20\,\text{ns}$ in Fig. 5.2e shows the final equilibrium configuration several nanoseconds after the Bloch point reaches the right sample edge.

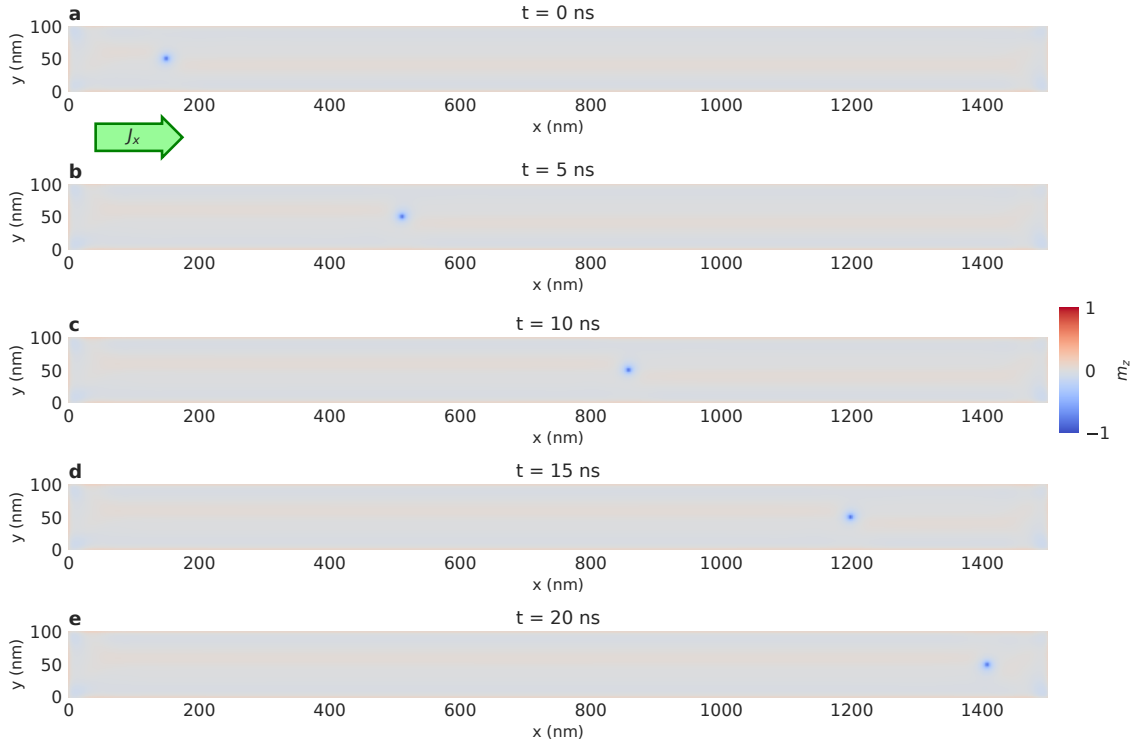

FIGURE 5.2: Movement of a single Bloch point with applied spin current with current density $J_x = 0.7 \times 10^{12}\,\mathrm{A/m^2}$. The Bloch point is initialised near the left sample edge (a). When applying current, the Bloch point moves in the $+x$ direction, parallel to the current, until it reaches the right sample edge (e). (b – d) show intermediate time steps.

Summarising these results, we can see that the Bloch point in the two-layer system moves parallel to the current direction without a Hall effect. We observe the same behaviour for other current densities above a depinning threshold (see below). We have verified these results for much wider strips ($w = 600\,\mathrm{nm}$) to ensure that the straight motion is not caused by the edge repulsion from the edges in the y direction in the narrow strip. Our results differ from the Bloch point in a chiral bobber studied by Gong et al. (2021), where the whole object shows a Hall effect that changes with the strength of the applied current. This difference can be understood from the two different system geometries. In the two-layer system studied here, the Bloch point is enclosed between two vortices located in the top and bottom layer. The vortices have opposite polarisation and hence would be subject to deflection in opposite direction. Overall, these effects cancel out and the Bloch point moves in a straight line. Similar suppression of the gyration has been observed for a Bloch point in a two-layer nanodisk, where the Bloch point is first displaced with an applied magnetic field and afterwards relaxes freely (Winkler et al., 2023).

We now study the effect of the current strength on the motion in more detail. Figure 5.3a shows the position of the Bloch point moving through the nanostrip for different applied current densities between $J_x = 0.07 \times 10^{12}\,\mathrm{A/m^2}$ and $J_x = 2.6 \times 10^{12}\,\mathrm{A/m^2}$ as a function of time.

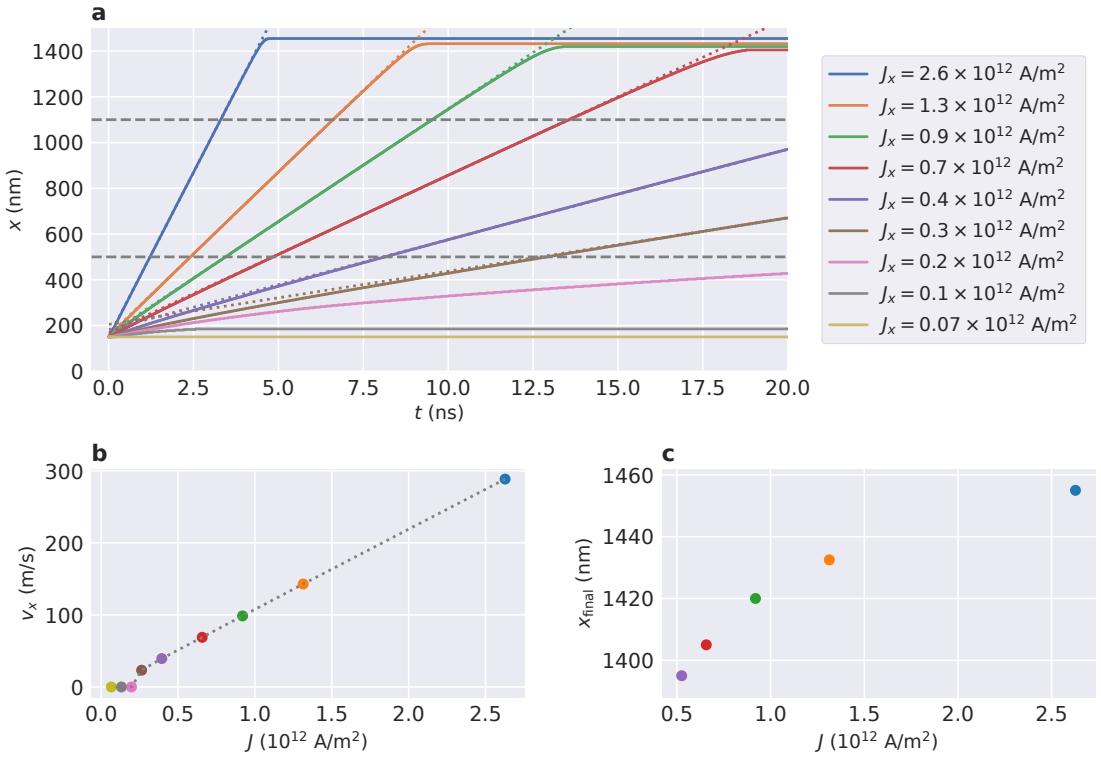

FIGURE 5.3: Movement of a single Bloch point with applied spin current. (a) Bloch-point position in x direction as a function of time for different current strengths. (b) Speed of the Bloch point depending on the current strength. A linear increase in speed can be observed above a certain depinning threshold. (c) Final equilibrium position of the Bloch point near the right sample edge at $x = 1500$ nm depending on the current density.

For large current densities ($J_x \geq 0.3 \times 10^{12}$ A/m^2 for the chosen discretisation size of 2.5 nm) we can see that the Bloch point moves through the nanostrip until it reaches the right sample edge (the simulation time of $t = 20$ ns shown in the figure is not long enough for Bloch points driven with $J_x \leq 0.4 \times 10^{12}$ A/m^2 to reach the right sample edge). In the inner part of the strip, away from the sample edges at $x = 0$ nm and $x = 1500$ nm, the Bloch point moves with constant velocity. We use the region between $x = 500$ nm and $x = 1100$ nm, highlighted with dashed lines, to compute the average velocity of the Bloch point using a linear fit. The thin dotted lines show the fits to the data. In the initial phase of the motion, after the onset of the current, we observe a non-linear motion of the Bloch point and a larger Bloch-point speed. During this initial phase, the whole micromagnetic structure re-adjusts to the current.

In the last part of the motion, the Bloch point reaches the right strip edge at $x = 1500$ nm. The Bloch point is repelled from the edge as can be seen from the plateaus in the Bloch-point position. The final position of the Bloch point as a function of current density is shown in Fig. 5.3c. Comparing the results for $J_x = 0.4 \times 10^{12}$ A/m^2 up to $J_x = 2.6 \times 10^{12}$ A/m^2, we can see that a larger current density pushes the Bloch point closer to the right sample edge, as can be expected. The current-dependence of this final position is a result of the varying total energy of the system depending on the Bloch-point position (see below).

For small current densities ($J_x = 0.07 \times 10^{12}\,\mathrm{A/m^2}$ in Fig. 5.3), we observe a pinning of the Bloch point in the discretisation lattice and hence no motion. The two simulations for $J_x = 0.1 \times 10^{12}\,\mathrm{A/m^2}$ and $J_x = 0.2 \times 10^{12}\,\mathrm{A/m^2}$ are special cases. Here, the current is not strong enough to permanently overcome the pinning in the discretisation potential and move the Bloch point through the whole nanostrip. However, the system has a comparatively high total energy in its initial configuration with the Bloch point near the sample edge at $x = 0\,\mathrm{nm}$ (see below). The combination of edge repulsion and applied current can overcome the pinning in the discretisation potential, and the Bloch point moves a limited distance until the edge repulsion becomes too weak and the Bloch point stops. We do not see any motion of the Bloch point for these current densities when starting from a state where the Bloch point is initially centred in x direction.

Pinning of the Bloch point in the inhomogeneous potential is a well-know property and can be observed in atomistic and micromagnetic simulations as described in Sec. 2.8.4. In micromagnetic simulations, the exact value of the depinning threshold density depends on the discretisation cell size. In the remainder of this work, we focus on larger current densities well above the depinning threshold.

Figure 5.3b shows the velocity v_x of the Bloch point in the x direction as a function of the current density. We can see the pinning for small current densities and then a linear increase in speed with increasing current density up to $v \approx 300\,\mathrm{m/s}$ for $J_x = 2.6 \times 10^{12}\,\mathrm{A/m^2}$. Simulations for larger current densities (not included in the figure) show that this linear increase in speed also holds for larger current densities. For very large current densities, probably not achievable in a real material, the current would lead to the creation and annihilation of additional Bloch points.

From the current-dependent stopping positions seen in Fig. 5.3 we can conclude that the total energy of the system depends on the position of the Bloch point in the nanostrip. We study this in more detail in a shorter strip with $l = 600\,\mathrm{nm}$. We initialise a Bloch point near the left sample edge and then drive the Bloch point with a current $J_x = 1.3 \times 10^{12}\,\mathrm{A/m^2}$ in the $+x$ direction (Fig. 5.4). The colour in Fig. 5.4a shows the m_z component of the initial configuration with the Bloch point at $x \approx 120\,\mathrm{nm}$. For each time step of the simulation, we then remove the external current and relax the system to obtain the energy of the equilibrium configuration depending on the Bloch-point position. Here, we exploit the pinning in the discretisation potential that generally prohibits motion of the Bloch point. The blue line in Fig. 5.4a shows the trajectory of the Bloch point with the applied current. The markers indicate the rightmost equilibrium positions of the Bloch point with applied current (blue diamond) and without applied current (orange square).

Figure 5.4b shows the position of the Bloch point in the x direction as a function of simulation time. The blue solid line shows the position with applied current, the orange dashed line the position after the free relaxation. We can distinguish two different regimes before and after $t = 2.5\,\mathrm{ns}$. In the first regime, the Bloch point is far away from the sample edge, and it does not

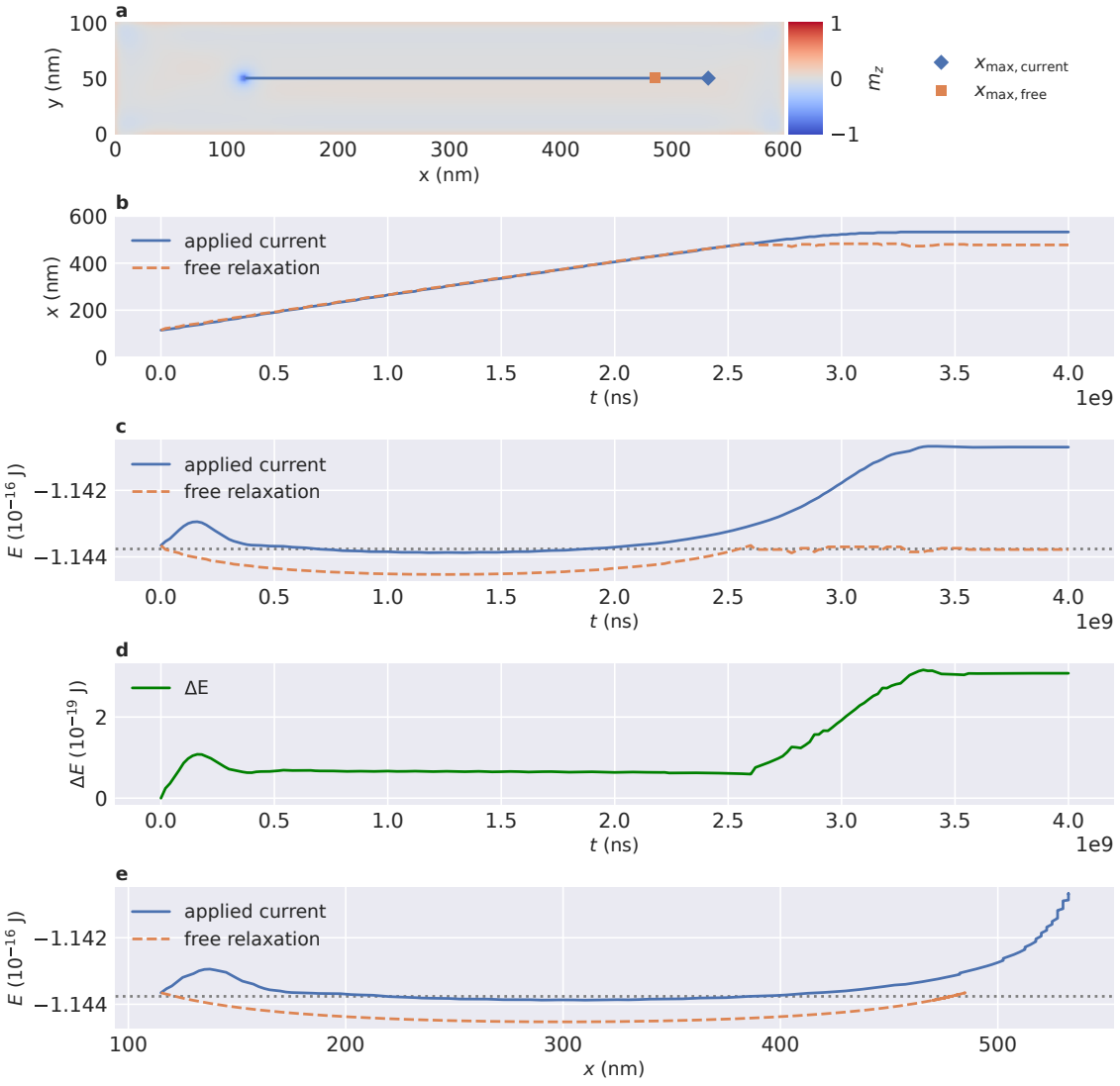

FIGURE 5.4: Influence of the Bloch-point position on the system's total energy for a nanostrip containing a single Bloch point. (a) System geometry, m_z component of the initial configuration, and trajectory of the Bloch point. The marker symbols indicate the rightmost equilibrium position of the Bloch point with applied current (blue diamond) and in the free system (orange square). (b) Position of the Bloch point in the x direction with applied current and after free relaxation as a function of simulation time. (c) Total energy of the system with applied current and after free relaxation and (d) energy difference between the configuration with and without applied current as a function of simulation time. (e) Total energy with and without current as a function of the Bloch-point position.

move when we remove the current and minimise the energy of the free system. In the second regime, after $t = 2.5\,\text{ns}$, the Bloch point comes close to the sample edge. With applied current, the final position is $x_{\text{current}} \approx 530\,\text{nm}$ (blue diamond in Fig. 5.4a). However, the Bloch point in the free system without applied current is not stable in this position. Instead, the Bloch point moves in the $-x$ direction, away from the sample edge at $x = 600\,\text{nm}$, during the relaxation and reaches a final position of $x_{\text{free}} \approx 480\,\text{nm}$ (orange square in Fig. 5.4a).

These differences are a result of the change in total energy depending on the Bloch-point position. Figure 5.4c shows the total energy for the system with applied current (blue solid line) and after free relaxation (orange dashed line) as a function of simulation time, and Fig. 5.4d shows the difference of the two energies. Figure 5.4e shows the two energies as a function of Bloch-point position. We can see that the total energy has a minimum when the Bloch point is located in the centre of the strip at $x = 300\,\text{nm}$ in Fig. 5.4e (and at $t \approx 1.3\,\text{ns}$ in Fig. 5.4c) and monotonically increases when the Bloch point moves closer to the sample boundary. With applied current, the whole configuration is in an excited state and has a higher total energy. When the Bloch point is far enough away from the sample edges in the x direction, in the simulation between $t \approx 0.4\,\text{ns}$ and $t \approx 2.6\,\text{ns}$, we can see a constant energy difference ΔE (Fig. 5.4d). After $t \approx 2.6\,\text{ns}$, the two energies deviate. With applied current, the total energy increases further up to $t \approx 3.4\,\text{ns}$. During this part of the simulation, the Bloch point still moves closer to the boundary. For $t > 3.4\,\text{ns}$ the Bloch point stops moving and hence the energy stays constant. In the free system, the total energy stays approximately constant for $t > 2.5\,\text{ns}$ and the Bloch point moves away from the sample edge during the free relaxation. These differences are caused by the pinning in the lattice potential, which is not strong enough to compensate the increase in total energy for $x > 480\,\text{nm}$ ($t > 2.6\,\text{ns}$) when the Bloch point comes close to the sample edge at $x = 600\,\text{nm}$.

In Fig. 5.4c to e we can see additional deviations in the initial phase of the simulations, for $t < 0.4\,\text{ns}$. At $t = 0\,\text{ns}$ the configuration is still in its equilibrium state and both energies are identical. When we start to apply current, the configuration re-adjusts, including a small motion of the Bloch point in the $+x$ direction, to compensate the adiabatic component of the spin current (the Bloch point does not reach a state of steady motion when we set the non-adiabatic parameter to $\beta = 0$). This deformation of the magnetisation configuration leads to an additional contribution to the total energy for $t < 0.4\,\text{ns}$.

5.3.2 Multiple Bloch points

Next, we discuss driving multiple Bloch points. We limit this discussion to three different configurations containing two Bloch points. Figure 5.5 shows the m_z component of the initial configuration (left part) and final configuration (right part) for the three systems: two Bloch points of the same type (head-to-head and head-to-head with an antivortex in between) with an initial distance $d_{\text{i,a}} \approx 250\,\text{nm}$ of the Bloch points and the antivortex centred between the two Bloch points (Fig. 5.5a), two Bloch points of opposite type (tail-to-tail and head-to-head)

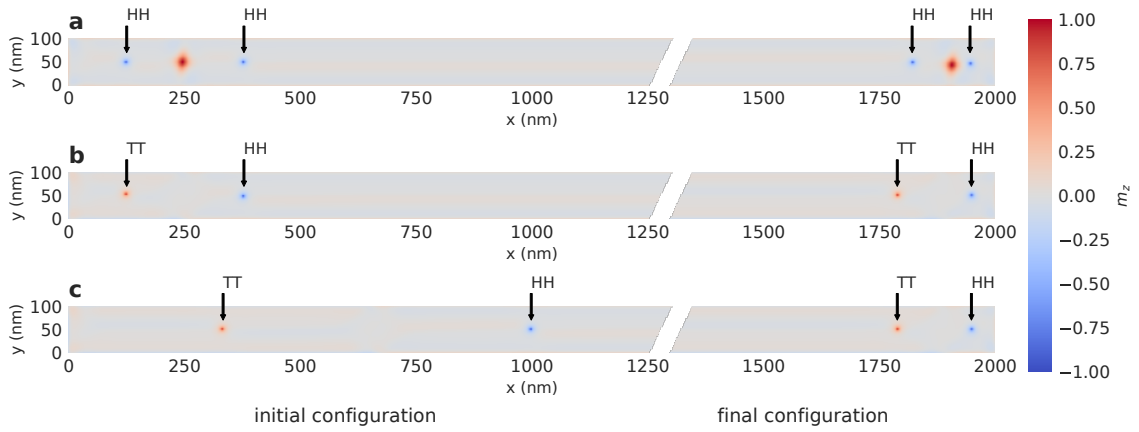

FIGURE 5.5: Initial configuration (left part) and final configuration (right part) of systems containing two Bloch points that are driven with a spin current. (a) Bloch points in the configuration head-to-head and head-to-head with an antivortex in between; (b) Bloch points in the configuration tail-to-tail and head-to-head with small initial distance; (c) Bloch points in the configuration tail-to-tail and head-to-head with large initial distance.

with an initial distance $d_{\mathrm{i,b}} \approx 250\,\mathrm{nm}$ (Fig. 5.5b), and two Bloch points of opposite type (tail-to-tail and head-to-head) with an initial distance $d_{\mathrm{i,c}} \approx 665\,\mathrm{nm}$ (Fig. 5.5c). We will refer to these configurations as *a*, *b*, and *c*. We apply a uniform current with $J_x = 0.7 \times 10^{12}\,\mathrm{A/m^2}$ in the $+x$ direction for all three simulations. The simulations start from relaxed states with no applied current, and the Bloch points are at rest at $t = 0$. The current is applied for the whole simulation time.

We can see that the Bloch points and the antivortex collectively move in current direction (right part in Fig. 5.5). The Bloch-point type does not affect the direction of motion. The right (head-to-head) Bloch point reaches nearly the same position in all three simulations. The final distance of the Bloch points depends on their individual type and the applied current, but it is independent of their initial distance. For the same-type Bloch points (configuration *a*) we find a final distance $d_{\mathrm{f,a}} \approx 125\,\mathrm{nm}$. The antivortex is located closer to the right Bloch point (distance 40 nm). For the two configurations containing Bloch points of opposite type (configurations *b* and *c*) we obtain the same final distance $d_{\mathrm{f,b}} = d_{\mathrm{f,c}} \approx 160\,\mathrm{nm}$, independent of their initial distance. The final distance is a result of the competition between Bloch point-Bloch point repulsion and the torque exerted from the driving current. We can see that the antivortex in between same-type Bloch points seems to reduce the Bloch point-Bloch point repulsion and allows for a smaller final distance.

Figures 5.6 and 5.7 (discussed in detail in the following) show the position x, velocity v_x, and distance d_x of the Bloch points and the antivortex for the three configuration as a function of simulation time. The time-resolved data reveals the influence of initial position, initial distance, and configuration on the motion of the Bloch points. For reference, we also include data for a system containing a single Bloch point.

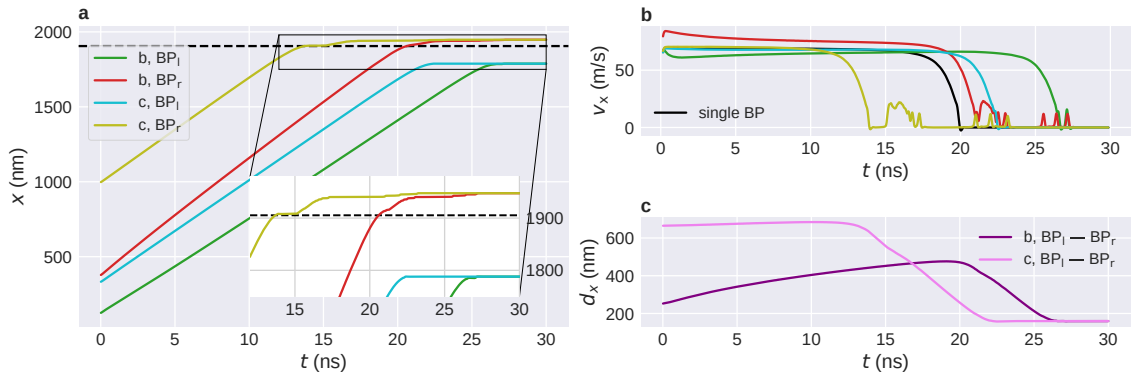

FIGURE 5.6: Motion of two Bloch points in the configurations *b* and *c* from Fig. 5.5. (a) Position of the Bloch points as a function of simulation time. The subscripts l and r refer to the left and right Bloch point of the configuration. The dashed line indicates the final equilibrium position of a single Bloch point. (b) Velocity v_x of the individual Bloch points in the configurations *b* and *c*, and for a system containing a single Bloch point. (c) Distance between the two Bloch points as a function of time.

First, we focus on configurations *b* and *c*, containing Bloch points of opposite type with different initial distance (Fig. 5.5b and Fig. 5.5c). Figure 5.6a shows the position of the Bloch points in x direction, Fig. 5.6b the velocity v_x of the Bloch points, and Fig. 5.6c the distance d_x between the Bloch points. Additionally, Fig. 5.6a indicates the final equilibrium position of a configuration containing a single Bloch point (dashed line) and Fig. 5.6b shows velocity data for the single Bloch point.

The pinning in the discretisation potential results in a non-uniform velocity with high-frequency oscillations, which depend on the discretisation cell size. We smooth the velocities using two consecutive rolling averages over 15 time steps (0.15 ns) with the window centred on the current data point, first with a Gaussian profile with standard deviation 4, second with even weights. As a sanity check, we integrate the smoothed velocity to confirm that the total travelled distance obtained from the integration matches the distance that the Bloch points have actually travelled (based on the position data). As a side effect of this averaging, we do not have velocity data for $t < 0.14$ ns and hence cannot study details of the onset of the motion.

For Bloch points with large initial distance (configuration *c*), we can see that both Bloch points move with nearly the same velocity (Fig. 5.6b), which is comparable to that of a single Bloch point. Accordingly, the distance between the Bloch points stays almost constant as long as both Bloch points can move freely (Fig. 5.6c, $t < 12$ ns). For the right Bloch point we observe a slowdown as it approaches the right sample edge at $t \approx 12$ ns, and the motion stops at $t \approx 14$ ns, when the Bloch point reaches the equilibrium position of the single Bloch point. The second Bloch point continues moving towards the right and also affects the right Bloch point, which in turn moves closer towards the right sample edge between $t \approx 15$ ns and $t \approx 17$ ns. Afterwards, we can observe a slip-stick motion with a few additional spikes in the velocity (Fig. 5.6b, broadened due to the smoothing of the velocity data) as the Bloch point moves a few cells closer to the right sample edge. The left Bloch point reaches its final

position at $t \approx 22\,\mathrm{ns}$. We do not observe a decrease in velocity for the second Bloch point as the distance between the two Bloch points decreases (excluding the part for $t > 20\,\mathrm{ns}$ where the Bloch point reaches its final equilibrium position), which also manifests in a linear decrease of the Bloch-point distance (Fig 5.6c, $14\,\mathrm{ns} < t < 22\,\mathrm{ns}$).

For Bloch points with smaller initial distance (configuration *b*), we observe qualitatively similar behaviour with some differences in the details of the motion. We first focus on the time between $t \approx 1\,\mathrm{ns}$ and $t \approx 20\,\mathrm{ns}$. During this time frame, both Bloch points move towards the right and their motion is only affected by their mutual interaction. In Fig. 5.6b, we can observe an increased velocity of the right Bloch point and a decreased velocity of the left Bloch point compared to the results for a single Bloch point (and the two Bloch points with large initial distance). This also manifests in an increase of the Bloch-point distance over time in Fig. 5.6c. With increasing distance, the repulsion becomes weaker and the velocity difference decreases.

In the initial phase of the motion, roughly up to $t = 1\,\mathrm{ns}$, we can see a larger initial velocity and then a significant velocity decrease in Fig. 5.6b. This feature is more prominent for the left Bloch point and results from the edge repulsion of the Bloch points. It is a consequence of the initial configuration with the Bloch points close to the sample edge at $x = 0\,\mathrm{nm}$. It does not occur for Bloch points initialised further away from the sample edge, as can be seen for configuration *c*.

At $t \approx 27\,\mathrm{ns}$, the right Bloch point in configuration *b* reaches its final equilibrium position near the right sample edge and stops moving. Its final position is identical to that of the right Bloch point in configuration *c*. Before reaching this position, we can observe a slow-down at $t \approx 20\,\mathrm{ns}$, when the Bloch point passes the equilibrium position of a single Bloch point (without stopping completely), and a slip-stick motion for $t > 23\,\mathrm{ns}$, similar to the right Bloch point in configuration *c*. The left Bloch point in configuration *b* reaches its final position at $t \approx 26\,\mathrm{ns}$. Again, the final position is identical to that of the left Bloch point in configuration *c*. In the time frame between $t \approx 20\,\mathrm{ns}$ and $t \approx 26\,\mathrm{ns}$ we observe a linear decrease of the Bloch-point distance (Fig. 5.6c) without any significant speed reduction for the left Bloch point.

Figure 5.7 compares the results for configuration *a* (containing two Bloch points of the same type, Fig. 5.5a) and configuration *b* (containing two Bloch points of opposite type, Fig. 5.5b). The Bloch points in both systems are initialised at the same positions, close to the left sample edge. We have already discussed the details of the Bloch-point motion for configuration *b* in the previous paragraphs. We find qualitatively similar behaviour for configuration *a*. The presence of the additional antivortex changes some details of the motion.

In the direct comparison in Fig. 5.7b we can see that the speed of the right Bloch point in configuration *a* is higher and the speed of the left Bloch point in configuration *a* is lower that those of the respective Bloch points in configuration *b*. This results in a faster increase of the distance between the two Bloch points and a larger maximum distance at $t \approx 19\,\mathrm{ns}$ (Fig. 5.7c). In contrast, the final Bloch-point distance after both Bloch points have reached their equilibrium position near the right sample edge is smaller in configuration *a*.

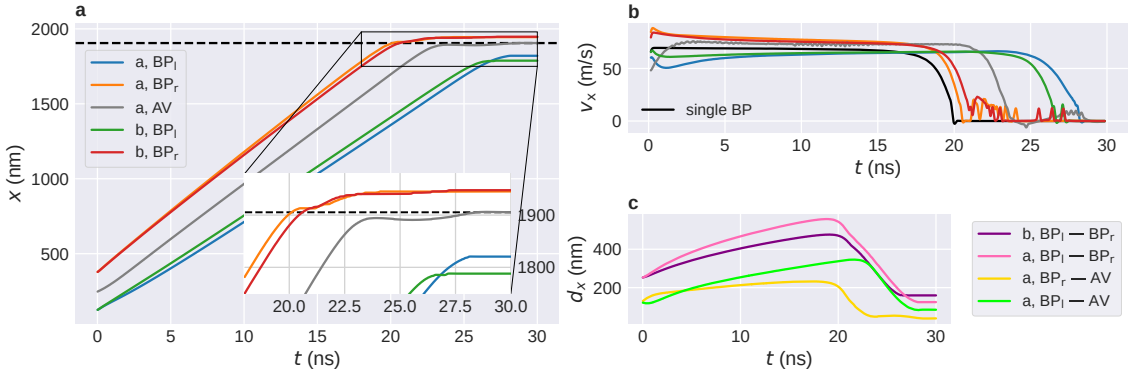

FIGURE 5.7: Motion of two Bloch points in the configurations *a* and *b* from Fig. 5.5. (a) Position of the Bloch points and the antivortex as a function of simulation time. The subscripts l and r refer to the left and right Bloch point of the configuration. The dashed line indicates the final equilibrium position of a single Bloch point. (b) Velocity v_x of the individual Bloch points and the antivortex in the configurations *a* and *b*, and for a system containing a single Bloch point. (c) Distance between the two Bloch points and between the antivortex and each of the two Bloch points in configuration *a* as a function of time.

Both observations can be attributed to the presence of the additional antivortex between the two same-type Bloch points in configuration *a*. The speed of the antivortex is larger than that of a single Bloch point (Fig. 5.7b). This could be a consequence of the additional pinning force for a Bloch point, which is absent for the antivortex, or indicate a more effective coupling of the spin-transfer torque to the antivortex. The higher antivortex velocity together with the repulsion between the antivortex and the Bloch points and the small initial distance of the Bloch points leads to an increased velocity of the right Bloch point and a decreased velocity of the left Bloch point in configuration *a*.

Figure 5.7c also shows the distance between the antivortex and each of the two Bloch points and provides further insights. At $t = 0$ ns, the antivortex is centred between the two Bloch points. The distance between the left Bloch point and the antivortex stays nearly constant up to $t \approx 1$ ns, whereas the distance between the antivortex and the right Bloch point increases rapidly during this time period. This is presumably a result of the edge repulsion of the Bloch points that leads to a large initial Bloch-point velocity, whereas we observe a much slower acceleration for the antivortex, which reaches a mostly steady velocity only after $t \approx 2$ ns. After this initial phase, we observe an increase of both distances, with a larger slope for the distance between the left Bloch point and the antivortex due to the higher antivortex velocity. The antivortex pushes the right Bloch point, which therefore has a higher velocity in configuration *a* compared to configuration *b*. Furthermore, the left Bloch point is slowed down due to the overall small distance to the antivortex. Once the Bloch points and the antivortex reach their respective final equilibrium positions near the right sample edge, they stop moving and the distances decrease. For the right Bloch point we additionally see a slowdown at the equilibrium position of a single Bloch point at $t \approx 20$ ns and a slip-stick motion near the sample edge, as seen before.

In the final equilibrium configuration, for $t > 28$ ns, we find that the antivortex is much closer to the right Bloch point than to the left Bloch point (Fig. 5.7c and also Fig. 5.5a, right). We obtain $d_x \approx 40$ nm between the antivortex and the right Bloch point and $d_x \approx 85$ nm between the antivortex and the left Bloch point.

The different distances could indicate that the coupling of the spin-transfer torque to an antivortex is more effective than the coupling to a Bloch point. When the antivortex is pushed towards the right Bloch point in front of it (which has a fixed position do to the edge repulsion), it reaches a final distance $d_x \approx 40$ nm. In contrast, when the left Bloch point is pushed towards the antivortex, the minimum achievable distance is $d_x \approx 85$ nm, about twice as much as in the opposite case. Hence, the force pushing the antivortex towards the Bloch point seems to be stronger that the force pushing the Bloch point towards the antivortex. The final distance between the antivortex and the right Bloch point is additionally decreased due the presence of the left Bloch point, as can be seen from the motion of the antivortex between $t \approx 23$ ns and $t \approx 28$ ns (Fig. 5.7a). After coming close to the right Bloch point, the antivortex first moves in the $-x$ direction, away from the right Bloch point, and then again in the $+x$ direction when the left Bloch point comes closer. However, the effect of the left Bloch point does not seem to be strong enough to explain the difference of factor two of the two distances. We have carried out additional simulations where we only move the antivortex or Bloch point and keep the other object fixed (by fixing the magnetisation of a few cells in the simulation). Here, we find a minimum distance $d_x \approx 55$ nm and final equilibrium distance $d_x \approx 65$ nm when moving the antivortex towards the fixed Bloch point and a minimum (final) distance $d_x \approx 85$ nm when moving the Bloch point towards the fixed antivortex. We can conclude that the presence of the left Bloch point in configuration a leads to a reduction of the distance between the antivortex and the right Bloch point between $\Delta d_x \approx 15$ nm and $\Delta d_x \approx 25$ nm.

Let us briefly summarise these results. We have found that multiple Bloch points in a sample collectively move under applied current. Bloch points repel each other and are repelled from the sample edges and additional vortices present in the configuration. These repulsions can affect the speed of the Bloch points and prevent Bloch points from leaving the sample. Antivortices have a higher velocity and push Bloch points in front of them.

5.4 Nanostrip with one notch

Next, we study the motion of a single Bloch point in a nanostrip with a notch. We simulate a strip with $l = 600$ nm with a wedge-shaped notch at $x = 300$ nm, extending through the sample in z direction (Fig. 5.1). The notch tip is located at $y = 70$ nm ($n_y = 30$ nm) and the opening angle is 90° ($n_x = 60$ nm). An xy cross-section is shown in Fig. 5.8. We use a finite-element simulation to compute the non-uniform current density profile in this geometry, as discussed in Sec. 5.2.3. The resulting current profile is shown in Fig. 5.8c. Near the notch we can observe a variation in the current density with the maximum at the tip of the notch.

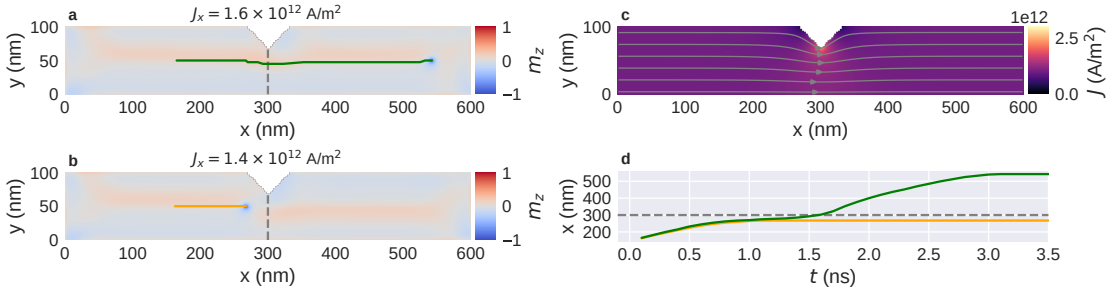

FIGURE 5.8: Motion of a Bloch point in a nanostrip ($l = 600$ nm, $w = 100$ nm) with a single notch under applied current. (a, b) Final configuration and Bloch-point trajectory for two different current strengths: (a) the Bloch point can move past the notch for $J_x = 1.6 \times 10^{12}$ A/m^2; (b) the Bloch point is trapped at the notch for $J_x = 1.4 \times 10^{12}$ A/m^2. (c) Simulated current profile. (d) Position of the Bloch points in (a) and (b) as a function of simulation time.

The simulated current densities on the order of 10^{12} A/m^2 would lead to a significant temperature increase due to Joule heating. A detailed study (Fangohr et al., 2011) shows that the material, pulse duration, and cooling from the substrate play important roles in the control of the temperature. In this prototype study we ignore all temperature-related effects and possible engineering efforts which would need to be addressed for higher technical readiness levels.

First, we focus on two current densities $J_{x,\mathrm{a}} = 1.6 \times 10^{12}$ A/m^2 and $J_{x,\mathrm{b}} = 1.4 \times 10^{12}$ A/m^2. We initialise the systems with a Bloch point at $x_\mathrm{i} \approx 165$ nm. The final configurations with applied current are shown in Fig. 5.8a and b for $J_{x,\mathrm{a}}$ and $J_{x,\mathrm{b}}$, respectively. The solid lines show the Bloch-point path from its initial to its final configuration. Figure 5.8d shows the x position of the Bloch point in the two simulations as a function of simulation time.

The current density $J_{x,\mathrm{b}}$ (Fig. 5.8b) is not strong enough to push the Bloch point past the notch. Instead, the Bloch point gets stuck near the notch at a final position $x_{\mathrm{f,b}} \approx 270$ nm, to which it moves in a straight line without any deflection in y direction. As a function of time (Fig. 5.8d), we can see a slow-down as the Bloch point approaches the notch. The motion stops around $t = 1$ ns: the applied current cannot push the Bloch point further against the restoring force from the notch constriction.

The current density $J_{x,\mathrm{a}}$ (Fig. 5.8a) is strong enough to push the Bloch point past the notch, and the Bloch point stops at $x_{\mathrm{f,a}} \approx 550$ nm at around $t = 3$ ns due to the edge repulsion of the sample at $x = 600$ nm. Near the notch, we can see a small displacement in the $-y$ direction, away from the tip of the notch. In the time-resolved data (Fig. 5.8d), we can see a slow-down of the Bloch point in front of the notch, very similar to the results for $J_{x,\mathrm{a}}$ up to $t \approx 1$ ns. The small deviations of the two curves for Bloch-point positions before the notch are caused by the slightly different current strengths. However, for the stronger current, the Bloch point continues to move towards the notch for $t > 1$ ns. We can see a slight speed increase around $t = 1.3$ ns, and the Bloch point passes the tip of the notch at around $t = 1.6$ ns (and $x = 300$ nm shown as a dashed line in Fig. 5.8). After passing the notch, we can see a strong speed increase

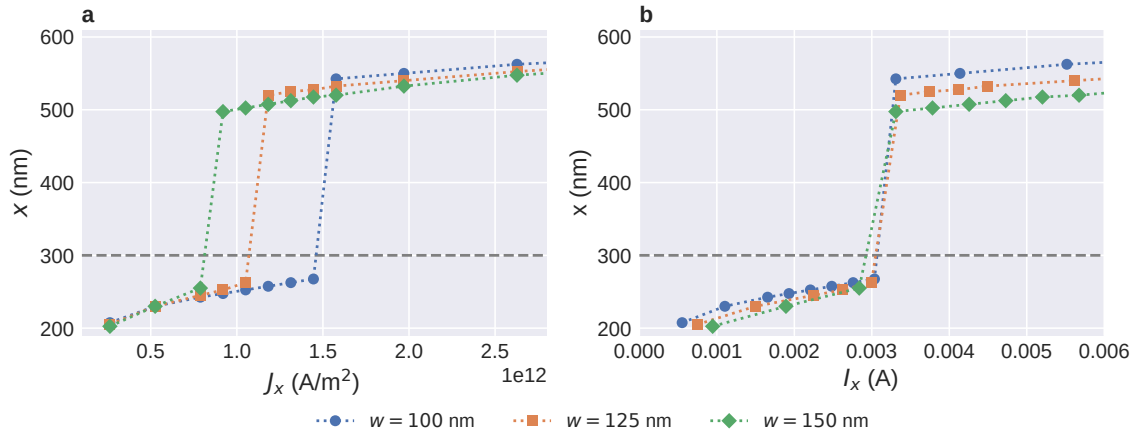

FIGURE 5.9: Final equilibrium position of a Bloch point in a strip with a notch as a function of applied current for three different strip widths. (a) The minimum required current density to move the Bloch point past the notch at $x = 300\,\text{nm}$ increases with decreasing strip width. (b) The Bloch point moves past the notch at a critical total current that is independent of the details of the geometry. In both subfigures, we can see that narrower strips compress the overall structure and allow the Bloch point to move closer to the notch or sample edge.

and a fast motion in $+x$ direction until the Bloch point approaches the right sample boundary, where it slows down and eventually stops.

To better understand the effect of the notch size on the pinning, we simulate strips with three different widths $w = 100\,\text{nm}$, $w = 125\,\text{nm}$, and $w = 150\,\text{nm}$ for several different current densities. We keep the notch size of $n_y = 30\,\text{nm}$ used before. Results are shown in Fig. 5.9.

Figure 5.9a shows the final position of the Bloch point as a function of current density. Final positions below the notch tip at $x = 300\,\text{nm}$, visualised by the grey dashed line, mean that the Bloch point cannot move past the notch. Larger final positions mean that the Bloch point moves past the notch. We can see that the minimum current density required to move the Bloch point past the notch increases with decreasing strip width, as can be expected because the fraction by which the overall structure with the embedded Bloch point has to be compressed increases with decreasing strip width.

For large current densities, $J_x \geq 1.6 \times 10^{12}\,\text{A/m}^2$, the Bloch point moves past the notch for all strip widths. Here, we can see that the Bloch point can move closer to the right sample boundary when the strip width decreases. This is presumably a result of the fact that the large-scale magnetisation configuration around the Bloch point is more compressed in narrower strips. It is in agreement with our previous work (Lang et al., 2023a), discussed in Chap. 4, where we find that the optimal distance between Bloch points in a configuration containing multiple Bloch points also decreases with decreasing strip width. It appears that the large-scale configuration around the Bloch point wants to retain its approximately circular shape and reduces its radius due to the narrowness (in y direction) of the strip.

Figure 5.9b shows the final position as a function of total current through the yz plane at the notch tip, the minimum of the constriction. For similar geometries studied here, i.e. always a notch of the same size at the same x position, we find that the total current required to move the Bloch point past the notch is approximately independent of the strip width.

5.5 Nanostrip with multiple notches

Based on the previous results, we can develop a protocol to move one or multiple Bloch points past a series of notches in a controlled manner. The overall idea is as follows. For weak current strengths, the Bloch point cannot move past a notch. Hence, we can use a weak current to move a Bloch point to a defined position close to a notch. Subsequently, we can apply a short, strong current pulse that pushes the Bloch point past the notch. Afterwards, we can let the system relax (i.e. switch off the current) or use a weak current to move the Bloch point to the next notch.

Figure 5.10 demonstrates this process for a single Bloch point in a strip with length $l = 1000\,\text{nm}$ and four notches at $x = 200\,\text{nm}$, $x = 400\,\text{nm}$, $x = 600\,\text{nm}$, and $x = 800\,\text{nm}$. We initialise the system in a configuration containing a single Bloch point between the first two notches at $x = 300\,\text{nm}$. Figure 5.10a shows the strip geometry and the path of the Bloch point, Fig. 5.10b shows the x position of the Bloch point as a function of simulation time t.

We use a three-step process to move the Bloch point past a notch. (i) We apply a current $J_{x,(\text{i})} = 0.7\times10^{12}\,\text{A/m}^2$ to move the Bloch point to the next notch, where it gets trapped. We use

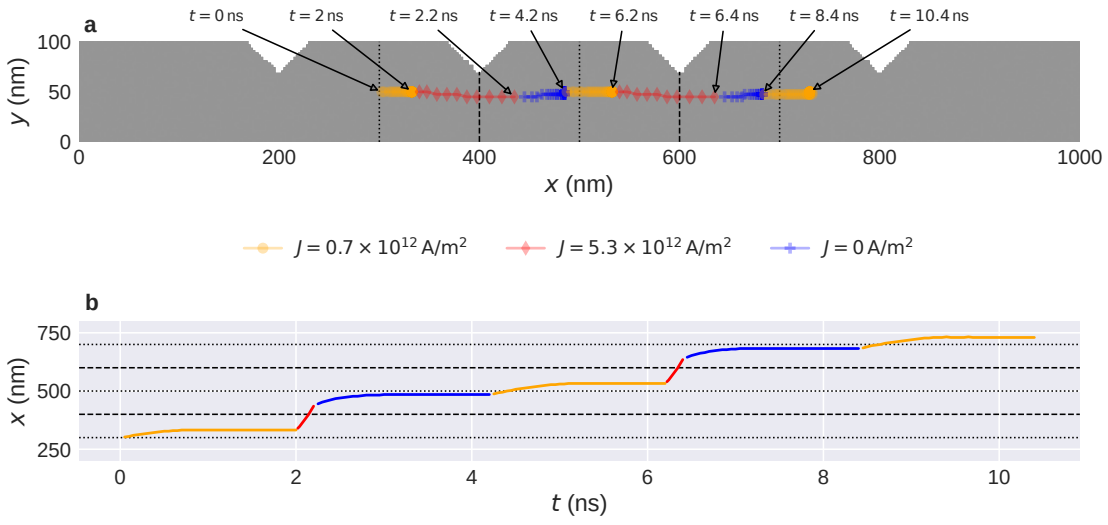

FIGURE 5.10: Driving a single Bloch point past several notches using a series of current pulses of different strength. (a) Strip geometry and trajectory of the Bloch point. (b) Position of the Bloch point in x direction as a function of simulation time. Dashed and dotted lines indicate the locations of the notches and centres of the wide areas in between, respectively.

a pulse length $\Delta t_{(\mathrm{i})} = 2\,\mathrm{ns}$ for this alignment of the Bloch point to the left of the notch. From the time-resolved data we can see that the Bloch point stops moving after $\Delta t \approx 0.5\,\mathrm{ns}$. The longer pulse duration can be useful to ensure that the Bloch point reaches the notch independent of its initial position. Applying the pulse for "too long" does not affect the configuration due to the trapping at the notch. (ii) We apply a strong pulse with $J_{x,(\mathrm{ii})} = 5.3 \times 10^{12}\,\mathrm{A/m^2}$ with pulse length $\Delta t_{(\mathrm{ii})} = 0.2\,\mathrm{ns}$. This pulse pushes the Bloch point past the notch. A short pulse duration is required to ensure that the Bloch point only moves past one notch. (iii) We remove the current and let the system relax for $\Delta t_{(\mathrm{iii})} = 2\,\mathrm{ns}$. During this period, the Bloch point moves away from the notch until it reaches its equilibrium position near the centre of the region between the two notches, hereinafter called storage area. In the simulation, the Bloch point reaches its equilibrium position after $\Delta t \approx 0.5\,\mathrm{ns}$ and does not move for the remainder of $\Delta t_{(\mathrm{iii})}$.

We can repeat steps (i) to (iii) to move the Bloch point past a series of notches, as shown in Fig. 5.10. Step (iii) is not strictly required to achieve the desired motion past multiple notches. However, it demonstrates several advantages. First, the Bloch point in the free system reaches an equilibrium position in each storage area without an applied current. Hence, successful operation only requires an applied current during a short period of time. This reduces energy consumption of potential devices based on this technology as external energy is only required to change the configuration. Second, the position of the Bloch point at the end of step (ii) is not critical. As long as the Bloch point has moved past the notch, the configuration will automatically converge to a low-energy state with the Bloch point in the desired storage area. This makes the approach more robust and less sensitive to, for example, variations in current pulse duration and notch geometry.

Figure 5.11 demonstrates a similar process for a configuration containing multiple Bloch points in the configuration HH-HH-TT-TT-HH (following the notation introduced in Chap. 4). We simulate a strip with length $l = 1600\,\mathrm{nm}$ containing seven notches. Figure 5.11a shows the initial configuration with the individual Bloch points labelled.

The two large red and blue blobs at $x \approx 300\,\mathrm{nm}$ and $x \approx 800\,\mathrm{nm}$ are antivortices that form between neighbouring Bloch points of the same type and which have significant magnetisation in the z direction. We have discussed their role in the motion of Bloch points in Sec. 5.3.2. For the following discussion, it is sufficient to focus on the Bloch points.

To simplify the simulation process, we only use steps (i) with $\Delta t_{(\mathrm{i})} = 5\,\mathrm{ns}$ and (ii) with $\Delta t_{(\mathrm{ii})} = 0.25\,\mathrm{ns}$. We start with (i) a weak current that moves the Bloch points towards the notches where they get trapped to the left of each notch (Fig. 5.11b). The antivortices experience a repelling force from the Bloch points but do not significantly interact with the notches. Subsequently, we apply (ii) the strong current pulse that pushes each of the Bloch points past the next notch to their right (Fig. 5.11c). In the configuration at the end of this pulse, at $t = 5.25\,\mathrm{ns}$, we can see that individual Bloch points have travelled different distances during the pulse. After the next weak pulse (Fig. 5.11d) each of the Bloch points is aligned to the left

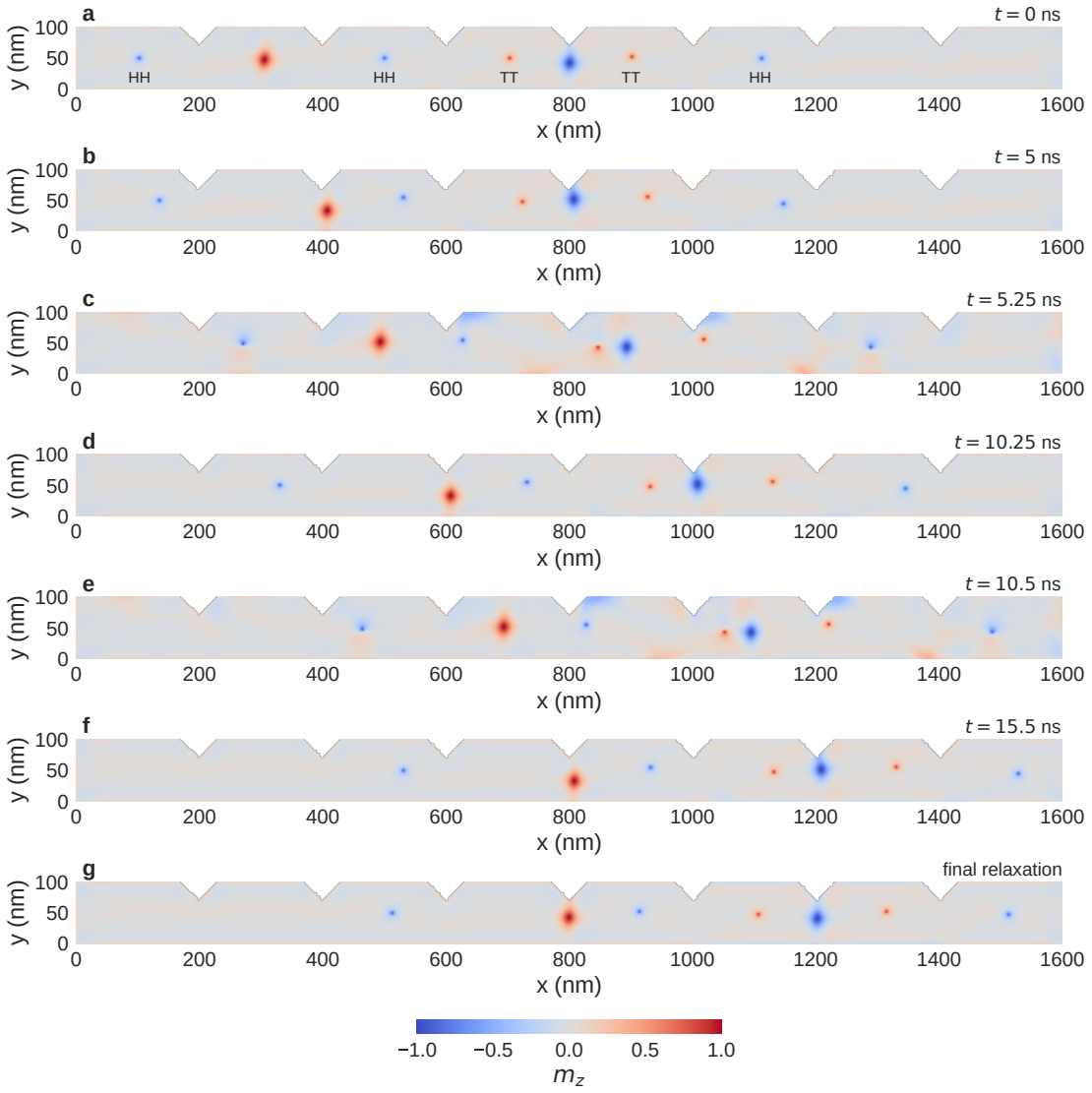

FIGURE 5.11: Movement of a configuration containing five Bloch points past two notches by applying a series of current pulses of alternating lower and higher strength. The initial configuration and the distribution of the Bloch points across storage areas is retained.

of the next notch, and all Bloch points have the same spacing to their notch. By applying the weak pulse for a sufficiently long period, we ensure that all Bloch points reach their aligned position near the next notch before applying the next strong pulse. The cycle is repeated once more (Fig. 5.11e and Fig. 5.11f), and we can see, at $t = 15.5$ ns, that each Bloch point has moved one notch further (in comparison to Fig. 5.11d) in the direction of the applied current.

To demonstrate the stability of the free configuration, we also simulate the free relaxation after the last current pulse. Figure 5.11g shows the relaxed configuration. We can see that the configuration does not significantly change from the previous step (Fig. 5.11f), but we observe small shifts of the Bloch points in the $-x$ direction due to the repulsion from the notches and the sample edge.

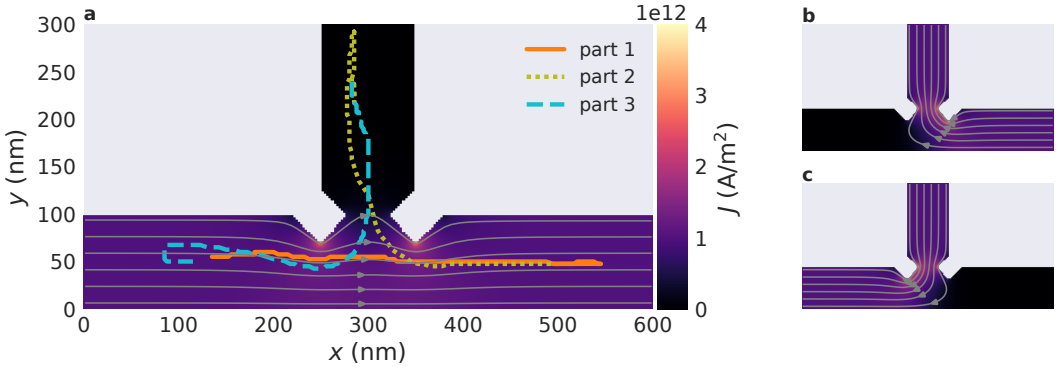

FIGURE 5.12: Movement of a single Bloch point through a T-shaped structure when applying a series of current pulses along different directions. The Bloch point is initialised in the left storage area, its position during the simulation is shown with the thick line in (a). The Bloch point first moves to the right storage area during part 1 with current applied from the left to the right as shown in the background of (a), then to the top during part 2 with current applied from the right to the top as shown in (b), and finally back to the left during part 3 with current applied from the top to the left as shown in (c).

5.6 T-shaped geometry

Finally, we study a single Bloch point in a T-shaped geometry with three storage areas. The geometry is shown in Fig. 5.12. It has the three storage areas *left* for $x < 200\,\text{nm}$, *right* for $x > 400\,\text{nm}$, and *top* for $y > 150\,\text{nm}$. They are separated by a total of four notches. We initialise the system in a state where it contains a single Bloch point in the left storage area (at $x \approx 135\,\text{nm}$). We apply a series of current pulses of varying strength between different pairs of strip ends to move the Bloch point first to the right storage area, then to the top storage area, and finally back to the left storage area.

Each part of the movement consists of three steps: (i) long current pulse with $J_{(\text{i})} = 0.7 \times 10^{12}\,\text{A/m}^2$ to move the Bloch point to the notches where it gets stuck, (ii) short current pulse with $J_{(\text{ii})} = 6.6 \times 10^{12}\,\text{A/m}^2$ to push the Bloch point past the notches, and (iii) free relaxation. The weak pulse (i) is always applied for $\Delta t_{(\text{i})} = 2\,\text{ns}$, during which the Bloch point moves towards the notch and gets stuck well before the end of the simulation time. The duration of the strong pulse depends on the part of the motion (see below). For the free relaxation in step (iii) we simulate the time evolution of the system until it reaches an equilibrium state (roughly for $\Delta t_{(\text{iii})} = 2 - 4\,\text{ns}$).

Figure 5.12a shows the position of the Bloch point during the full cycle. The three parts of the trajectory are shown with a solid orange line for the motion left–right (part 1), a dotted olive line for the motion right–top (part 2), and a dashed cyan line for the motion top–left (part 3). The background in Fig. 5.12a shows the magnitude of the current density for the current flowing from the left to the right, streamlines show the current direction. Figures 5.12b and c show the current flowing from the right to the top and from the top to the left, respectively.

For the motion left–right, we apply the strong pulse for $\Delta t_{(ii)} = 0.7\,\text{ns}$. We can see a slight overshoot at the end of the pulse. During the free relaxation, the Bloch point moves in $-x$ direction to its equilibrium position at $x \approx 500\,\text{nm}$ near the centre of the right storage area. For the motion right–top, we apply the strong pulse for $\Delta t_{(ii)} = 0.5\,\text{ns}$. Here, we can see a strong overshoot with the Bloch point nearly reaching the top sample boundary at $y = 300\,\text{nm}$. During the free relaxation, the Bloch point moves back to the central part of the storage area at $y \approx 200\,\text{nm}$. For the final motion top–left, we apply the strong pulse for $\Delta t_{(iii)} = 0.7\,\text{ns}$. After moving past the two notches, the Bloch point gets deflected in $+y$ direction. This deflection is a result of the uneven thickness of the two layers (bottom layer $t_b = 20\,\text{nm}$, top layer $t_t = 10\,\text{nm}$) and the deformed, off-centred Bloch point after it moves past the notches and the junction. We have simulated a second system with layer thicknesses $t_b = 17.5\,\text{nm}$ and $t_t = 12.5\,\text{nm}$ and find that the effect decreases. During the free relaxation, the Bloch point moves back to the central part of the storage area at $x \approx 115\,\text{nm}$. The slightly different initial and final position in the left storage area result from the differences in the initial and final magnetisation configuration due to the series of applied current pulses and the nearly flat energy landscape for a Bloch point inside a storage area. Qualitatively similar behaviour can be seen in Fig. 5.10, where the free Bloch point also relaxes slightly off-centred.

5.7 Discussion

Our micromagnetic simulations show that Bloch points—which are equilibrium configurations in two-layer FeGe nanostrips—can be moved with spin-polarised currents. In uniform strips, Bloch points move along the current direction without a Hall effect, independent of their type. This is different from the behaviour of vortices (He et al., 2006; Shibata et al., 2006; Nakatani et al., 2008) or skyrmions (Zang et al., 2011; Jiang et al., 2017a; Litzius et al., 2017), and also Bloch points in other systems (Gong et al., 2021). The straight motion is a special feature of the two-layer system, in which each Bloch point is encapsulated between two vortices with opposite polarisation. The vortices would be subject to deflection in opposite direction but are strongly exchange-coupled across the layer interface. At the Bloch point the forces are compensated, and thus the Bloch point moves in a straight line. Different behaviour has been reported by Gong et al. (2021), who have studied current-induced dynamics of a chiral bobber (Rybakov et al., 2015; Zheng et al., 2018; Ahmed et al., 2018), a skyrmion tube that ends in a Bloch point. They have simulated thin FeGe films with a single material chirality with applied spin-transfer torque and observe a motion of the chiral bobber, and hence also the Bloch point, with a current-dependent Hall effect.

In the system studied here, changes in geometry can be used to modify the motion. We have demonstrated that below a threshold current density, a Bloch point can be trapped by a notch. The Bloch point holds its position because the current is pushing it towards the notch constriction, but the Bloch point is repelled from the boundary and does not want to deform, and thus it cannot move past the notch. Using these competing effects, we can choose

appropriate current strengths to either neatly align a Bloch point at a notch or move it past a notch. Using a series of current pulses of different strength, we can move an array of Bloch points of different type through strips with multiple notches in a controlled fashion. They retain their initial order and relative distance in terms of empty or occupied storage areas. The additional antivortices between same-type Bloch points do not impede this process, despite not being trapped at the notches themselves. In each storage area, we can distinguish between three different local configurations: a HH Bloch point, a TT Bloch point, or no Bloch point.

Furthermore, we have demonstrated that Bloch points can be moved through more complex geometries with multiple possible paths. We have demonstrated this for a T-shaped geometry, where the Bloch point can move along either of the two possible strip ends when being pushed towards the junction depending on the direction of the applied current. In this system, we have added additional constrictions at the junction to create three well-separated storage areas. The Bloch point in the free system reaches an equilibrium position in each of the three storage areas. A weak and subsequent strong pulse can be used to move the Bloch point between storage areas.

In a larger system, these two building blocks—constrictions to restrict the Bloch-point motion and junctions with multiple possible paths—can be combined. Such a system can then host an array of Bloch points and the geometrical constraints can be used to manipulate the array, e.g. re-arrange Bloch points with a series of current pulses between different contacts. Successful operation will likely require more device engineering.

Speculating about potential applications, a simple nanostrip containing a series of Bloch points could be used in a racetrack-like design (Parkin et al., 2008), and the two Bloch-point types could be used for binary data representation. The whole array of Bloch points could be moved with spin currents. Retaining equal spacing would not be required because of the two different types that could encode “0” and “1”, which is not the case in skyrmion-based racetrack memories. In a more complex setup, we have shown that a series of notches in a strip can be used to create confined “storage areas”. Bloch points can be distributed across these areas, where each area can be in one of three states: occupied with a HH Bloch point, occupied with a TT Bloch point, or not containing a Bloch point—with the potential to realise a ternary storage device. The whole configuration could be moved through this strip using a series of current pulses. Pinning of the Bloch points at the notches helps control the movement and ensures that the configuration is retained.

Chapter 6

Conclusion

Bloch points are topologically non-trivial point singularities in the magnetisation vector field. They are dynamically generated and annihilated in many magnetisation reversal processes. Some systems can also host static Bloch points. In the present work, we have numerically studied one such system: a FeGe nanostrip consisting of two layers with opposite material chirality.

Using finite-difference micromagnetic simulations, we have investigated both statics and dynamics of Bloch points in the two-layer system. In this specific set-up, a Bloch point can be realised in two different types, which are energetically equivalent. We have demonstrated that two-layer FeGe nanostrips of suitable geometry can host multiple coexisting Bloch points in any possible combination of the two types (Chap. 4). We find that neighbouring Bloch points of the same type are separated by an additional antivortex, which increases the total energy of the system. Based on our simulations for up to eight Bloch points, we can predict suitable geometries for an arbitrary number of Bloch points. We have tested these predictions for a configuration containing 80 Bloch points (Sec. 4.7).

We can manipulate Bloch points in this system using spin-transfer torques (Chap. 5). We find that arrays of Bloch points can be moved collectively, independent of their individual type and arrangement. In the two-layer system, Bloch points move without any Hall effect. We have demonstrated that more complex strip geometries can be used to control the motion of the Bloch points. In a nanostrip with a notch, Bloch points can get stuck at the notch for lower current densities or be pushed past the notch for higher current densities, which allows for a controlled, discrete motion triggered with short current pulses. In a structure with multiple possible paths, such as the T-shaped structure studied in Sec. 5.6, the movement of a Bloch point can be controlled by applying current between suitable contacts.

For all simulations in this work, we use the Python package Ubermag with OOMMF as the numerical backend. The high-level description of the micromagnetic problem in the domain-specific language provided by Ubermag has significantly simplified the present work. In

particular, the integration into the Python ecosystem is useful for semi-automated control of larger numbers of simulations with custom scripts. Where required for the work, we have extended or modified Ubermag. Most notably, we have significantly improved its interactive visualisation capabilities. All of this software work is published under a permissive open-source licence and can be used by the community.

Speculating about potential applications, Bloch points in the two-layer system exhibit several properties that could be beneficial for racetrack memory. They can exist in two different energetically equivalent configurations, which could be used to encode data in binary format. We have demonstrated this for a system containing 80 Bloch points in Sec. 4.7, where we encode the word "Blochpoint" in ASCII encoding. Arrays of Bloch points—hence arrays of bits—can be moved with spin currents without loosing their order. Because of the two different types, it is not necessary to retain a fixed distance between Bloch points to prevent data loss. In a micro-structured nanostrip with storage areas separated by constrictions, Bloch points can be moved with control over their distance (Sec. 5.5). Such a system could also allow for ternary data storage with the states: head-to-head Bloch point, tail-to-tail Bloch point, no Bloch point.

Going beyond the present work, full control over Bloch points in the two-layer nanostrip would additionally require mechanisms for controlled creation and annihilation of individual Bloch points. The combination of both processes would then also provide means to switch the type of a Bloch point. Additionally, more direct means of switching a Bloch point may also be possible. These questions could be addressed in the same micromagnetic framework and could directly extend the present work. Other open questions, requiring different techniques, comprise energy barriers between different multi-Bloch-point configurations and thermal stability of Bloch points in the two-layer system, among others. One of the main problems for potential use in actual devices is the detection of Bloch points. Electrical detection methods might be suitable to probe the presence or absence of a Bloch point, however it is not clear whether distinguishing the two different types would also be possible. Other methods such as tomography, which are currently used to resolve the magnetisation structure around Bloch points are not suitable for devices.

The two-layer geometry with stable Bloch points forms an interesting system from a fundamental point of view. The Bloch points in this system can be interpreted as particles of two different types that form a metamaterial. The individual particles can move around and interact with each other. In the present work, focused on long, narrow nanostrips, Bloch points are generally distributed in x direction and hence form a quasi-1D metamaterial. Our simulations revealed repulsive forces between nearby Bloch points. In the investigated system, these forces can affect neighbouring Bloch points over distances of several 100 nm, mediated via the vortices enclosing the Bloch points. In extended two-layer thin films, we can expect Bloch points to be distributed in x and y direction. Depending on their density, Bloch points could presumably arrange in ordered 2D lattices or distribute more irregularly. Such a system could exhibit a variety of phenomena, such as domain formation or a melting transition of the metamaterial's crystal lattice, and provide more insights into the interaction of Bloch points.

Bibliography

Abert, C. (2019). Micromagnetics and spintronics: Models and numerical methods. *The European Physical Journal B*, **92** (6), 120.

Ado, I. A., Qaiumzadeh, A., Brataas, A. & Titov, M. (2020). Chiral ferromagnetism beyond Lifshitz invariants. *Physical Review B*, **101** (16), 161403.

Ahmed, A. S., Rowland, J., Esser, B. D., Dunsiger, S. R., McComb, D. W., Randeria, M. & Kawakami, R. K. (2018). Chiral bobbers and skyrmions in epitaxial FeGe/Si(111) films. *Physical Review Materials*, **2** (4), 041401.

Aji, S., Oda, T., Fujishiro, Y., Kanazawa, N., Saito, H., Endo, H., Hino, M., Itoh, S., Arima, T.-h., Tokura, Y. & Nakajima, T. (2023). *Direct observations of spin fluctuations in spin-hedgehog-anti-hedgehog lattice states in $MnSi_{1-x}Ge_x$ ($x = 0.6$ and 0.8) at zero magnetic field*. arXiv: 2305.01172 [cond-mat].

Al Khawaja, U. & Stoof, H. (2001). Skyrmions in a ferromagnetic Bose–Einstein condensate. *Nature*, **411** (6840), 918–920.

Allwood, D. A., Xiong, G., Faulkner, C. C., Atkinson, D., Petit, D. & Cowburn, R. P. (2005). Magnetic Domain-Wall Logic. *Science*, **309** (5741), 1688–1692.

Alnæs, M. S., Logg, A., Ølgaard, K. B., Rognes, M. E. & Wells, G. N. (2014). Unified form language: A domain-specific language for weak formulations of partial differential equations. *ACM Transactions on Mathematical Software*, **40** (2), 9:1–9:37.

Andreas, C., Kákay, A. & Hertel, R. (2014). Multiscale and multimodel simulation of Bloch-point dynamics. *Physical Review B*, **89** (13), 134403.

Askey, J., Hunt, M., Langbein, W. & Ladak, S. (2022). Asymmetric dual Bloch point domain walls in cylindrical magnetic nanowires. *APL Materials*, **10** (7), 071105.

Baji, T. (2018). Evolution of the GPU Device widely used in AI and Massive Parallel Processing. *2018 IEEE 2nd Electron Devices Technology and Manufacturing Conference (EDTM)*, 7–9.

Baker, M. (2016). 1,500 scientists lift the lid on reproducibility. *Nature*, **533** (7604), 452–454.

Bazaliy, Ya. B., Jones, B. A. & Zhang, S.-C. (1998). Modification of the Landau-Lifshitz equation in the presence of a spin-polarized current in colossal- and giant-magnetoresistive materials. *Physical Review B*, **57** (6), R3213–R3216.

Beg, M., Carey, R., Wang, W., Cortés-Ortuño, D., Vousden, M., Bisotti, M.-A., Albert, M., Chernyshenko, D., Hovorka, O., Stamps, R. L. & Fangohr, H. (2015). Ground state search,

hysteretic behaviour and reversal mechanism of skyrmionic textures in confined helimagnetic nanostructures. *Scientific Reports*, **5** (1), 17137.

Beg, M., Albert, M., Bisotti, M.-A., Cortés-Ortuño, D., Wang, W., Carey, R., Vousden, M., Hovorka, O., Ciccarelli, C., Spencer, C. S., Marrows, C. H. & Fangohr, H. (2017a). Dynamics of skyrmionic states in confined helimagnetic nanostructures. *Physical Review B*, **95** (1), 014433.

Beg, M., Pepper, R. A. & Fangohr, H. (2017b). User interfaces for computational science: A domain specific language for OOMMF embedded in Python. *AIP Advances*, **7** (5), 056025.

Beg, M., Pepper, R. A., Cortés-Ortuño, D., Atie, B., Bisotti, M.-A., Downing, G., Kluyver, T., Hovorka, O. & Fangohr, H. (2019). Stable and manipulable Bloch point. *Scientific Reports*, **9** (1), 7959.

Beg, M., Taka, J., Kluyver, T., Konovalov, A., Ragan-Kelley, M., Thiéry, N. M. & Fangohr, H. (2021). Using Jupyter for Reproducible Scientific Workflows. *Computing in Science Engineering*, **23** (2), 36–46.

Beg, M., Lang, M. & Fangohr, H. (2022). Ubermag: Toward More Effective Micromagnetic Workflows. *IEEE Transactions on Magnetics*, **58** (2), 1–5.

Behncke, C., Adolff, C. F. & Meier, G. (2018). Magnetic Vortices. In J. Zang, V. Cros & A. Hoffmann (Eds.), *Topology in Magnetism* (pp. 75–115). Springer International Publishing.

Berg, B. & Lüscher, M. (1981). Definition and statistical distributions of a topological number in the lattice O(3) σ-model. *Nuclear Physics B*, **190** (2), 412–424.

Berger, L. (1996). Emission of spin waves by a magnetic multilayer traversed by a current. *Physical Review B*, **54** (13), 9353–9358.

Berry, M. V. (1984). Quantal phase factors accompanying adiabatic changes. *Proceedings of the Royal Society of London. A. Mathematical and Physical Sciences*, **392** (1802), 45–57.

Birch, M., Cortés-Ortuño, D., Turnbull, L., Wilson, M., Groß, F., Träger, N., Laurenson, A., Bukin, N., Moody, S., Weigand, M., Schütz, G., Popescu, H., Fan, R., Steadman, P., Verezhak, J., Balakrishnan, G., Loudon, J., Twitchett-Harrison, A., Hovorka, O., … Hatton, P. (2020). Real-space imaging of confined magnetic skyrmion tubes. *Nature Communications*, **11** (1).

Bläsing, R., Khan, A. A., Filippou, P. C., Garg, C., Hameed, F., Castrillon, J. & Parkin, S. S. P. (2020). Magnetic Racetrack Memory: From Physics to the Cusp of Applications Within a Decade. *Proceedings of the IEEE*, **108** (8), 1303–1321.

Bogdanchikov, A., Zhaparov, M. & Suliyev, R. (2013). Python to learn programming. *Journal of Physics: Conference Series*, **423**, 012027.

Bogdanov, A. & Yablonskiui, D. (1989). Thermodynamically stable “vortices” in magnetically ordered crystals. The mixed state of magnets. *Sov. Phys. JETP*, **68**, 101.

Bogdanov, A. N. & Panagopoulos, C. (2020). Physical foundations and basic properties of magnetic skyrmions. *Nature Reviews Physics*, **2** (9), 492–498.

Bohlens, S., Krüger, B., Drews, A., Bolte, M., Meier, G. & Pfannkuche, D. (2008). Current controlled random-access memory based on magnetic vortex handedness. *Applied Physics Letters*, **93** (14), 142508.

Bonomi, M., Bussi, G., Camilloni, C., Tribello, G. A., Banáš, P., Barducci, A., Bernetti, M., Bolhuis, P. G., Bottaro, S., Branduardi, D., Capelli, R., Carloni, P., Ceriotti, M., Cesari, A., Chen, H., Chen, W., Colizzi, F., De, S., De La Pierre, M., … The PLUMED consortium. (2019). Promoting transparency and reproducibility in enhanced molecular simulations. *Nature Methods*, **16** (8), 670–673.

Bourianoff, G., Pinna, D., Sitte, M. & Everschor-Sitte, K. (2018). Potential implementation of reservoir computing models based on magnetic skyrmions. *AIP Advances*, **8** (5), 055602.

Brown, W. F. (1963). *Micromagnetics.* Interscience Publishers.

Bruno, P., Dugaev, V. K. & Taillefumier, M. (2004). Topological Hall Effect and Berry Phase in Magnetic Nanostructures. *Physical Review Letters*, **93** (9), 096806.

Büttner, F., Moutafis, C., Schneider, M., Krüger, B., Günther, C. M., Geilhufe, J., Schmising, C. v. K., Mohanty, J., Pfau, B., Schaffert, S., Bisig, A., Foerster, M., Schulz, T., Vaz, C. a. F., Franken, J. H., Swagten, H. J. M., Kläui, M. & Eisebitt, S. (2015). Dynamics and inertia of skyrmionic spin structures. *Nature Physics*, **11** (3), 225–228.

Carpentieri, M., Tomasello, R., Zivieri, R. & Finocchio, G. (2015). Topological, non-topological and instanton droplets driven by spin-transfer torque in materials with perpendicular magnetic anisotropy and Dzyaloshinskii–Moriya Interaction. *Scientific Reports*, **5** (1), 16184.

Caso, D., Tuero, P., Garcia, J., Guslienko, K. Y. & Aliev, F. G. (2023). *Dynamics and reversible control of the vortex Bloch-point vortex domain wall in short cylindrical magnetic nanowires*. arXiv: 2305.00346 [cond-mat].

Chandrasekhar, S. & Ranganath, G. (1986). The structure and energetics of defects in liquid crystals. *Advances in Physics*, **35** (6), 507–596.

Charilaou, M. (2020). Prediction of confined and controllable Bloch points in nanocubes of chiral magnets. *Physical Review B*, **102** (1), 014430.

Chen, M.-C. & Roy, K. (2017). *Magnetic Skyrmions for Cache Memory*. arXiv: 1705.01095 [physics.app-ph].

Cortés-Ortuño, D., Beg, M., Nehruji, V., Pepper, R. A. & Fangohr, H. (2018a). *OOMMF extension: Dzyaloshinskii-Moriya interaction (DMI) for crystallographic classes T and O*. Zenodo.

Cortés-Ortuño, D., Beg, M., Nehruji, V., Breth, L., Pepper, R., Kluyver, T., Downing, G., Hesjedal, T., Hatton, P., Lancaster, T., Hertel, R., Hovorka, O. & Fangohr, H. (2018b). Proposal for a micromagnetic standard problem for materials with Dzyaloshinskii–Moriya interaction. *New Journal of Physics*, **20** (11), 113015.

Cullity, B. D. & Graham, C. D. (2009). *Introduction to Magnetic Materials*. John Wiley & Sons, Inc.

Da Col, S., Jamet, S., Rougemaille, N., Locatelli, A., Mentes, T. O., Burgos, B. S., Afid, R., Darques, M., Cagnon, L., Toussaint, J. C. & Fruchart, O. (2014). Observation of Bloch-point domain walls in cylindrical magnetic nanowires. *Physical Review B*, **89** (18), 180405.

Diethelm, K. (2012). The Limits of Reproducibility in Numerical Simulation. *Computing in Science & Engineering*, **14** (1), 64–72.

Donahue, M. J. & Porter, D. (1999). OOMMF User's Guide, Version 1.0. *Interagency Report NISTIR 6376, National Institute of Standards and Technology, Gaithersburg, MD*.

Donnelly, C., Guizar-Sicairos, M., Scagnoli, V., Gliga, S., Holler, M., Raabe, J. & Heyderman, L. J. (2017). Three-dimensional magnetization structures revealed with X-ray vector nanotomography. *Nature*, **547** (7663), 328–331.

Donnelly, C., Metlov, K. L., Scagnoli, V., Guizar-Sicairos, M., Holler, M., Bingham, N. S., Raabe, J., Heyderman, L. J., Cooper, N. R. & Gliga, S. (2021). Experimental observation of vortex rings in a bulk magnet. *Nature Physics*, **17** (3), 316–321.

Döring, W. (1968). Point Singularities in Micromagnetism. *Journal of Applied Physics*, **39** (2), 1006–1007.

Drews, A., Krüger, B., Meier, G., Bohlens, S., Bocklage, L., Matsuyama, T. & Bolte, M. (2009). Current- and field-driven magnetic antivortices for nonvolatile data storage. *Applied Physics Letters*, **94** (6), 062504.

Dzyaloshinsky, I. (1958). A thermodynamic theory of "weak" ferromagnetism of antiferromagnetics. *Journal of Physics and Chemistry of Solids*, **4** (4), 241–255.

Ekreem, N. B., Olabi, A. G., Prescott, T., Rafferty, A. & Hashmi, M. S. J. (2007). An overview of magnetostriction, its use and methods to measure these properties. *Journal of Materials Processing Technology*, **191** (1), 96–101.

Elías, R. G. & Verga, A. (2011). Magnetization structure of a Bloch point singularity. *The European Physical Journal B*, **82** (2), 159.

Everschor-Sitte, K., Masell, J., Reeve, R. M. & Kläui, M. (2018). Perspective: Magnetic skyrmions – Overview of recent progress in an active research field. *Journal of Applied Physics*, **124** (24), 240901.

Everschor-Sitte, K. & Sitte, M. (2014). Real-space Berry phases: Skyrmion soccer (invited). *Journal of Applied Physics*, **115** (17), 172602.

Exl, L., Suess, D. & Schrefl, T. (2020). Micromagnetism. In M. Coey & S. Parkin (Eds.), *Handbook of Magnetism and Magnetic Materials* (pp. 1–44). Springer International Publishing.

Fangohr, H., Chernyshenko, D. S., Franchin, M., Fischbacher, T. & Meier, G. (2011). Joule heating in nanowires. *Physical Review B*, **84** (5), 054437.

Feldtkeller, E. (1965). Mikromagnetisch stetige und unstetige Magnetisierungskonfigurationen. *Zeitschrift für Angewandte Physik*, **19** (6), 530–536.

Fert, A., Cros, V. & Sampaio, J. (2013). Skyrmions on the track. *Nature Nanotechnology*, **8** (3), 152–156.

Fert, A., Reyren, N. & Cros, V. (2017). Magnetic skyrmions: Advances in physics and potential applications. *Nature Reviews Materials*, **2** (7), 1–15.

Fidler, J. & Schrefl, T. (2000). Micromagnetic modelling – the current state of the art. *Journal of Physics D: Applied Physics*, **33** (15), R135–R156.

Finocchio, G., Ricci, M., Tomasello, R., Giordano, A., Lanuzza, M., Puliafito, V., Burrascano, P., Azzerboni, B. & Carpentieri, M. (2015). Skyrmion based microwave detectors and harvesting. *Applied Physics Letters*, **107** (26), 262401.

Finocchio, G., Büttner, F., Tomasello, R., Carpentieri, M. & Kläui, M. (2016). Magnetic skyrmions: From fundamental to applications. *Journal of Physics D: Applied Physics*, **49** (42), 423001.

Freitas, P. P. & Berger, L. (1985). Observation of s-d exchange force between domain walls and electric current in very thin Permalloy films. *Journal of Applied Physics*, **57** (4), 1266–1269.

Fujishiro, Y., Kanazawa, N., Nakajima, T., Yu, X. Z., Ohishi, K., Kawamura, Y., Kakurai, K., Arima, T., Mitamura, H., Miyake, A., Akiba, K., Tokunaga, M., Matsuo, A., Kindo, K., Koretsune, T., Arita, R. & Tokura, Y. (2019). Topological transitions among skyrmion- and hedgehog-lattice states in cubic chiral magnets. *Nature Communications*, **10** (1), 1059.

Fujishiro, Y., Kanazawa, N. & Tokura, Y. (2020). Engineering skyrmions and emergent monopoles in topological spin crystals. *Applied Physics Letters*, **116** (9), 090501.

Fukuda, J.-I. & Žumer, S. (2011). Quasi-two-dimensional Skyrmion lattices in a chiral nematic liquid crystal. *Nature Communications*, **2** (1).

Gambardella, P. & Miron, I. M. (2011). Current-induced spin–orbit torques. *Philosophical Transactions of the Royal Society A: Mathematical, Physical and Engineering Sciences*, **369** (1948), 3175–3197.

Garst, M., Waizner, J. & Grundler, D. (2017). Collective spin excitations of helices and magnetic skyrmions: Review and perspectives of magnonics in non-centrosymmetric magnets. *Journal of Physics D: Applied Physics*, **50** (29), 293002.

Geuzaine, C. & Remacle, J.-F. (2009). Gmsh: A 3-D finite element mesh generator with built-in pre- and post-processing facilities. *International Journal for Numerical Methods in Engineering*, **79** (11), 1309–1331.

Gilbert, T. (1955). A Lagrangian Formulation of the Gyromagnetic Equation of the Magnetization Field. *Physical Review D*.

Gilbert, T. L. (2004). A phenomenological theory of damping in ferromagnetic materials. *IEEE Transactions on Magnetics*, **40** (6), 3443–3449.

Giuliani, G., Camara, G., Killough, B. & Minchin, S. (2019). Earth Observation Open Science: Enhancing Reproducible Science Using Data Cubes. *Data*, **4** (4), 147.

Göbel, B., Mook, A., Henk, J. & Mertig, I. (2017). Unconventional topological Hall effect in skyrmion crystals caused by the topology of the lattice. *Physical Review B*, **95** (9), 094413.

Göbel, B., Akosa, C. A., Tatara, G. & Mertig, I. (2020). Topological Hall signatures of magnetic hopfions. *Physical Review Research*, **2** (1), 013315.

Göbel, B., Mertig, I. & Tretiakov, O. A. (2021). Beyond skyrmions: Review and perspectives of alternative magnetic quasiparticles. *Physics Reports*, **895**, 1–28.

Gong, Z., Tang, J., Pershoguba, S. S., Xie, Z., Sun, R., Li, Y., Yang, X., Liu, J., Zhang, W., Zhang, X., He, W., Du, H., Zang, J. & Cheng, Z.-h. (2021). Current-induced dynamics and tunable spectra of a magnetic chiral bobber. *Physical Review B*, **104** (10), L100412.

Granger, B. E. & Pérez, F. (2021). Jupyter: Thinking and Storytelling With Code and Data. *Computing in Science Engineering*, **23** (2), 7–14.

Grollier, J., Querlioz, D. & Stiles, M. D. (2016). Spintronic Nanodevices for Bioinspired Computing. *Proceedings of the IEEE*, **104** (10), 2024–2039.

Haldar, A. & Buchanan, K. S. (2013). Magnetic antivortex formation in pound-key-like nanostructures. *Applied Physics Letters*, **102** (11), 112401.

Hamamoto, K., Ezawa, M. & Nagaosa, N. (2015). Quantized topological Hall effect in skyrmion crystal. *Physical Review B*, **92** (11), 115417.

Han, J. H. (2017). *Skyrmions in Condensed Matter* (Vol. 278). Springer International Publishing.

Harris, C. R., Millman, K. J., van der Walt, S. J., Gommers, R., Virtanen, P., Cournapeau, D., Wieser, E., Taylor, J., Berg, S., Smith, N. J., Kern, R., Picus, M., Hoyer, S., van Kerkwijk, M. H., Brett, M., Haldane, A., del Río, J. F., Wiebe, M., Peterson, P., … Oliphant, T. E. (2020). Array programming with NumPy. *Nature*, **585** (7825), 357–362.

Hasegawa, R. (1975). Effect of Bloch points on the dynamic properties of bubble domain. *AIP Conference Proceedings*, **24**, 615–616.

He, J., Li, Z. & Zhang, S. (2006). Current-driven vortex domain wall dynamics by micromagnetic simulations. *Physical Review B*, **73** (18), 184408.

He, Z., Angizi, S. & Fan, D. (2017). Current-Induced Dynamics of Multiple Skyrmions With Domain-Wall Pair and Skyrmion-Based Majority Gate Design. *IEEE Magnetics Letters*, **8**, 1–5.

Heinze, S., von Bergmann, K., Menzel, M., Brede, J., Kubetzka, A., Wiesendanger, R., Bihlmayer, G. & Blügel, S. (2011). Spontaneous atomic-scale magnetic skyrmion lattice in two dimensions. *Nature Physics*, **7** (9), 713–718.

Hermosa, J., Hierro-Rodríguez, A., Quirós, C., Martín, J. I., Sorrentino, A., Aballe, L., Pereiro, E., Vélez, M. & Ferrer, S. (2023). Bloch points and topological dipoles observed by X-ray vector magnetic tomography in a ferromagnetic microstructure. *Communications Physics*, **6** (1), 1–10.

Hertel, R. (2016). Ultrafast domain wall dynamics in magnetic nanotubes and nanowires. *Journal of Physics: Condensed Matter*, **28** (48), 483002.

Hertel, R., Gliga, S., Fähnle, M. & Schneider, C. M. (2007). Ultrafast Nanomagnetic Toggle Switching of Vortex Cores. *Physical Review Letters*, **98** (11), 117201.

Hertel, R. & Andreas, C. (2015). 22 - Multiscale simulation of Bloch point dynamics in thick nanowires. In M. Vázquez (Ed.), *Magnetic Nano- and Microwires* (pp. 653–677). Woodhead Publishing.

Hertel, R. & Kirschner, J. (2004). Magnetic drops in a soft-magnetic cylinder. *Journal of Magnetism and Magnetic Materials*, **278** (3), L291–L297.

Hertel, R. & Schneider, C. M. (2006). Exchange Explosions: Magnetization Dynamics during Vortex-Antivortex Annihilation. *Physical Review Letters*, **97** (17), 177202.

Hierro-Rodriguez, A., Quirós, C., Sorrentino, A., Alvarez-Prado, L. M., Martín, J. I., Alameda, J. M., McVitie, S., Pereiro, E., Vélez, M. & Ferrer, S. (2020). Revealing 3D magnetization of thin films with soft X-ray tomography: Magnetic singularities and topological charges. *Nature Communications*, **11** (1), 6382.

Hillebrands, B. & Thiaville, A. (Eds.). (2006). *Spin dynamics in confined magnetic structures III*. Springer.

Holt, S. J. R. (2021). *Structure and magnetism of skyrmion hosting materials* (Doctoral dissertation). University of Warwick.

Hoyer, S. & Hamman, J. (2017). Xarray: N-D labeled Arrays and Datasets in Python. *Journal of open research software*, **5** (1), 10.

Huang, Y., Kang, W., Zhang, X., Zhou, Y. & Zhao, W. (2017). Magnetic skyrmion-based synaptic devices. *Nanotechnology*, **28** (8), 08LT02.

Huber, E. E., Smith, D. O. & Goodenough, J. B. (1958). Domain-Wall Structure in Permalloy Films. *Journal of Applied Physics*, **29** (3), 294–295.

Hubert, A. & Schäfer, R. (1998). *Magnetic Domains*. Springer.

Hunter, J. D. (2007). Matplotlib: A 2D Graphics Environment. *Computing in Science & Engineering*, **9** (3), 90–95.

Im, M.-Y., Han, H.-S., Jung, M.-S., Yu, Y.-S., Lee, S., Yoon, S., Chao, W., Fischer, P., Hong, J.-I. & Lee, K.-S. (2019). Dynamics of the Bloch point in an asymmetric permalloy disk. *Nature Communications*, **10** (1), 593.

Jamet, S., Rougemaille, N., Toussaint, J. C. & Fruchart, O. (2015). 25 - Head-to-head domain walls in one-dimensional nanostructures: An extended phase diagram ranging from strips to cylindrical wires. In M. Vázquez (Ed.), *Magnetic Nano- and Microwires* (pp. 783–811). Woodhead Publishing.

Janssen, J., Surendralal, S., Lysogorskiy, Y., Todorova, M., Hickel, T., Drautz, R. & Neugebauer, J. (2019). Pyiron: An integrated development environment for computational materials science. *Computational Materials Science*, **163**, 24–36.

Jantz, W., Slonczewski, J. C. & Argyle, B. E. (1981). Effects of Bloch lines and Bloch points on resonances of magnetic bubbles. *Journal of Magnetism and Magnetic Materials*, **23** (1), 8–14.

Jena, J., Göbel, B., Ma, T., Kumar, V., Saha, R., Mertig, I., Felser, C. & Parkin, S. S. P. (2020). Elliptical Bloch skyrmion chiral twins in an antiskyrmion system. *Nature Communications*, **11** (1), 1115.

Jiang, W., Upadhyaya, P., Zhang, W., Yu, G., Jungfleisch, M. B., Fradin, F. Y., Pearson, J. E., Tserkovnyak, Y., Wang, K. L., Heinonen, O., te Velthuis, S. G. E. & Hoffmann, A. (2015). Blowing magnetic skyrmion bubbles. *Science*, **349** (6245), 283–286.

Jiang, W., Zhang, X., Yu, G., Zhang, W., Wang, X., Benjamin Jungfleisch, M., Pearson, J. E., Cheng, X., Heinonen, O., Wang, K. L., Zhou, Y., Hoffmann, A. & te Velthuis, S. G. E. (2017a). Direct observation of the skyrmion Hall effect. *Nature Physics*, **13** (2), 162–169.

Jiang, W., Chen, G., Liu, K., Zang, J., te Velthuis, S. G. E. & Hoffmann, A. (2017b). Skyrmions in magnetic multilayers. *Physics Reports*, **704**, 1–49.

Jourdan, T. (2008). *Approche multiéchelle pour le magnétisme. Application aux hétérogénéités struc- turales et aux singularités magnétiques.* (Doctoral dissertation). Université Joseph-Fourier. Grenoble.

Kabanov, Yu. P., Dedukh, L. M. & Nikitenko, V. I. (1989). Bloch points in an oscillating Bloch line. *ZhETF Pisma Redaktsiiu*, **49** (10), 551–554.

Kamionka, T., Martens, M., Chou, K. W., Curcic, M., Drews, A., Schütz, G., Tyliszczak, T., Stoll, H., Van Waeyenberge, B. & Meier, G. (2010). Magnetic Antivortex-Core Reversal by Circular-Rotational Spin Currents. *Physical Review Letters*, **105** (13), 137204.

Kanazawa, N., Onose, Y., Arima, T., Okuyama, D., Ohoyama, K., Wakimoto, S., Kakurai, K., Ishiwata, S. & Tokura, Y. (2011). Large Topological Hall Effect in a Short-Period Helimagnet MnGe. *Physical Review Letters*, **106** (15), 156603.

Kanazawa, N., Kim, J.-H., Inosov, D. S., White, J. S., Egetenmeyer, N., Gavilano, J. L., Ishiwata, S., Onose, Y., Arima, T., Keimer, B. & Tokura, Y. (2012). Possible skyrmion-lattice ground state in the *B*20 chiral-lattice magnet MnGe as seen via small-angle neutron scattering. *Physical Review B*, **86** (13), 134425.

Kanazawa, N., White, J. S., Rønnow, H. M., Dewhurst, C. D., Morikawa, D., Shibata, K., Arima, T., Kagawa, F., Tsukazaki, A., Kozuka, Y., Ichikawa, M., Kawasaki, M. & Tokura, Y. (2017). Topological spin-hedgehog crystals of a chiral magnet as engineered with magnetic anisotropy. *Physical Review B*, **96** (22), 220414.

Kanazawa, N., Kitaori, A., White, J. S., Ukleev, V., Rønnow, H. M., Tsukazaki, A., Ichikawa, M., Kawasaki, M. & Tokura, Y. (2020). Direct Observation of the Statics and Dynamics of Emergent Magnetic Monopoles in a Chiral Magnet. *Physical Review Letters*, **125** (13), 137202.

Kang, W., Huang, Y., Zhang, X., Zhou, Y. & Zhao, W. (2016). Skyrmion-Electronics: An Overview and Outlook. *Proceedings of the IEEE*, **104** (10), 2040–2061.

Kasuya, T. (1956). A Theory of Metallic Ferro- and Antiferromagnetism on Zener's Model. *Progress of Theoretical Physics*, **16** (1), 45–57.

Kato, Y. & Motome, Y. (2023). Hidden topological transitions in emergent magnetic monopole lattices. *Physical Review B*, **107** (9), 094437.

Khodenkov, G. E. (2010). Exchange reduction of the magnetization modulus in the vicinity of a Bloch point. *Technical Physics*, **55** (5), 738–740.

Kim, D. H., Rozhkova, E. A., Ulasov, I. V., Bader, S. D., Rajh, T., Lesniak, M. S. & Novosad, V. (2010). Biofunctionalized magnetic-vortex microdiscs for targeted cancer-cell destruction. *Nature Materials*, **9** (2), 165–171.

Kim, J.-V. & Mulkers, J. (2020). On quantifying the topological charge in micromagnetics using a lattice-based approach. *IOP SciNotes*, **1** (2), 025211.

Kim, S. K. & Tchernyshyov, O. (2013). Pinning of a Bloch point by an atomic lattice. *Physical Review B*, **88** (17), 174402.

Kluyver, T., Ragan-Kelley, B., Pérez, F., Granger, B., Bussonnier, M., Frederic, J., Kelley, K., Hamrick, J., Grout, J., Corlay, S., Ivanov, P., Avila, D., Abdalla, S., Willing, C. & Team, J. D. (2016). Jupyter Notebooks – a publishing format for reproducible computational workflows. *Positioning and Power in Academic Publishing: Players, Agents and Agendas*, 87–90.

Kotiuga, P. (1989). The algebraic topology of Bloch points. *IEEE Transactions on Magnetics*, **25** (5), 3476–3478.

Krishnan, K. M. (2016). *Fundamentals and Applications of Magnetic Materials*. Oxford University Press.

Kufaev, Y. A. & Sonin, E. B. (1989). Dynamics of a Bloch point (point soliton) in a ferromagnet. *Zh. Eksp. Teor. Fiz.*, **95**, 1523–1529.

Landau, L. D. & Lifshitz, E. M. (1935). On the theory of the dispersion of magnetic permeability in ferromagnetic bodies. *Physikalische Zeitschrift der Sowjetunion*, **8** (2), 153–169.

Lang, M., Beg, M., Hovorka, O. & Fangohr, H. (2022). *Bloch points in nanostrips*. Zenodo.

Lang, M., Beg, M., Hovorka, O. & Fangohr, H. (2023a). Bloch points in nanostrips. *Scientific Reports*, **13** (1), 6910.

Lang, M., Pathak, S. A., Holt, S. J. R., Beg, M. & Fangohr, H. (2023b). Controlling stable Bloch points with electric currents. *Scientific Reports*, **13** (1), 18934.

Lang, M. & Fangohr, H. (2023). *OOMMF extension: Spin-transfer torque with arbitrary current direction (Zhang Li)*. Zenodo.

Lang, M., Pathak, S. A., Holt, S. J. R., Beg, M. & Fangohr, H. (2023c). *Supplementary repository: Controlling stable Bloch points with electric currents* (Version v1.0). Zenodo.

Larsen, A. H., Mortensen, J. J., Blomqvist, J., Castelli, I. E., Christensen, R., Dułak, M., Friis, J., Groves, M. N., Hammer, B., Hargus, C., Hermes, E. D., Jennings, P. C., Jensen, P. B., Kermode, J., Kitchin, J. R., Kolsbjerg, E. L., Kubal, J., Kaasbjerg, K., Lysgaard, S., … Jacobsen, K. W. (2017). The atomic simulation environment—a Python library for working with atoms. *Journal of Physics: Condensed Matter*, **29** (27), 273002.

Lebecki, K. M., Hinzke, D., Nowak, U. & Chubykalo-Fesenko, O. (2012). Key role of temperature in ferromagnetic Bloch point simulations. *Physical Review B*, **86** (9), 094409.

Lebrun, R., Jenkins, A., Dussaux, A., Locatelli, N., Tsunegi, S., Grimaldi, E., Kubota, H., Bortolotti, P., Yakushiji, K., Grollier, J., Fukushima, A., Yuasa, S. & Cros, V. (2015). Understanding of Phase Noise Squeezing Under Fractional Synchronization of a Nonlinear Spin Transfer Vortex Oscillator. *Physical Review Letters*, **115** (1), 017201.

Lebrun, R., Tsunegi, S., Bortolotti, P., Kubota, H., Jenkins, A. S., Romera, M., Yakushiji, K., Fukushima, A., Grollier, J., Yuasa, S. & Cros, V. (2017). Mutual synchronization of spin torque nano-oscillators through a long-range and tunable electrical coupling scheme. *Nature Communications*, **8** (1), 15825.

Lee, M., Kang, W., Onose, Y., Tokura, Y. & Ong, N. P. (2009). Unusual Hall Effect Anomaly in MnSi under Pressure. *Physical Review Letters*, **102** (18), 186601.

Li, S., Kang, W., Zhang, X., Nie, T., Zhou, Y., L. Wang, K. & Zhao, W. (2021). Magnetic skyrmions for unconventional computing. *Materials Horizons*, **8** (3), 854–868.

Li, Y., Pierobon, L., Charilaou, M., Braun, H.-B., Walet, N. R., Löffler, J. F., Miles, J. J. & Moutafis, C. (2020). Tunable terahertz oscillation arising from Bloch-point dynamics in chiral magnets. *Physical Review Research*, **2** (3), 033006.

Li, Y., Kanazawa, N., Yu, X. Z., Tsukazaki, A., Kawasaki, M., Ichikawa, M., Jin, X. F., Kagawa, F. & Tokura, Y. (2013). Robust Formation of Skyrmions and Topological Hall Effect Anomaly in Epitaxial Thin Films of MnSi. *Physical Review Letters*, **110** (11), 117202.

Litzius, K., Lemesh, I., Krüger, B., Bassirian, P., Caretta, L., Richter, K., Büttner, F., Sato, K., Tretiakov, O. A., Förster, J., Reeve, R. M., Weigand, M., Bykova, I., Stoll, H., Schütz, G., Beach, G. S. D. & Kläui, M. (2017). Skyrmion Hall effect revealed by direct time-resolved X-ray microscopy. *Nature Physics*, **13** (2), 170–175.

Liu, J. P., Zhang, Z. & Zhao, G. (Eds.). (2017). *Skyrmions: Topological structures, properties, and applications*. CRC Press, Taylor & Francis Group.

Liu, Y., Du, H., Jia, M. & Du, A. (2015). Switching of a target skyrmion by a spin-polarized current. *Physical Review B*, **91** (9), 094425.

Lonsky, M., Lang, M., Holt, S., Pathak, S. A., Klause, R., Lo, T.-H., Beg, M., Hoffmann, A. & Fangohr, H. (2023). *Developing computational skills through simulation based problem-solving in science*. arXiv: 2303.01784 [cond-mat].

Luo, S., Song, M., Li, X., Zhang, Y., Hong, J., Yang, X., Zou, X., Xu, N. & You, L. (2018). Reconfigurable Skyrmion Logic Gates. *Nano Letters*, **18** (2), 1180–1184.

Ma, F., Zhou, Y., Braun, H. B. & Lew, W. S. (2015). Skyrmion-Based Dynamic Magnonic Crystal. *Nano Letters*, **15** (6), 4029–4036.

Maccariello, D., Legrand, W., Reyren, N., Garcia, K., Bouzehouane, K., Collin, S., Cros, V. & Fert, A. (2018). Electrical detection of single magnetic skyrmions in metallic multilayers at room temperature. *Nature Nanotechnology*, **13** (3), 233–237.

Malozemoff, A. P. & Slonczewski, J. C. (1979). *Magnetic domain walls in bubble materials*. Academic Press.

Manchon, A. & Zhang, S. (2008). Theory of nonequilibrium intrinsic spin torque in a single nanomagnet. *Physical Review B*, **78** (21), 212405.

Manchon, A., Železný, J., Miron, I. M., Jungwirth, T., Sinova, J., Thiaville, A., Garello, K. & Gambardella, P. (2019). Current-induced spin-orbit torques in ferromagnetic and antiferromagnetic systems. *Reviews of Modern Physics*, **91** (3), 035004.

Markov, I. L. (2014). Limits on fundamental limits to computation. *Nature*, **512** (7513), 147–154.

Martens, M., Kamionka, T., Drews, A., Krüger, B. & Meier, G. (2012). Influence of the winding number on field- and current driven dynamics of magnetic vortices and antivortices. *Journal of Applied Physics*, **112** (1), 013917.

Masseboeuf, A., Jourdan, T., Lançon, F., Bayle-Guillemaud, P. & Marty, A. (2009). Probing magnetic singularities during magnetization process in FePd films. *Applied Physics Letters*, **95** (21), 212501.

McKinney, W. (2010). Data Structures for Statistical Computing in Python. In S. J. van der Walt (Ed.), *Proceedings of the 9th Python in Science Conference* (pp. 56–61). SciPy.

Mermin, N. D. (1979). The topological theory of defects in ordered media. *Reviews of Modern Physics*, **51** (3), 591–648.

Middelhoek, S. (1963). Domain Walls in Thin Ni–Fe Films. *Journal of Applied Physics*, **34** (4), 1054–1059.

Milde, P., Köhler, D., Seidel, J., Eng, L. M., Bauer, A., Chacon, A., Kindervater, J., Mühlbauer, S., Pfleiderer, C., Buhrandt, S., Schütte, C. & Rosch, A. (2013). Unwinding of a Skyrmion Lattice by Magnetic Monopoles. *Science*, **340** (6136), 1076–1080.

Mochizuki, M., Yu, X. Z., Seki, S., Kanazawa, N., Koshibae, W., Zang, J., Mostovoy, M., Tokura, Y. & Nagaosa, N. (2014). Thermally driven ratchet motion of a skyrmion microcrystal and topological magnon Hall effect. *Nature Materials*, **13** (3), 241–246.

Mohn, P. & Wohlfarth, E. P. (1987). The Curie temperature of the ferromagnetic transition metals and their compounds. *Journal of Physics F: Metal Physics*, **17** (12), 2421–2430.

Moore, G. E. (1965). Cramming more components onto integrated circuits. *Electronics*, **38** (8), 114–117.

Moore, G. E. (1975). Progress in Digital Integrated Electronics. *IEEE Int. Electron Devices Meeting Tech. Dig.*, 11–13.

Moreno, R., Carvalho-Santos, V. L., Altbir, D. & Chubykalo-Fesenko, O. (2022). Detailed examination of domain wall types, their widths and critical diameters in cylindrical magnetic nanowires. *Journal of Magnetism and Magnetic Materials*, **542**, 168495.

Moriya, T. (1960). Anisotropic Superexchange Interaction and Weak Ferromagnetism. *Physical Review*, **120** (1), 91–98.

Moutafis, C., Komineas, S. & Bland, J. A. C. (2009). Dynamics and switching processes for magnetic bubbles in nanoelements. *Physical Review B*, **79** (22), 224429.

Mühlbauer, S., Binz, B., Jonietz, F., Pfleiderer, C., Rosch, A., Neubauer, A., Georgii, R. & Böni, P. (2009). Skyrmion Lattice in a Chiral Magnet. *Science*, **323** (5916), 915–919.

Müller, G. P., Rybakov, F. N., Jónsson, H., Blügel, S. & Kiselev, N. S. (2020). Coupled quasi-monopoles in chiral magnets. *Physical Review B*, **101** (18), 184405.

Müller, J. (2016). Shape-dependence of the barrier for skyrmions on a two-lane racetrack. *Spintronics IX*, **9931**, 340–345.

Müller, J. (2017). Magnetic skyrmions on a two-lane racetrack. *New Journal of Physics*, **19** (2), 025002.

Mulugeta, L., Drach, A., Erdemir, A., Hunt, C. A., Horner, M., Ku, J. P., Myers Jr., J. G., Vadigepalli, R. & Lytton, W. W. (2018). Credibility, Replicability, and Reproducibility in Simulation for Biomedicine and Clinical Applications in Neuroscience. *Frontiers in Neuroinformatics*, **12**.

Nagaosa, N. & Tokura, Y. (2013). Topological properties and dynamics of magnetic skyrmions. *Nature Nanotechnology*, **8** (12), 899–911.

Nakatani, Y., Thiaville, A. & Miltat, J. (2003). Faster magnetic walls in rough wires. *Nature Materials*, **2** (8), 521–523.

Nakatani, Y., Thiaville, A. & Miltat, J. (2005). Head-to-head domain walls in soft nano-strips: A refined phase diagram. *Journal of Magnetism and Magnetic Materials*, **290–291**, 750–753.

Nakatani, Y., Shibata, J., Tatara, G., Kohno, H., Thiaville, A. & Miltat, J. (2008). Nucleation and dynamics of magnetic vortices under spin-polarized current. *Physical Review B*, **77** (1), 014439.

Neubauer, A., Pfleiderer, C., Binz, B., Rosch, A., Ritz, R., Niklowitz, P. G. & Böni, P. (2009). Topological Hall Effect in the A Phase of MnSi. *Physical Review Letters*, **102** (18), 186602.

Niedoba, H. & Labrune, M. (2005). Magnetization reversal via bloch points nucleation in nanowires and dots: A micromagnetic study. *The European Physical Journal B - Condensed Matter and Complex Systems*, **47** (4), 467–478.

Noske, M., Stoll, H., Fähnle, M., Hertel, R. & Schütz, G. (2015). Mechanisms for the symmetric and antisymmetric switching of a magnetic vortex core: Differences and common aspects. *Physical Review B*, **91** (1), 014414.

Okumura, S., Hayami, S., Kato, Y. & Motome, Y. (2020). Magnetic hedgehog lattices in noncentrosymmetric metals. *Physical Review B*, **101** (14), 144416.

Okuno, T. (2020). Spin-Transfer Torques for Domain Wall Motion in Antiferromagnetically-Coupled Ferrimagnets. In T. Okuno (Ed.), *Magnetic Dynamics in Antiferromagnetically-Coupled Ferrimagnets: The Role of Angular Momentum* (pp. 25–48). Springer.

Onoda, M., Tatara, G. & Nagaosa, N. (2004). Anomalous Hall Effect and Skyrmion Number in Real and Momentum Spaces. *Journal of the Physical Society of Japan*, **73** (10), 2624–2627.

Paradezhenko, G. V., A. Pervishko, A., Swain, N., Sengupta, P. & Yudin, D. (2022). Spin-hedgehog-derived electromagnetic effects in itinerant magnets. *Physical Chemistry Chemical Physics*, **24** (39), 24317–24322.

Parkin, S. S. P., Hayashi, M. & Thomas, L. (2008). Magnetic Domain-Wall Racetrack Memory. *Science*, **320** (5873), 190–194.

Peng, R. D. (2011). Reproducible Research in Computational Science. *Science*, **334** (6060), 1226–1227.

Piao, H.-G., Shim, J.-H., Djuhana, D. & Kim, D.-H. (2013). Intrinsic pinning behavior and propagation onset of three-dimensional Bloch-point domain wall in a cylindrical ferromagnetic nanowire. *Applied Physics Letters*, **102** (11), 112405.

Pimentel, J. F., Murta, L., Braganholo, V. & Freire, J. (2021). Understanding and improving the quality and reproducibility of Jupyter notebooks. *Empirical Software Engineering*, **26** (4), 65.

Pinna, D., Abreu Araujo, F., Kim, J.-V., Cros, V., Querlioz, D., Bessiere, P., Droulez, J. & Grollier, J. (2018). Skyrmion Gas Manipulation for Probabilistic Computing. *Physical Review Applied*, **9** (6), 064018.

Prychynenko, D., Sitte, M., Litzius, K., Krüger, B., Bourianoff, G., Kläui, M., Sinova, J. & Everschor-Sitte, K. (2018). Magnetic Skyrmion as a Nonlinear Resistive Element: A

Potential Building Block for Reservoir Computing. *Physical Review Applied*, **9** (1), 014034.

Pues, M., Martens, M. & Meier, G. (2014). Absorption spectroscopy of isolated magnetic antivortices. *Journal of Applied Physics*, **116** (15), 153903.

Pues, M. & Meier, G. (2018). Magnetic Antivortices. In R. Wiesendanger (Ed.), *Atomic- and Nanoscale Magnetism* (pp. 299–323). Springer International Publishing.

Pylypovskyi, O. V., Sheka, D. D. & Gaididei, Y. (2012). Bloch point structure in a magnetic nanosphere. *Physical Review B*, **85** (22), 224401.

Pylypovskyi, O. V., Sheka, D. D., Kravchuk, V. P. & Gaididei, Y. (2015). Vortex polarity switching in magnets with surface anisotropy. *Low Temperature Physics*, **41** (5), 361–374.

Ralph, D. C. & Stiles, M. D. (2008). Spin transfer torques. *Journal of Magnetism and Magnetic Materials*, **320** (7), 1190–1216.

Rana, A., Liao, C.-T., Iacocca, E., Zou, J., Pham, M., Lu, X., Subramanian, E.-E. C., Lo, Y. H., Ryan, S. A., Bevis, C. S., Karl, R. M., Glaid, A. J., Rable, J., Mahale, P., Hirst, J., Ostler, T., Liu, W., O'Leary, C. M., Yu, Y.-S., … Miao, J. (2023). Three-dimensional topological magnetic monopoles and their interactions in a ferromagnetic meta-lattice. *Nature Nanotechnology*, 1–6.

Richter, H. J. (2009). Density limits imposed by the microstructure of magnetic recording media. *Journal of Magnetism and Magnetic Materials*, **321** (6), 467–476.

Ruderman, M. A. & Kittel, C. (1954). Indirect Exchange Coupling of Nuclear Magnetic Moments by Conduction Electrons. *Physical Review*, **96** (1), 99–102.

Rudiger, P., Stevens, J.-L., Bednar, J. A., Hansen, S. H., Liquet, M., Andrew, Nijholt, B., Mease, J., B, C., Randelhoff, A., Tenner, V., maxalbert, Kaiser, M., ea42gh, stonebig, Samuels, J., Raillard, D., Pevey, K., LB, F., … Bampton, J. (2023). *Holoviz/holoviews: Version 1.17.0*. Zenodo.

Rule, A., Birmingham, A., Zuniga, C., Altintas, I., Huang, S.-C., Knight, R., Moshiri, N., Nguyen, M. H., Rosenthal, S. B., Pérez, F. & Rose, P. W. (2018). *Ten Simple Rules for Reproducible Research in Jupyter Notebooks*. arXiv: 1810.08055 [cs].

Rybakov, F. N., Borisov, A. B., Blügel, S. & Kiselev, N. S. (2015). New Type of Stable Particlelike States in Chiral Magnets. *Physical Review Letters*, **115** (11), 117201.

Sáez, G., Díaz, P., Vidal-Silva, N., Escrig, J. & Vogel, E. E. (2022a). Bloch points stabilization by means of diameter modulations in cylindrical nanowires. *Results in Physics*, **39**, 105768.

Sáez, G., Saavedra, E., Vidal-Silva, N., Escrig, J. & Vogel, E. E. (2022b). Dynamic susceptibility of a Bloch point singularity confined in a magnetic nanowire. *Results in Physics*, **37**, 105530.

Sampaio, J., Cros, V., Rohart, S., Thiaville, A. & Fert, A. (2013). Nucleation, stability and current-induced motion of isolated magnetic skyrmions in nanostructures. *Nature Nanotechnology*, **8** (11), 839–844.

Savchenko, A. S., Zheng, F., Kiselev, N. S., Yang, L., Rybakov, F. N., Blügel, S. & Dunin-Borkowski, R. E. (2022). Diversity of states in a chiral magnet nanocylinder. *APL Materials*, **10** (6), 061110.

Schaduangrat, N., Lampa, S., Simeon, S., Gleeson, M. P., Spjuth, O. & Nantasenamat, C. (2020). Towards reproducible computational drug discovery. *Journal of Cheminformatics*, **12** (1), 9.

Schryer, N. L. & Walker, L. R. (1974). The motion of 180° domain walls in uniform dc magnetic fields. *Journal of Applied Physics*, **45** (12), 5406–5421.

Schulz, T., Ritz, R., Bauer, A., Halder, M., Wagner, M., Franz, C., Pfleiderer, C., Everschor, K., Garst, M. & Rosch, A. (2012). Emergent electrodynamics of skyrmions in a chiral magnet. *Nature Physics*, **8** (4), 301–304.

Schütte, C. & Rosch, A. (2014). Dynamics and energetics of emergent magnetic monopoles in chiral magnets. *Physical Review B*, **90** (17), 174432.

Scroggs, M. W., Baratta, I. A., Richardson, C. N. & Wells, G. N. (2022a). Basix: A runtime finite element basis evaluation library. *Journal of Open Source Software*, **7** (73), 3982.

Scroggs, M. W., Dokken, J. S., Richardson, C. N. & Wells, G. N. (2022b). Construction of Arbitrary Order Finite Element Degree-of-Freedom Maps on Polygonal and Polyhedral Cell Meshes. *ACM Transactions on Mathematical Software*, **48** (2), 18:1–18:23.

Shibata, J., Nakatani, Y., Tatara, G., Kohno, H. & Otani, Y. (2006). Current-induced magnetic vortex motion by spin-transfer torque. *Physical Review B*, **73** (2), 020403.

Shimizu, K., Okumura, S., Kato, Y. & Motome, Y. (2021). Phase transitions between helices, vortices, and hedgehogs driven by spatial anisotropy in chiral magnets. *Physical Review B*, **103** (5), 054427.

Shinjo, T., Okuno, T., Hassdorf, R., Shigeto, K. & Ono, T. (2000). Magnetic Vortex Core Observation in Circular Dots of Permalloy. *Science*, **289** (5481), 930–932.

Sinova, J., Valenzuela, S. O., Wunderlich, J., Back, C. H. & Jungwirth, T. (2015). Spin Hall effects. *Reviews of Modern Physics*, **87** (4), 1213–1260.

Skyrme, T. H. R. (1962). A unified field theory of mesons and baryons. *Nuclear Physics*, **31**, 556–569.

Skyrme, T. H. R. & Schonland, B. F. J. (1961). A non-linear field theory. *Proceedings of the Royal Society of London. Series A. Mathematical and Physical Sciences*, **260** (1300), 127–138.

Slonczewski, J. C. (1975). Properties of Bloch points in bubble domains. *AIP Conference Proceedings*, **24** (1), 613–614.

Slonczewski, J. C. (1996). Current-driven excitation of magnetic multilayers. *Journal of Magnetism and Magnetic Materials*, **159** (1), L1–L7.

Sondhi, S., Karlhede, A., Kivelson, S. & Rezayi, E. (1993). Skyrmions and the crossover from the integer to fractional quantum Hall effect at small Zeeman energies. *Physical Review B*, **47** (24), 16419–16426.

Suess, D., Vogler, C., Bruckner, F., Heistracher, P. & Abert, C. (2018). A repulsive skyrmion chain as a guiding track for a racetrack memory. *AIP Advances*, **8** (11), 115301.

Suess, D., Fidler, J. & Schrefl, T. (2006). Chapter 2 Micromagnetic Simulation of Magnetic Materials. *Handbook of Magnetic Materials* (pp. 41–125). Elsevier.

Sullivan, C. B. & Kaszynski, A. A. (2019). PyVista: 3D plotting and mesh analysis through a streamlined interface for the Visualization Toolkit (VTK). *Journal of Open Source Software*, **4** (37), 1450.

Taguchi, Y., Oohara, Y., Yoshizawa, H., Nagaosa, N. & Tokura, Y. (2001). Spin Chirality, Berry Phase, and Anomalous Hall Effect in a Frustrated Ferromagnet. *Science*, **291** (5513), 2573–2576.

Tanigaki, T., Shibata, K., Kanazawa, N., Yu, X., Onose, Y., Park, H. S., Shindo, D. & Tokura, Y. (2015). Real-Space Observation of Short-Period Cubic Lattice of Skyrmions in MnGe. *Nano Letters*, **15** (8), 5438–5442.

Tannous, C. & Comstock, R. L. (2017). Magnetic Information-Storage Materials. In S. Kasap & P. Capper (Eds.), *Springer Handbook of Electronic and Photonic Materials* (pp. 1–1). Springer International Publishing.

Tejo, F., Heredero, R. H., Chubykalo-Fesenko, O. & Guslienko, K. Y. (2021). The Bloch point 3D topological charge induced by the magnetostatic interaction. *Scientific Reports*, **11** (1), 21714.

Thiaville, A. & Miltat, J. (1994). Controlled Injection of a Singular Point along a Linear Magnetic Structure. *EPL (Europhysics Letters)*, **26** (1), 57.

Thiaville, A., Nakatani, Y., Miltat, J. & Suzuki, Y. (2005). Micromagnetic understanding of current-driven domain wall motion in patterned nanowires. *Europhysics Letters*, **69** (6), 990.

Thiaville, A., García, J. M., Dittrich, R., Miltat, J. & Schrefl, T. (2003). Micromagnetic study of Bloch-point-mediated vortex core reversal. *Physical Review B*, **67** (9), 094410.

Thiaville, A. & Nakatani, Y. (2014). 6 - Micromagnetics of Domain Wall Dynamics in Soft Nanostrips. In T. Shinjo (Ed.), *Nanomagnetism and Spintronics (Second Edition)* (pp. 261–313). Elsevier.

Thiaville, A. & Miltat, J. (2018). Topology and Magnetic Domain Walls. In J. Zang, V. Cros & A. Hoffmann (Eds.), *Topology in Magnetism* (pp. 41–73). Springer International Publishing.

Tomasello, R., Martinez, E., Zivieri, R., Torres, L., Carpentieri, M. & Finocchio, G. (2014). A strategy for the design of skyrmion racetrack memories. *Scientific Reports*, **4** (1), 6784.

Tylissanakis, G. & Cotronis, Y. (2009). Data Provenance and Reproducibility in Grid Based Scientific Workflows. *2009 Workshops at the Grid and Pervasive Computing Conference*, 42–49.

Van Waeyenberge, B., Puzic, A., Stoll, H., Chou, K. W., Tyliszczak, T., Hertel, R., Fähnle, M., Brückl, H., Rott, K., Reiss, G., Neudecker, I., Weiss, D., Back, C. H. & Schütz, G. (2006). Magnetic vortex core reversal by excitation with short bursts of an alternating field. *Nature*, **444** (7118), 461–464.

Vansteenkiste, A., Leliaert, J., Dvornik, M., Helsen, M., Garcia-Sanchez, F. & Van Waeyenberge, B. (2014). The design and verification of MuMax3. *AIP Advances*, **4** (10), 107133.

Vazquez, M. (2015). *Magnetic nano- and microwires: Design, synthesis, properties and applications*. Elsevier.

Vila, L., Darques, M., Encinas, A., Ebels, U., George, J.-M., Faini, G., Thiaville, A. & Piraux, L. (2009). Magnetic vortices in nanowires with transverse easy axis. *Physical Review B*, **79** (17), 172410.

Virtanen, P., Gommers, R., Oliphant, T. E., Haberland, M., Reddy, T., Cournapeau, D., Burovski, E., Peterson, P., Weckesser, W., Bright, J., van der Walt, S. J., Brett, M., Wilson, J., Millman, K. J., Mayorov, N., Nelson, A. R. J., Jones, E., Kern, R., Larson, E., … van Mulbregt, P. (2020). SciPy 1.0: Fundamental algorithms for scientific computing in Python. *Nature Methods*, **17** (3), 261–272.

Volovik, G. E. (1987). Linear momentum in ferromagnets. *Journal of Physics C: Solid State Physics*, **20** (7), L83–L87.

Wachowiak, A., Wiebe, J., Bode, M., Pietzsch, O., Morgenstern, M. & Wiesendanger, R. (2002). Direct Observation of Internal Spin Structure of Magnetic Vortex Cores. *Science*, **298** (5593), 577–580.

Waldrop, M. M. (2016). The chips are down for Moore's law. *Nature News*, **530** (7589), 144.

Wang, J., Kuo, T.-y., Li, L. & Zeller, A. (2021). Assessing and restoring reproducibility of Jupyter notebooks. *Proceedings of the 35th IEEE/ACM International Conference on Automated Software Engineering*, 138–149.

Wang, K., Zhang, Y., Bheemarasetty, V., Zhou, S., Ying, S.-C. & Xiao, G. (2022a). Single skyrmion true random number generator using local dynamics and interaction between skyrmions. *Nature Communications*, **13** (1).

Wang, K., Bheemarasetty, V., Duan, J., Zhou, S. & Xiao, G. (2022b). Fundamental physics and applications of skyrmions: A review. *Journal of Magnetism and Magnetic Materials*, **563**, 169905.

Wang, Z., Guo, M., Zhou, H.-A., Zhao, L., Xu, T., Tomasello, R., Bai, H., Dong, Y., Je, S.-G., Chao, W., Han, H.-S., Lee, S., Lee, K.-S., Yao, Y., Han, W., Song, C., Wu, H., Carpentieri, M., Finocchio, G., … Jiang, W. (2020). Thermal generation, manipulation and thermoelectric detection of skyrmions. *Nature Electronics*, **3** (11), 672–679.

Wartelle, A., Trapp, B., Staňo, M., Thirion, C., Bochmann, S., Bachmann, J., Foerster, M., Aballe, L., Menteş, T. O., Locatelli, A., Sala, A., Cagnon, L., Toussaint, J.-C. & Fruchart, O. (2019). Bloch-point-mediated topological transformations of magnetic domain walls in cylindrical nanowires. *Physical Review B*, **99** (2), 024433.

Wegrowe, J.-E. & Ciornei, M.-C. (2012). Magnetization dynamics, gyromagnetic relation, and inertial effects. *American Journal of Physics*, **80** (7), 607–611.

Wiesendanger, R. (2016). Nanoscale magnetic skyrmions in metallic films and multilayers: A new twist for spintronics. *Nature Reviews Materials*, **1** (7), 1–11.

Wieser, R., Nowak, U. & Usadel, K. D. (2004). Domain wall mobility in nanowires: Transverse versus vortex walls. *Physical Review B*, **69** (6), 064401.

Wilhelm, H., Baenitz, M., Schmidt, M., Naylor, C., Lortz, R., Rößler, U. K., Leonov, A. A. & Bogdanov, A. N. (2012). Confinement of chiral magnetic modulations in the precursor region of FeGe. *Journal of Physics: Condensed Matter*, **24** (29), 294204.

Winkler, T. B., Beg, M., Lang, M., Kläui, M. & Fangohr, H. (2023). *Energetics and Dynamics of a stable Bloch point*. arXiv: 2303.10091 [cond-mat].

Wintz, S., Tiberkevich, V., Weigand, M., Raabe, J., Lindner, J., Erbe, A., Slavin, A. & Fassbender, J. (2016). Magnetic vortex cores as tunable spin-wave emitters. *Nature Nanotechnology*, **11** (11), 948–953.

Wohlhüter, P., Bryan, M. T., Warnicke, P., Gliga, S., Stevenson, S. E., Heldt, G., Saharan, L., Suszka, A. K., Moutafis, C., Chopdekar, R. V., Raabe, J., Thomson, T., Hrkac, G. & Heyderman, L. J. (2015). Nanoscale switch for vortex polarization mediated by Bloch core formation in magnetic hybrid systems. *Nature Communications*, **6**, 7836.

Woo, S., Litzius, K., Krüger, B., Im, M.-Y., Caretta, L., Richter, K., Mann, M., Krone, A., Reeve, R. M., Weigand, M., Agrawal, P., Lemesh, I., Mawass, M.-A., Fischer, P., Kläui, M. & Beach, G. S. D. (2016). Observation of room-temperature magnetic skyrmions and their current-driven dynamics in ultrathin metallic ferromagnets. *Nature Materials*, **15** (5), 501–506.

Xing, X. J., Yu, Y. P., Wu, S. X., Xu, L. M. & Li, S. W. (2008). Bloch-point-mediated magnetic antivortex core reversal triggered by sudden excitation of a suprathreshold spin-polarized current. *Applied Physics Letters*, **93** (20), 202507.

Xing, X., Pong, P. W. T. & Zhou, Y. (2016). Skyrmion domain wall collision and domain wall-gated skyrmion logic. *Physical Review B*, **94** (5), 054408.

Yan, M., Andreas, C., Kákay, A., García-Sánchez, F. & Hertel, R. (2011). Fast domain wall dynamics in magnetic nanotubes: Suppression of Walker breakdown and Cherenkov-like spin wave emission. *Applied Physics Letters*, **99** (12), 122505.

Yang, S. A., Beach, G. S. D., Knutson, C., Xiao, D., Niu, Q., Tsoi, M. & Erskine, J. L. (2009). Universal Electromotive Force Induced by Domain Wall Motion. *Physical Review Letters*, **102** (6), 067201.

Ye, J., Kim, Y. B., Millis, A. J., Shraiman, B. I., Majumdar, P. & Tešanović, Z. (1999). Berry Phase Theory of the Anomalous Hall Effect: Application to Colossal Magnetoresistance Manganites. *Physical Review Letters*, **83** (18), 3737–3740.

Yosida, K. (1957). Magnetic Properties of Cu-Mn Alloys. *Physical Review*, **106** (5), 893–898.

Yu, X. Z., Onose, Y., Kanazawa, N., Park, J. H., Han, J. H., Matsui, Y., Nagaosa, N. & Tokura, Y. (2010). Real-space observation of a two-dimensional skyrmion crystal. *Nature*, **465** (7300), 901–904.

Yu, X. Z., Kanazawa, N., Onose, Y., Kimoto, K., Zhang, W. Z., Ishiwata, S., Matsui, Y. & Tokura, Y. (2011). Near room-temperature formation of a skyrmion crystal in thin-films of the helimagnet FeGe. *Nature Materials*, **10** (2), 106–109.

Zambrano-Rabanal, C., Valderrama, B., Tejo, F., Elías, R. G., Nunez, A. S., Carvalho-Santos, V. L. & Vidal-Silva, N. (2023). Magnetostatic interaction between Bloch point nanospheres. *Scientific Reports*, **13** (1), 7171.

Zang, J., Mostovoy, M., Han, J. H. & Nagaosa, N. (2011). Dynamics of Skyrmion Crystals in Metallic Thin Films. *Physical Review Letters*, **107** (13), 136804.

Zázvorka, J., Jakobs, F., Heinze, D., Keil, N., Kromin, S., Jaiswal, S., Litzius, K., Jakob, G., Virnau, P., Pinna, D., Everschor-Sitte, K., Rózsa, L., Donges, A., Nowak, U. & Kläui, M. (2019). Thermal skyrmion diffusion used in a reshuffler device. *Nature Nanotechnology*, **14** (7), 658–661.

Zhang, S. & Li, Z. (2004). Roles of Nonequilibrium Conduction Electrons on the Magnetization Dynamics of Ferromagnets. *Physical Review Letters*, **93** (12), 127204.

Zhang, S. & Zhang, S. S.-L. (2009). Generalization of the Landau-Lifshitz-Gilbert Equation for Conducting Ferromagnets. *Physical Review Letters*, **102** (8), 086601.

Zhang, X., Ezawa, M. & Zhou, Y. (2015a). Magnetic skyrmion logic gates: Conversion, duplication and merging of skyrmions. *Scientific Reports*, **5** (1), 9400.

Zhang, X., Zhao, G. P., Fangohr, H., Liu, J. P., Xia, W. X., Xia, J. & Morvan, F. J. (2015b). Skyrmion-skyrmion and skyrmion-edge repulsions in skyrmion-based racetrack memory. *Scientific Reports*, **5** (1), 7643.

Zheng, F., Rybakov, F. N., Borisov, A. B., Song, D., Wang, S., Li, Z.-A., Du, H., Kiselev, N. S., Caron, J., Kovács, A., Tian, M., Zhang, Y., Blügel, S. & Dunin-Borkowski, R. E. (2018). Experimental observation of chiral magnetic bobbers in B20-type FeGe. *Nature Nanotechnology*, **13** (6), 451–455.

Zhu, J., Wu, Y., Hu, Q., Kong, L., Tang, J., Tian, M. & Du, H. (2020). Current-driven transformations of a skyrmion tube and a bobber in stepped nanostructures of chiral magnets. *Science China Physics, Mechanics & Astronomy*, **64** (2), 227511.

Zou, J., Zhang, S. & Tserkovnyak, Y. (2020). Topological Transport of Deconfined Hedgehogs in Magnets. *Physical Review Letters*, **125** (26), 267201.

Zubov, V. E., Krinchik, G. S. & Kudakov, A. D. (1988). Experimental detection of singularities of 'Bloch point' type in a domain boundary. *Pisma v Zhurnal Eksperimentalnoi i Teoreticheskoi Fiziki*, **47**, 134.

Zubov, V. E., Krinchik, G. S. & Kuz'menko, S. N. (1990). Anomalous coercive force of Bloch point in iron single crystals. *Soviet Journal of Experimental and Theoretical Physics Letters*, **51**, 477.